

Negative ions

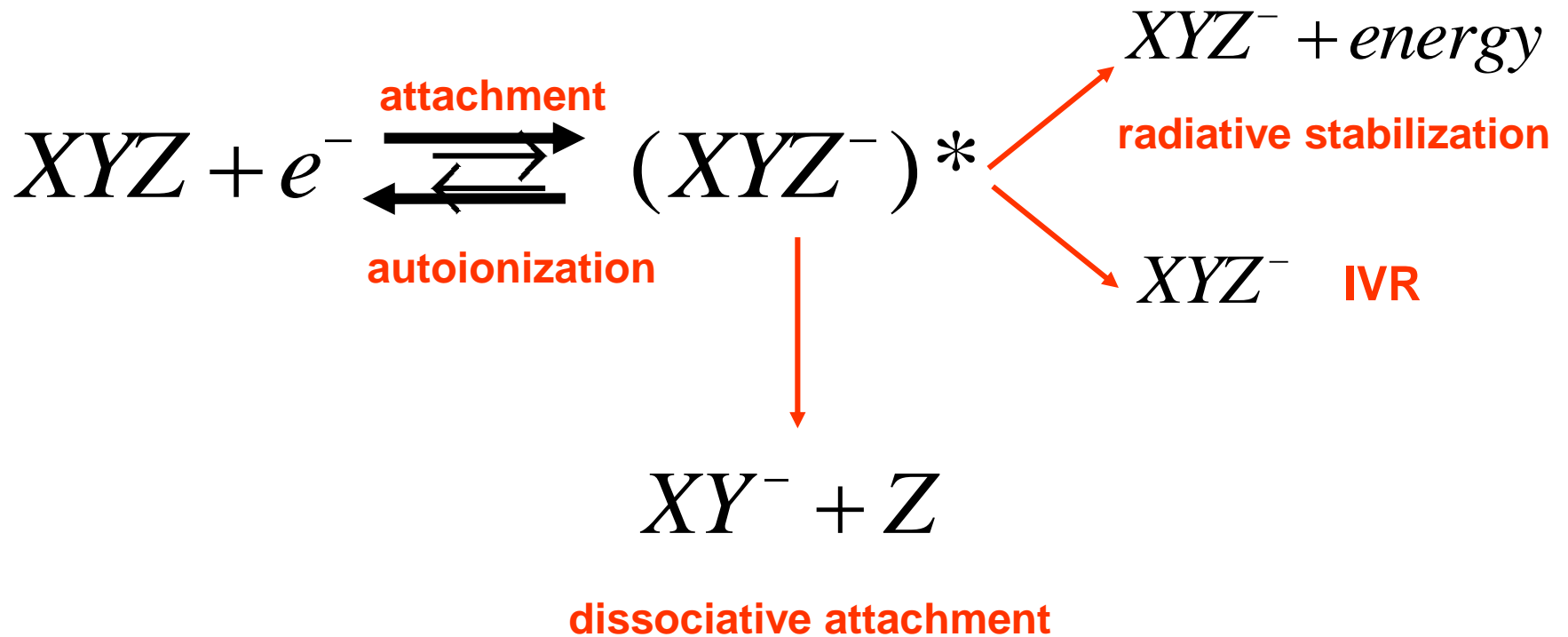
UFP ZS 2024 8C 06. 01. 2025

Date: 23 Apr 2010
Satellite: Hubble Space Telescope
Depicts: Detail of the Carina Nebula



The chemical physics of negative ions

A) Negative ion formation mechanisms: (molecule XYZ)



B) Negative ion destruction mechanisms

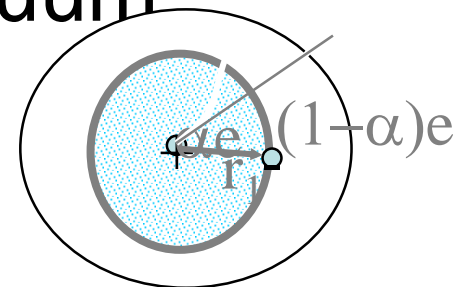


The negative hydrogen ion H^-

- one of the most important negative ions in the universe!
- It exists, electron affinity (binding energy of the extra electron) = 0.75 eV
- why does it exist? first electron in H only partially shields the nuclear charge



- QM calculations confirm this
- responsible for most of the continuum opacity of the photosphere



H⁻ in the photosphere

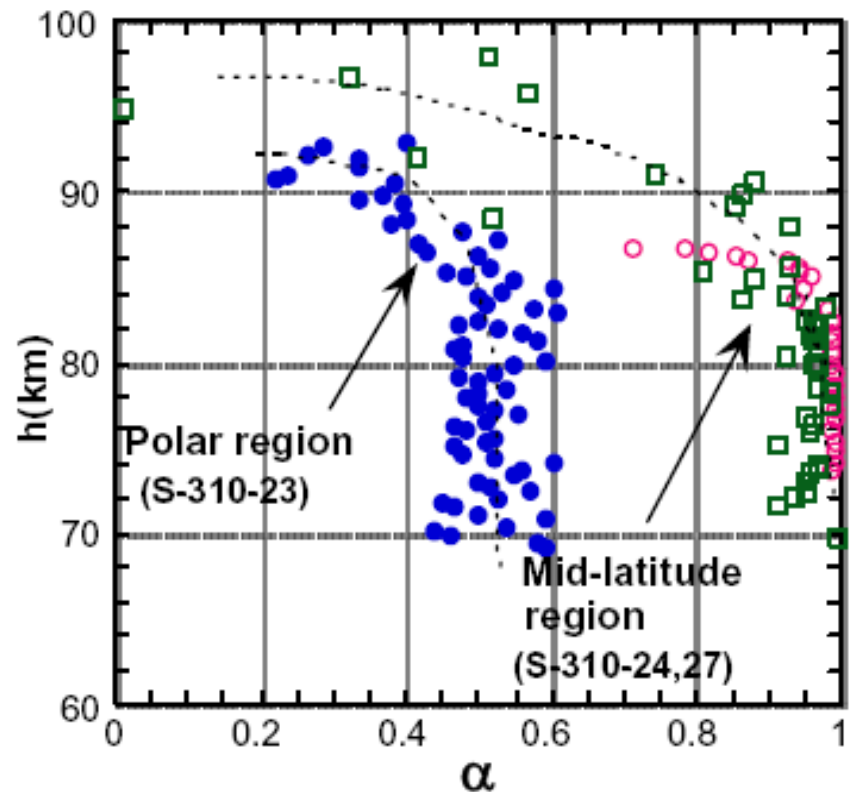
- **photosphere** - what you see when you look at the sun
- about 400 km thick, cool ~ 4400K – 5800K, mostly H
- remarkably opaque at infrared and shorter wavelengths
- most H in ground state and thus does not contribute much to absorption
- need 13.6 eV (121.6 nm) to get H in first excited state
- 1939- about one in 10⁷ H's are H⁻, and need only 0.75 eV to remove extra electron → 1653 nm (Saha relation)
- **so H⁻ can account for absorption down to very long wavelengths**
- negative H makes photosphere as opaque as a dense object, therefore it radiates like a blackbody

negativne H činí fotosféru neprůhlednou jako hustý objekt,
proto vyzařuje jako černé těleso

negative ions in the earth's ionosphere

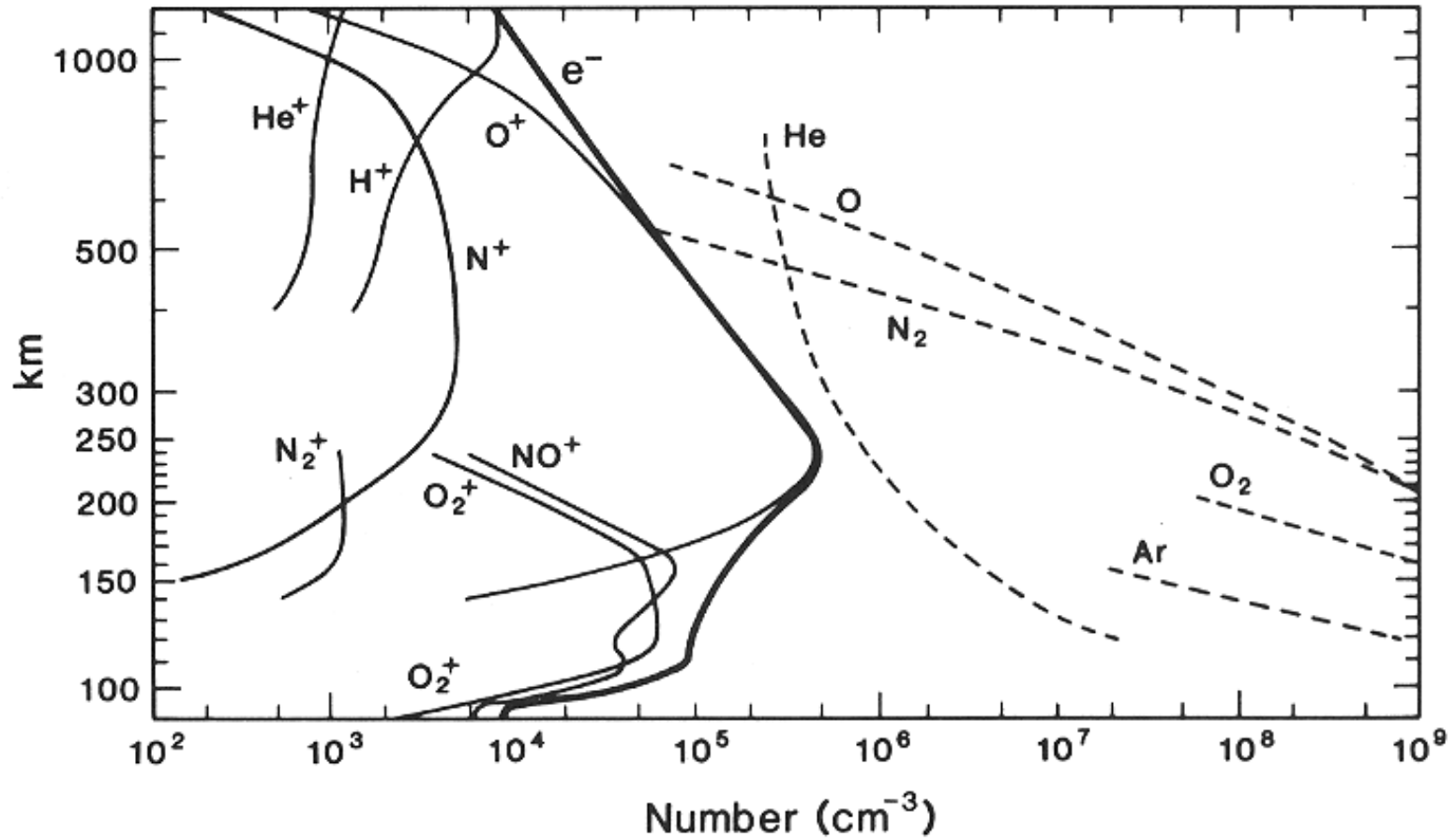
- negative ions (O_2^-) are generally present in the lower ionosphere (D region) 60 – 90 km
- they may play a role in the creation and destruction of the ozone layer observed at 76 km in the polar region

Data from rocket borne instruments

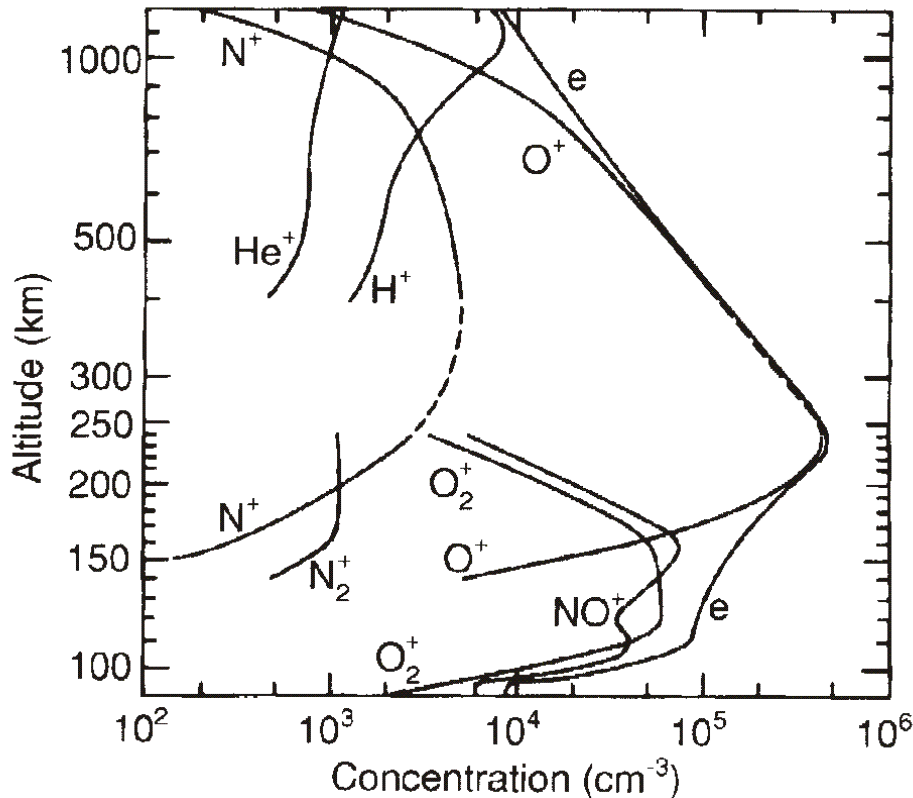


$$\alpha = \frac{N_-}{N_+}$$

- Neutral density exceeds the ion density below about 500 km.

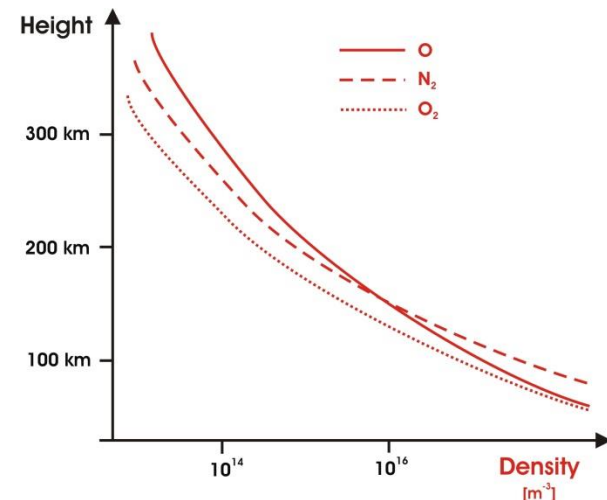


Ionosphere composition



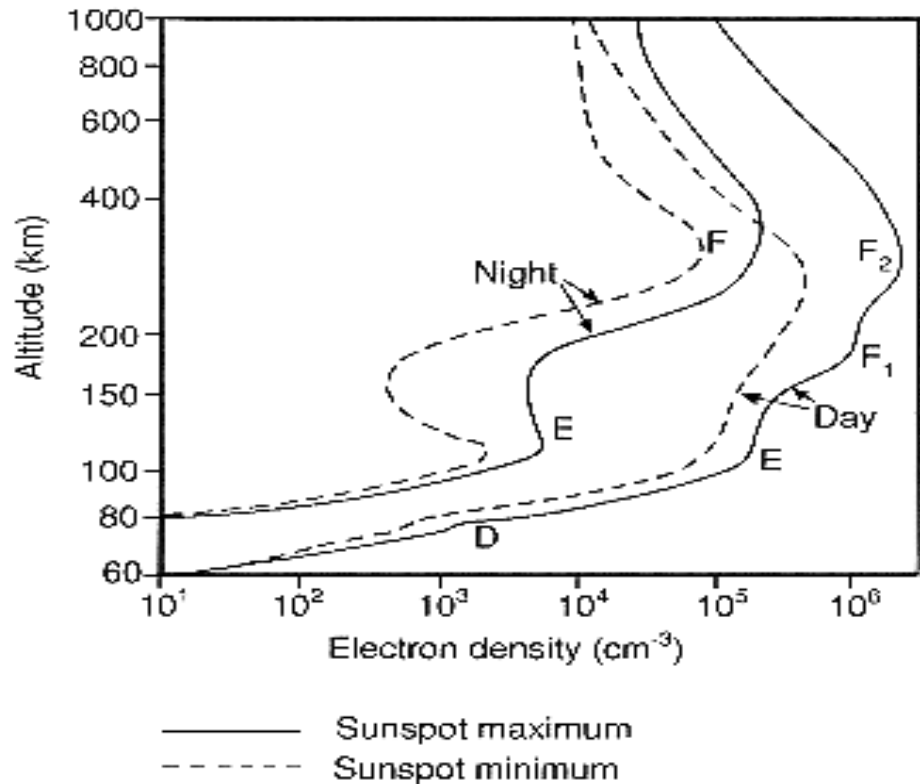
Dayside ionosphere composition at solar minimum.

Major F-region ions is O⁺, followed by H⁺ at the top and NO⁺ and O₂⁺ at the bottom. Note that neutral gas concentration at 300 km is around 10⁸ cm⁻³, so ion concentrations are 2 orders of magnitude smaller. Negative ions are found only in the lower ionosphere (D region). The net charge of the ionosphere is zero.



- The extent of the ionosphere

- There are ions and electrons at all altitudes in the atmosphere.
- Below about 60km the charged particles do not play an important part in determining the chemical or physical properties of the atmosphere.
- Identification of ionospheric layers is related to inflection points in the vertical density profile.



Negative ions in ionosphere

Negative ions are a feature of the D-region ionosphere, where they hold a substantial portion of the negative charge. Negative ion chemistry is initiated by electron attachment to molecular oxygen



after which subsequent reactions form other ions, including complex clusters (see, e.g. Hargreaves, 1992, 231–233). Based on laboratory work and in-situ measurements, the main negative ions are expected to be CO_3^- and NO_3^- , and their hydrates. The main reaction path leading from the initial O_2^- to these “terminal” ions involves neutral ozone, carbon dioxide, and nitric oxide, and the formation of intermediate ion O_3^- (Reid, 1987). Negative ions are present at altitudes below 80 km, where the atmospheric density is high enough so that the 3-body reaction of Eq. (1) is efficient. The balance with electrons is then determined by electron detachment reactions, such as



Most of the balancing reactions depend on the solar light, such that at night the electrons nearly disappear from altitudes below 80 km and negative charge is held largely by the ions. During sunset, there is a transition of negative charge from electrons to negative ions, and a reverse transition occurs during sunrise. Any realistic modelling of the D-region ionosphere requires consideration of negative ion chemistry.

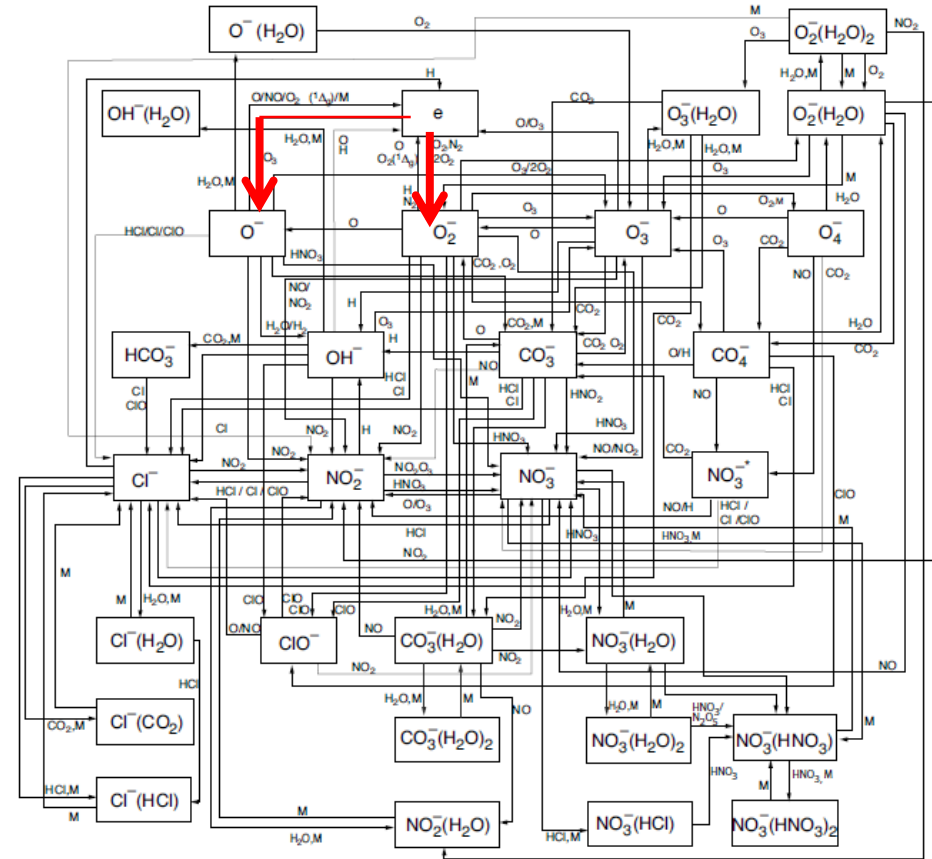


Fig. 1. Block diagram for the negative ion scheme of the SIC model. The various ions in the blocks are either the reactants or the final products of the reactions sketched by the connecting arrows. The arrows are labelled with the neutral constituents taking part in the reactions. Note that photodetachment and photodissociation reactions are not shown.

Table 1. Most important electron-detachment reactions from the SIC model. Sources of the rate coefficients are listed in Turunen et al. (1996). Units are $\text{m}^3 \text{s}^{-1}$ for R1–R3 and s^{-1} for the other reactions.

#	Reaction	Rate coefficient
R1	$\text{O}^- + \text{M} \rightarrow \text{O} + \text{M} + e$	$< 10^{-18}$
R2	$\text{O}_2^- + \text{O}_2(^1\Delta_g) \rightarrow 2\text{O}_2 + e$	2.0×10^{-16}
R3	$\text{O}_2^- + \text{O} \rightarrow \text{O}_3 + e$	1.5×10^{-16}
R4	$\text{O}_2^- + h\nu (< 2695 \text{ nm}) \rightarrow \text{O}_2 + e$	3.8×10^{-1}
R5	$\text{NO}_3^- + h\nu (< 318 \text{ nm}) \rightarrow \text{NO}_3 + e$	5.2×10^{-2}
R6	$\text{CO}_3^- + h\nu (< 428 \text{ nm}) \rightarrow \text{CO}_3 + e$	2.2×10^{-12}

Annales Geophysicae, 24, 187–202, 2006
 SRRef-ID: 1432-0576/ag/2006-24-187
 © European Geosciences Union 2006

2006

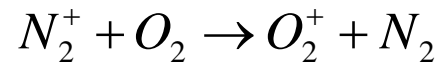


Sunset transition of negative charge in the D-region ionosphere during high-ionization conditions

P. T. Verroenen¹, Th. Ulich², E. Turunen², and C. J. Rodger³

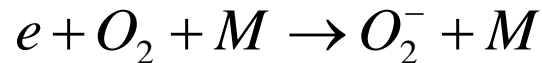
- The D Region

- The most complex and least understood layer in the ionosphere.
- The primary source of ionization in the D region is ionization by solar X-rays which ionize both N_2 and O_2
- Lyman- α ionization of the NO molecule.
- Precipitating magnetospheric electrons may also be important.
- Initial positive ions are N_2^+ , O_2^+ and NO^+



- The primary positive ions are O_2^+ and NO^+
- The most common negative ion is NO_3^-

- The first step in making a negative ion is



Negative ions

Formation of negative ions - attachment

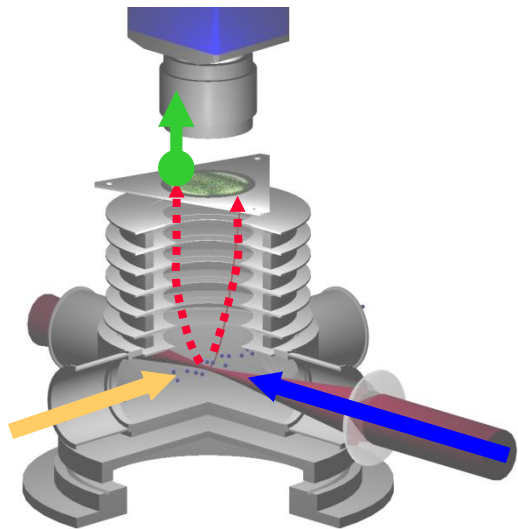
Interaction of electrons with atoms and molecules

Date: 23 Apr 2010

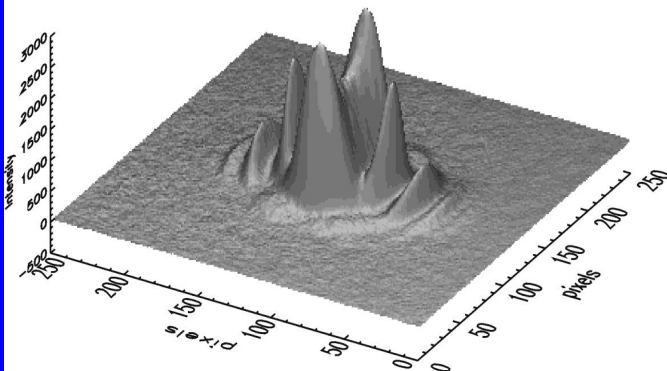
Satellite: Hubble Space Telescope

Depicts: Detail of the Carina Nebula

Photoelectron spectrometer



Photoelectron spectrum



Visible



Infrared

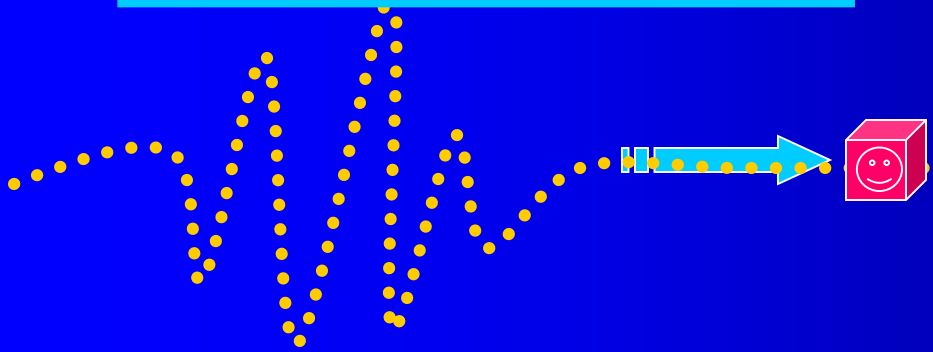
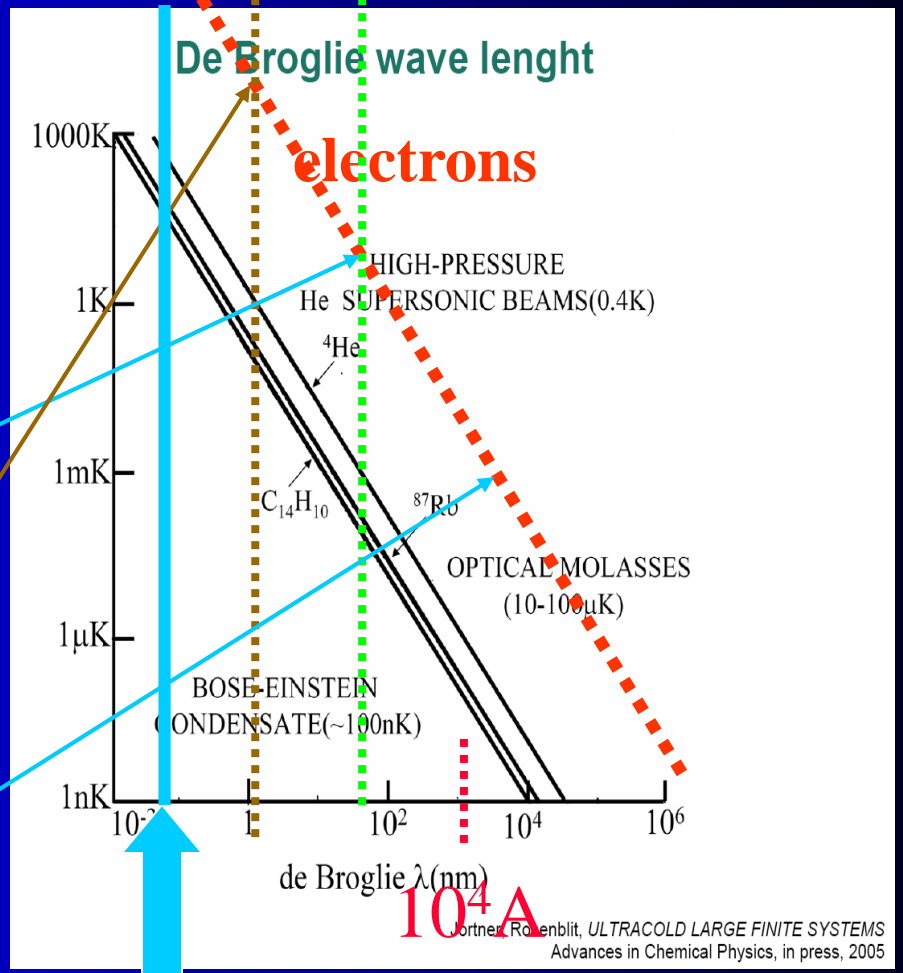
De Broglie wave length

$$\lambda = \frac{h}{p} = \frac{h}{mv} \sqrt{1 - \frac{v^2}{c^2}}$$

$$\lambda_e (4K) \sim 540 \text{ \AA} \sim 54 \times 10^{-9} \text{ m}$$

$$\lambda_e (1eV) \sim 11.6 \text{ \AA} \sim 1.16 \times 10^{-9} \text{ m}$$

$$\lambda_e (mK) \sim 3 \times 10^4 \text{ \AA} \sim 3 \times 10^{-6} \text{ m}$$



Jednorozměrný rozptyl

Parametry jsou E, V_0, a

$T+R=1$

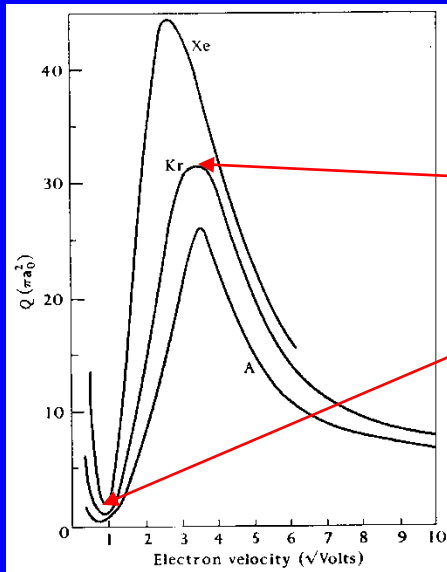


FIG. 1.9. Observed total collision cross-sections of A, Kr, and Xe.

$$2k'_n n = n\pi$$

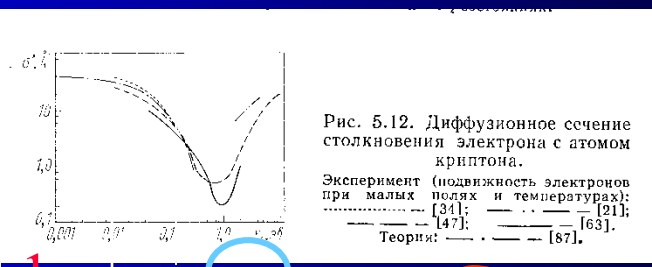
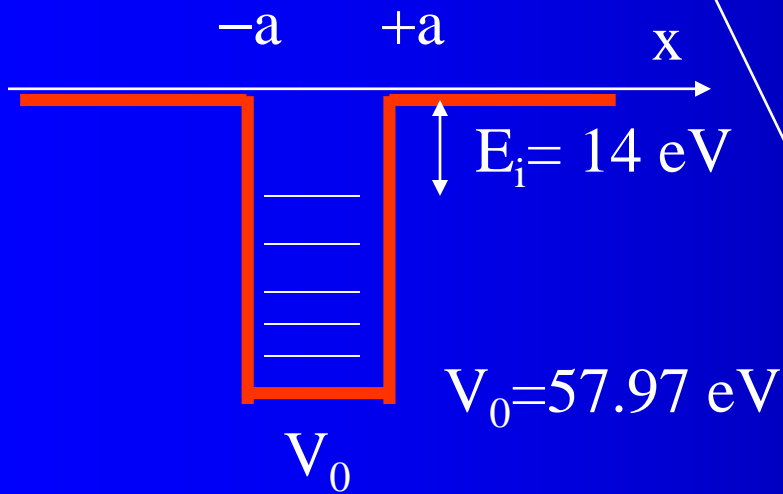
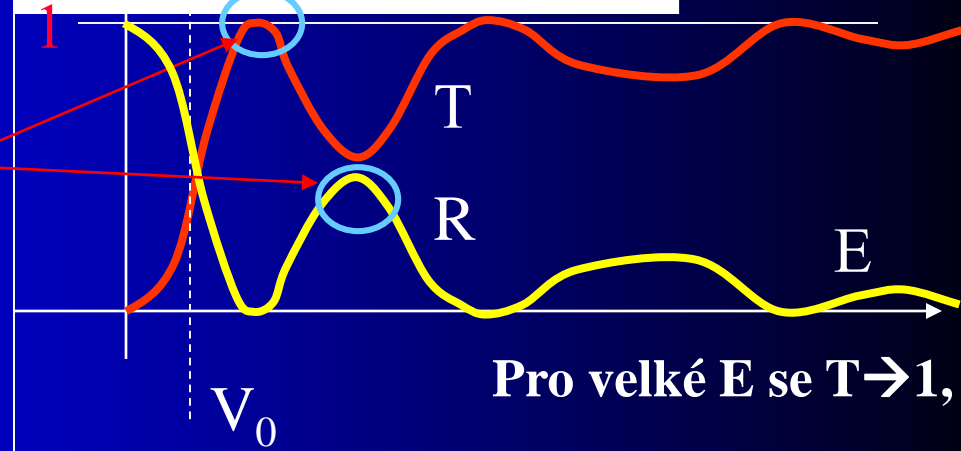


Рис. 5.12. Диффузионное сечение столкновения электрона с атомом криптона.
Эксперимент (подвижность электронов при малых полях и температурах):
— [31]; — [21];
— [47]; — [63].
Теория: — [87].



Pro velké E se $T \rightarrow 1$,

$$k' = \sqrt{2m(E + V_0) / h^2}$$

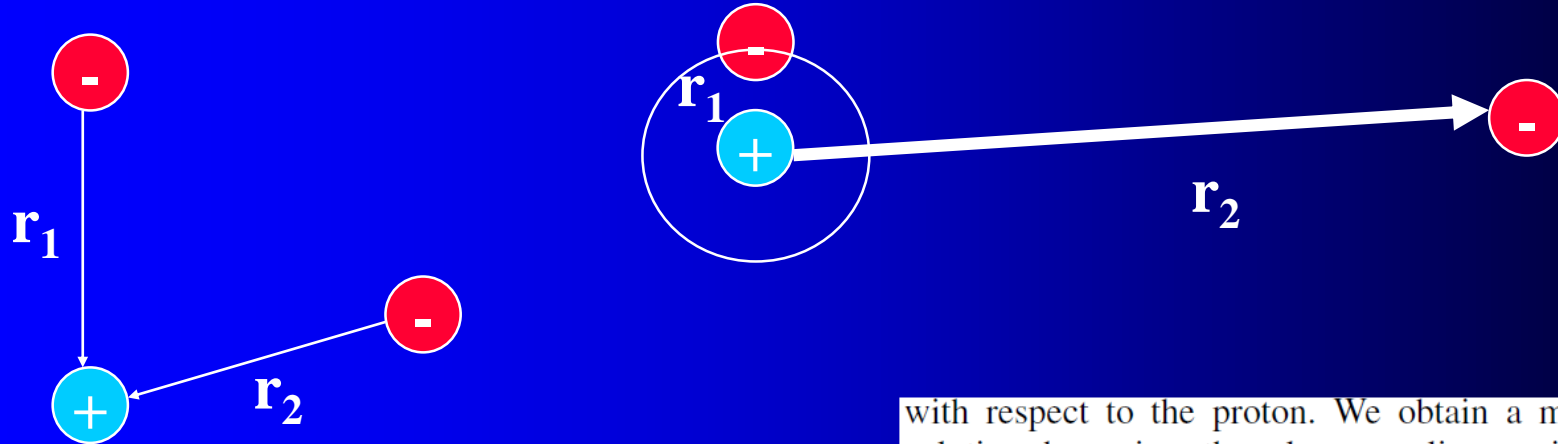
Kr; $a=2\text{\AA}$
 $E_i = 14 \text{ eV} \rightarrow V_0 = 57.97 \text{ eV}$

$$E=0.013 \quad V_0=0.75 \text{ eV}$$

Three-Body Recombination of Atomic Ions with Slow Electrons

S. X. Hu

Laboratory for Laser Energetics, University of Rochester, 250 East River Road, Rochester, New York 14623, USA



We consider the simplest TBR in the case of hydrogen formation, in which two free electrons interact with a proton. To investigate the three-body interaction dynamics, we numerically solve the six-dimensional (6D) time-dependent Schrödinger equation, which has the following form (atomic units are used throughout):

$$i \frac{\partial}{\partial t} \Phi(\mathbf{r}_1, \mathbf{r}_2, t) = \left[-\frac{1}{2} (\Delta_{\mathbf{r}_1} + \Delta_{\mathbf{r}_2}) - \frac{1}{r_1} - \frac{1}{r_2} + \frac{1}{|\mathbf{r}_1 - \mathbf{r}_2|} \right] \Phi(\mathbf{r}_1, \mathbf{r}_2, t), \quad (1)$$

where \mathbf{r}_1 and \mathbf{r}_2 are the position vectors of each electron, with respect to the proton. We obtain a more tractable

solution by using the close-coupling recipe [12]: expanding the 6D wave function $\Phi(\mathbf{r}_1, \mathbf{r}_2|t)$ in terms of bipolar spherical harmonics $Y_{l_1 l_2}^{LS}(\Omega_1, \Omega_2)$, $\Phi(\mathbf{r}_1, \mathbf{r}_2|t) = \sum_{LS} \sum_{l_1 l_2} [\Psi_{l_1 l_2}^{(LS)}(r_1, r_2|t)/r_1 r_2] Y_{l_1 l_2}^{LS}(\Omega_1, \Omega_2)$, for a specific symmetry (LS). We can also expand the Coulomb repulsion term $1/|\mathbf{r}_1 - \mathbf{r}_2|$ in terms of spherical harmonics. Substituting these expansions into the above Schrödinger Eq. (1) and integrating over the angles Ω_1 and Ω_2 yields a set of coupled partial differential equations with only two radial variables r_1 and r_2 left:

$$i \frac{\partial}{\partial t} \Psi_j(r_1, r_2|t) = [\hat{T}_1 + \hat{T}_2 + \hat{V}_c] \Psi_j(r_1, r_2|t) + \sum_k \hat{V}_{j,k}^I(r_1, r_2|t) \Psi_k(r_1, r_2|t), \quad (2)$$

where the partial-wave index j runs from 1 to the total number N of partial waves used for expansion. In Eq. (2),

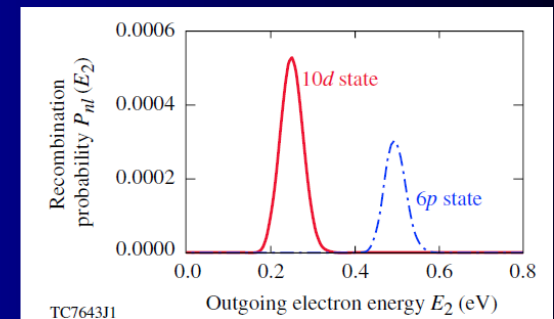
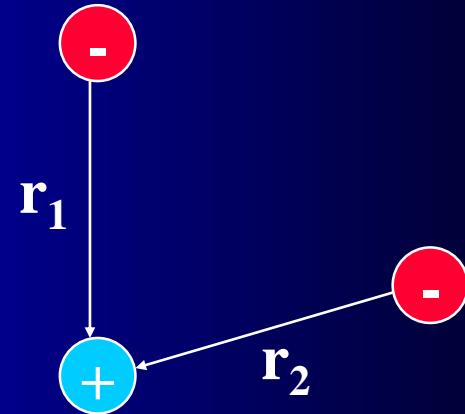
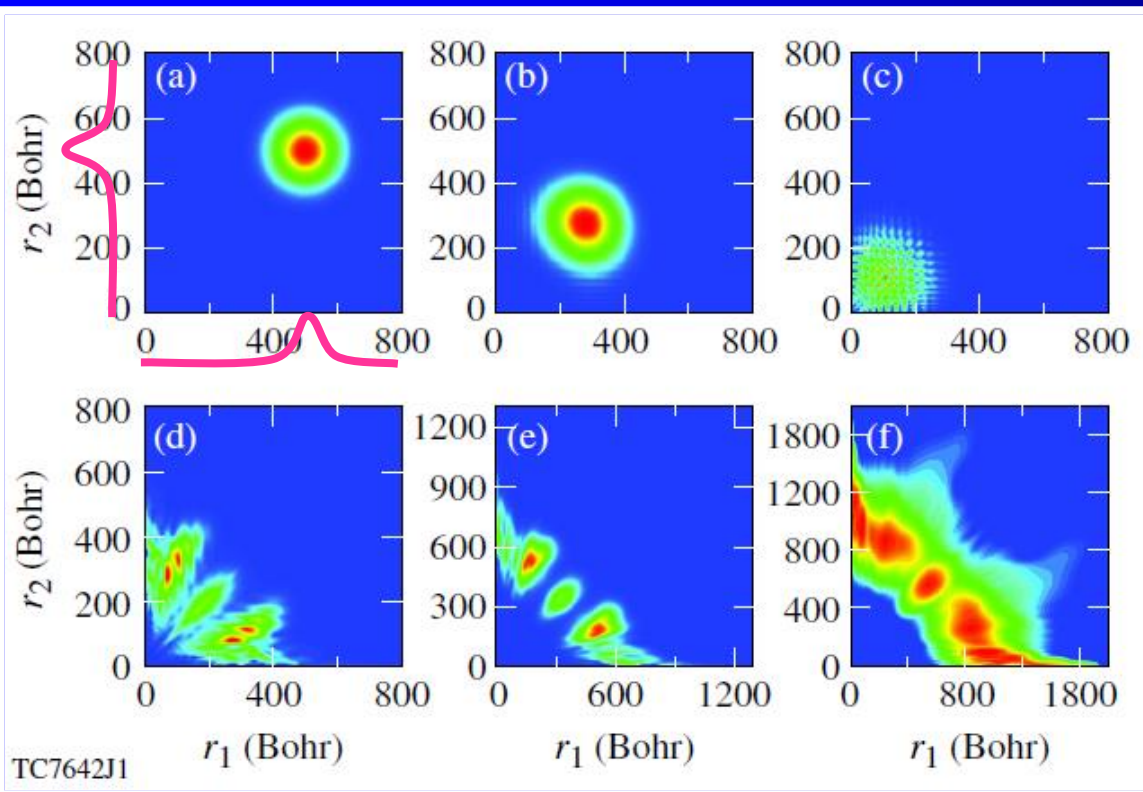
Kvantovka na každý deň

$$i\frac{\partial}{\partial t}\Psi_j(r_1, r_2|t) = [\hat{T}_1 + \hat{T}_2 + \hat{V}_c]\Psi_j(r_1, r_2|t) + \sum_k \hat{V}_{j,k}^I(r_1, r_2|t)\Psi_k(r_1, r_2|t), \quad (2)$$



$$P_{nl}(E_2) = 2 \sum_{LS} \sum_{l_2} \left| \int dr_1 \int dr_2 \phi_{nl}^*(r_1) \phi_{k_2 l_2}^*(r_2) \Psi_{ll_2}^{(LS)}(r_1, r_2, t = t_f) \right|^2,$$

$K_E = 0.1 \text{ eV}$



Thus, for the case of $K_E = 0.1 \text{ eV}$ considered in Figs. 1 and 2, the total system energy is about $E_{\text{tot}} \sim 0.12 \text{ eV}$ instead of $2K_E$. Hence, when one electron recombines to the $10d$ state ($|E_{10d}| \approx 0.136 \text{ eV}$) of the H atom, the outgoing electron takes an initial total energy of 0.12 eV plus $|E_{10d}|$, thereby $P_{10d}(E_2)$ peaks at $E_2 \sim 0.256 \text{ eV}$, as shown by the red solid line of Fig. 2. Similar energy conservation is also well satisfied for the recombination to the $6p$ state, as is illustrated by the blue dash-dotted line in Fig. 2. Our quantum calculations unambiguously reveal the essential feature of a TBR process.

FIG. 1 (color online). Snapshots of electron probability distribution on the plane spanned by the radial coordinates r_1 and r_2 for different times: (a) $t = 0.0 \text{ fs}$, (b) $t = 60 \text{ fs}$, (c) $t = 100 \text{ fs}$, (d) $t = 150 \text{ fs}$, (e) $t = 194 \text{ fs}$, and (f) (in log scale) $t = 260 \text{ fs}$.

Kvantovka na každý deň



$K_E = 0.1 \text{ eV}$

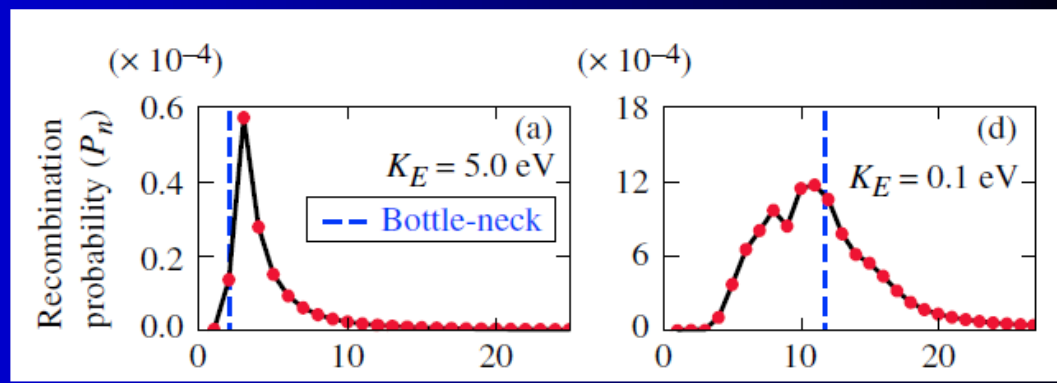


FIG. 3 (color online). The recombination probability P_n as a function of the energy level n , for different electron kinetic energies K_E marked in each panel.

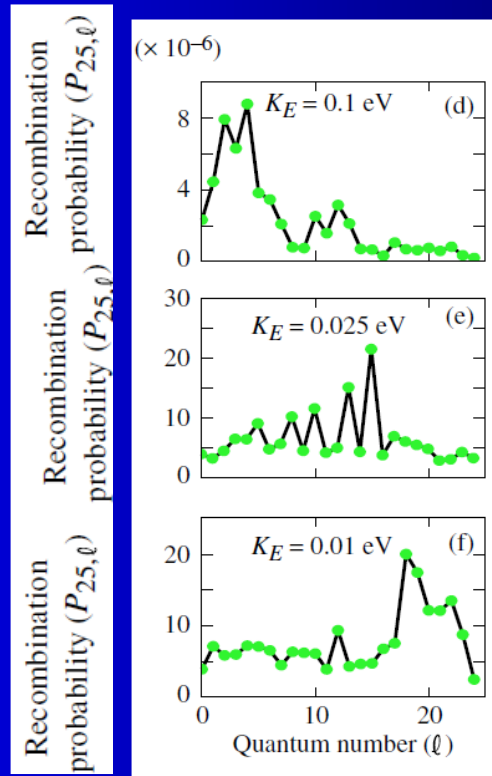
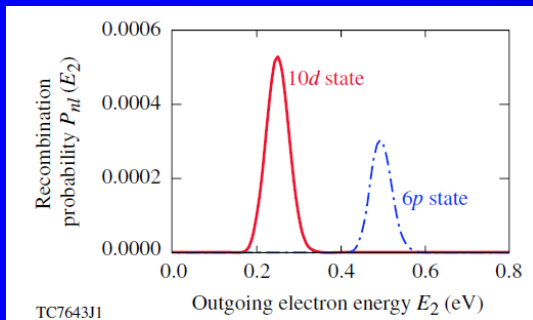
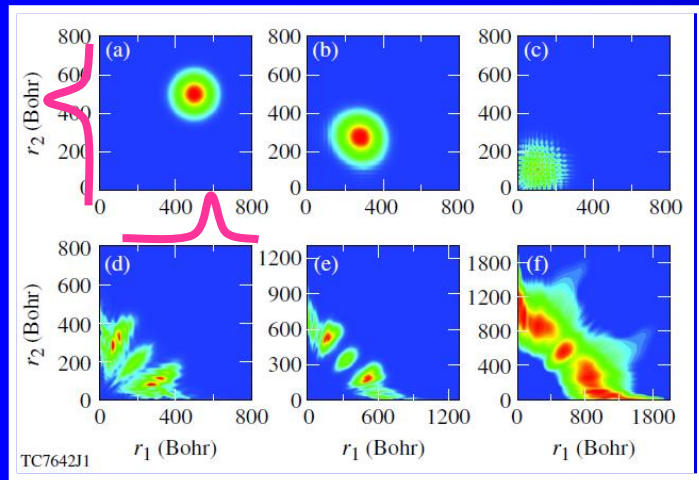
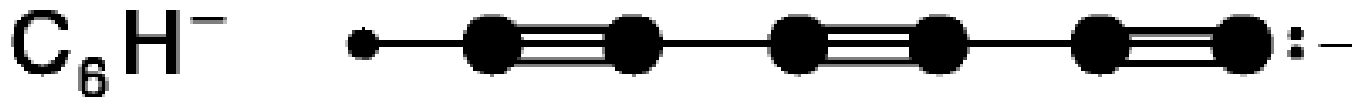


FIG. 4 (color online). The recombination probability $P_{n=25,l}$ as a function of the angular-momentum quantum number l , for different electron kinetic energies K_E marked in each panel.



THE ASTROPHYSICAL JOURNAL, 652: L141–L144, 2006 December 1

© 2006. The American Astronomical Society. All rights reserved. Printed in U.S.A.

2006

LABORATORY AND ASTRONOMICAL IDENTIFICATION OF THE NEGATIVE MOLECULAR ION C_6H^-

M. C. MCCARTHY,¹ C. A. GOTTLIEB,¹ H. GUPTA,^{1,2} AND P. THADDEUS¹

Received 2006 September 28; accepted 2006 October 17; published 2006 November 20

ABSTRACT

The negative molecular ion C_6H^- has been detected in the radio band in the laboratory and has been identified in the molecular envelope of IRC +10216 and in the dense molecular cloud TMC-1. The spectroscopic constants derived from laboratory measurements of 17 rotational lines between 8 and 187 GHz are identical to those derived from the astronomical data, establishing unambiguously that C_6H^- is the carrier of the series of lines with rotational constant 1377 MHz first observed by K. Kawaguchi et al. in IRC +10216. The column density of C_6H^- toward both sources is 1%–5% that of neutral C_6H . These surprisingly high abundances for a negative ion imply that if other molecular anions are similarly abundant with respect to their neutral counterparts, they may be detectable both in the laboratory at high resolution and in interstellar molecular clouds.

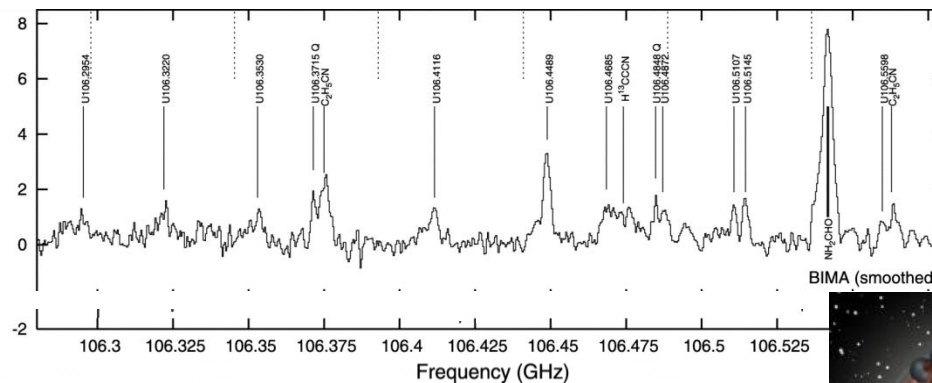
Note added in proof.—A third member in the series, C_4H^- , has now been detected in the laboratory at centimeter and millimeter wavelengths. A full account of this work will be presented elsewhere.

Interstellar Molecules

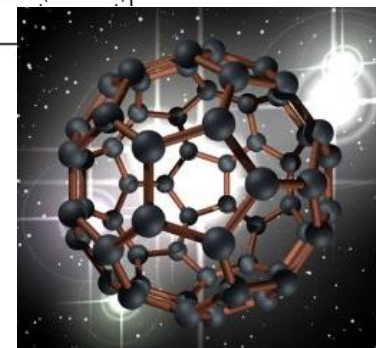
2 atoms	3 atoms	4 atoms	5 atoms	6 atoms	7 atoms	8 atoms	9 atoms	10 atoms	11 atoms	12 atoms	13 atoms
H ₂	C ₃ [*]	c-C ₃ H	C ₅ [*]	C ₅ H	C ₆ H	CH ₃ C ₃ N	CH ₃ C ₄ H	CH ₃ C ₅ N	HC ₉ N	C ₆ H ₆	HC ₁₁ N
AlF	C ₂ H	I-C ₃ H	C ₄ H	I-H ₂ C ₄	CH ₂ CHCN	HC(O)OCH ₃	CH ₃ CH ₂ CN	(CH ₃) ₂ CO	CH ₃ C ₆ H	C ₂ H ₅ OCH ₃	
AlCl	C ₂ O	C ₃ N	C ₄ Si	C ₂ H ₄ [*]	CH ₃ C ₂ H	CH ₃ COOH	(CH ₃) ₂ O	(CH ₂ OH) ₂	C ₂ H ₅ OCHO	n-C ₃ H ₇ CN	
C ₂ ^{**}	C ₂ S	C ₃ O	I-C ₃ H ₂	CH ₃ CN	HC ₅ N	C ₇ H	CH ₃ CH ₂ OH	CH ₃ CH ₂ CHO			
CH	CH ₂	C ₃ S	c-C ₃ H ₂	CH ₃ NC	CH ₃ CHO	H ₂ C ₆	HC ₇ N				
CH⁺	HCN	C ₂ H ₂ [*]	H ₂ CCN	CH ₃ OH	CH ₃ NH ₂	CH ₂ OHCHO	C ₈ H				
CN	HCO	NH ₃	CH ₄ [*]	CH ₃ SH	c-C ₂ H ₄ O	I-HC ₆ H [*]	CH ₃ C(O)NH ₂				
CO	HCO⁺	HCCN	HC ₃ N	HC₃NH⁺	H ₂ CCHOH	CH ₂ CHCHO	C₈H⁻				
CO⁺	HCS⁺	HCNH⁺	HC ₂ NC	HC ₂ CHO	C₆H⁻	CH ₂ CCHCN	C ₃ H ₆				
CP	HOC⁺	HNCO	HCOOH	NH ₂ CHO		H ₂ NCH ₂ CN					
SiC	H ₂ O	HNCS	H ₂ CNH	C ₅ N							
HCl	H ₂ S	HOCO⁺	H ₂ C ₂ O	I-HC ₄ H [*]							
KCl	HNC	H ₂ CO	H ₂ NCN	I-HC ₄ N							
NH	HNO	H ₂ CN	HNC ₃	c-H ₂ C ₃ O							
NO	MgCN	H ₂ CS	SiH ₄ [*]	H ₂ CCNH							
NS	MgNC	H₃O⁺	H₂COH⁺	C₅N⁻							
NaCl	N₂H⁺	c-SiC ₃	C₄H⁻								
OH	N ₂ O	CH ₃ [*]	HC(O)CN								
PN	NaCN	C₃N⁻									
SO	OCS	PH ₃									
SO⁺	SO ₂	HCNO									
SiN	c-SiC ₂	HOCN									
SiO	CO ₂ [*]	HSCN									
SiS	NH ₂										
CS	H₃⁺*										
HF	H₂D⁺										
SH [*]	HD₂⁺										
HD	SiCN										
FeO	AiNC										
O ₂	SiNC										
CF⁺	HCP										
SiH	CCP										
PO											
AIO											

Cations

Anions



Friedel et al.,
ApJ 600, 234
(2004)



<https://cdms.astro.uni-koeln.de/classic/molecules>

Molecules in the Interstellar Medium or Circumstellar Shells (as of 11/2024)

2 atoms	3 atoms	4 atoms	5 atoms	6 atoms	7 atoms	8 atoms	9 atoms	10 atoms	11 atoms	12 atoms	>12 atoms
CH ⁺	C ₂ ⁺	c-C ₃ H	C ₃ ⁺	C ₃ H	C ₃ H	CH ₃ C ₂ N	CH ₃ C ₂ H	CH ₃ C ₂ N	HC ₃ N	c-C ₆ H ₆ ⁺	C ₆₀ ⁺
CH	C ₂ H	I-C ₃ H	C ₃ H	I-H ₂ C ₄	CH ₂ CHCN	HC(O)OCH ₃	CH ₃ CH ₂ CN	(CH ₃) ₂ CO	CH ₃ C ₆ H	n-C ₃ H ₇ CN	C ₇₀ ⁺
CN	C ₂ O	C ₂ N	C ₂ Si	C ₂ H ₄ ⁺	CH ₃ C ₂ H	CH ₃ COOH	(CH ₃) ₂ O	(CH ₂ OH) ₂	C ₂ H ₃ OCHO	I-C ₃ H ₇ CN	C ₆₀ ⁺
OH	C ₂ S	C ₂ O	I-C ₃ H ₂	CH ₃ CN	HC ₃ N	C ₇ H	CH ₃ CH ₂ OH	CH ₃ CH ₂ CHO	CH ₃ OC(O)CH ₃	C ₂ H ₃ OCH ₃	c-C ₆ H ₅ CN
CO	CH ₂	C ₂ S	c-C ₃ H ₂	CH ₃ NC	CH ₃ CHO	C ₆ H ₂	HC ₇ N	CH ₃ CH ₂ CHO	CH ₃ C(O)CH ₂ OH	1-c-C ₆ H ₅ CN	HC ₁₁ N
H ₂	HCN	C ₂ H ₂ ⁺	H ₂ CCN	CH ₃ OH	CH ₃ NH ₂	CH ₂ OHCHO	C ₆ H	CH ₃ OCH ₂ OH	c-C ₆ H ₆	2-c-C ₆ H ₅ CN	1-C ₁₀ H ₇ CN
SiO	HCO	NH ₃	CH ₄ ⁺	CH ₃ SH	c-C ₂ H ₄ O	I-HC ₆ H ⁺	CH ₃ C(O)NH ₂	c-C ₆ H ₄	HOCH ₂ CH ₂ NH ₂	CH ₃ C ₇ N (?)	2-C ₁₀ H ₇ CN
CS	HCO ⁺	HCCN	HC ₃ N	HC ₃ NH ⁺	H ₂ CCOH	CH ₂ CHCHO	C ₆ H ⁺	H ₂ CCCHC ₃ N	H ₂ CCCHC ₄ H	n-C ₃ H ₇ OH	c-C ₉ H ₈
SO	HCS ⁺	HCNH ⁺	HCCNC	HCCOCHO	C ₆ H ⁺	CH ₂ CCHCN	C ₆ H ₆	C ₂ H ₂ NCO	C ₁₀ H ⁺ (2023)	I-C ₃ H ₇ OH	1-c-C ₉ H ₈ CCH
SIS	HOC ⁺	HNCO	HCOOH	NH ₂ CHO	CH ₃ NCO	H ₂ NCH ₂ CN	CH ₃ CH ₂ SH	C ₂ H ₂ NH ₂ (?)	H ₂ C(C)H ₂ (2023)	(CH ₃) ₂ C=CH ₂ (2023)	2-c-C ₉ H ₈ CCH
NS	H ₂ O	HNCS	H ₂ CNH	C ₂ N	HC ₂ O	CH ₃ CHNH	CH ₃ NHCHO	HC ₇ NH ⁺			c-C ₃ H ₄ CCH ₂
C ₂ ⁺⁺	H ₂ S	HOCC ⁺	H ₂ C ₂ O	I-HC ₄ H ⁺	HOCH ₂ CN	CH ₃ SiH ₃	HC ₇ O	E-CH ₃ CHCHCN			2-C ₉ H ₇ CN
NO	HNC	H ₂ CO	H ₂ CN	I-HC ₄ N	HCCCHNH	H ₂ NC(O)NH ₂	HCCCHCHCN	Z-CH ₃ CHCHCN			C ₉ H ₂ CCH (2023)
HCl	HNO	H ₂ CN	HNC ₃	c-H ₂ C ₃ O	HC ₄ NC	HCCCH ₂ CN	H ₂ CCHC ₃ N	CH ₃ Cl(CN)CH ₂			CH ₃ OCH ₂ CH ₂ OH (2024)
NaCl	MgCN	H ₂ CS	SiH ₄ ⁺	H ₂ CCNH	c-C ₃ HCCH	HC ₃ NH ⁺	H ₂ CCCHCCH	CH ₂ CHCH ₂ CN			1-C ₁₂ H ₇ CN (2024)
KCl	MgNC	H ₃ O ⁺	H ₂ COH ⁺	C ₃ N ⁺	I-H ₂ C ₅	CH ₂ CHCCH	HOCHCHCHO (2024)	HOCH ₂ C(O)NH ₂ (2023)			5-C ₁₂ H ₇ CN (2024)
AlCl	N ₂ H ⁺	c-SiC ₃	C ₄ H ⁺	HNCHCN	MgC ₂ N	MgC ₃ H	HC ₇ N ⁺ (2024)	CH ₃ CH ₂ CCH (2024)			1-C ₁₀ H ₉ CN (2024)
AlF	N ₂ O	CH ₃ ⁺	HC(O)CN	SiH ₃ CN	CH ₂ C ₃ N	C ₂ H ₃ NH ₂	CH ₂ (CCH) ₂ (2024)				
PN	NaCN	C ₂ N ⁻	HNCNH	C ₃ S	NC ₂ NH ⁺ (2023)	(CHOH) ₂					
SiC	OCS	PH ₃	CH ₃ O	MgC ₄ H	MgC ₃ N ⁺ (2023)	HC ₂ (H)C ₄					
CP	SO ₂	HCNO	NH ₄ ⁺	CH ₃ CO ⁺	HC ₂ N ⁺ (2024)	C ₇ N ⁻ (2023)					
SiN	CO ₂ ⁺	HSCN	NCCNH ⁺	H ₂ C ₃ S	CH ₂ (CN) ₂ (2024)	MgC ₃ H ⁺ (2023)					
SO ⁺	NH ₂	H ₂ O ₂	CH ₃ Cl	HCCOHS		Z-(CH) ₂ (CN) ₂ (2024)					
CO ⁺	H ₃ ⁺⁺	C ₃ H ⁺	MgC ₃ N	C ₃ O							
HF	SiCN	HMgNC	NH ₂ OH	C ₃ H ⁺							
SiH [?]	AlNC	HCCO	HC ₃ O ⁺	HCCNCH ⁺							
FeO [?]	SiNC	CNCN	HC ₃ S ⁺	c-C ₃ C ₂ H							
O ₂	HCP	HONO	H ₂ C ₂ S	HC ₄ S							
CF ⁺	CCP	MgC ₂ H	C ₄ S	HMgC ₃ N (2023)							
PO	AlOH	HCCS	HC(O)SH	MgC ₄ H ⁺ (2023)							
AlO	H ₂ O ⁺	HNCN	HC(S)CN	H ₂ C ₃ H ⁺ (2023)							
OH ⁺	H ₂ Cl ⁺	H ₂ NC	HCCCO	H ₂ C ₃ N (2023)							
CN ⁺	KCN	HCCS ⁺	NaCCCN (2023)	(HO) ₂ CO (2023)							
SH ⁺	FeCN	CH ₃ ⁺ (2023)	MgC ₃ N ⁺ (2023)	H ₂ CN(CN) (2024)							
SH	HO ₂	HCNS (2024)	HC ₃ N ⁺ (2024)	NCHCCS (2024)							
HCl ⁺	TiO ₂	HOCS ⁺ (2024)	HC ₃ S (2024)								
TiO	C ₂ N	HNSO (2024)	NC ₃ S (2024)								
AlH ⁺	Si ₂ C										
N ₂	HS ₂										
NO ⁺	HCS										
NS ⁺	HSC										
HeH ⁺	NCO										
PO ⁺	CaNC										
SiP [?]	NCS										
FeC (2023)	MgC ₂										
MgS (2024)	HSO (2023)										
NaS (2024)	CaC ₂ (2024)										

“more than 320 molecules

As of November 2024, 327 molecules are listed

Extragalactic Molecules (as of 03/2024)

2 atoms	3 atoms	4 atoms	5 atoms	6 atoms	7 atoms	8 atoms	>8 atoms
OH	H ₂ O	H ₂ CO	c-C ₃ H ₂	CH ₃ OH	CH ₃ CCH	HC ₆ H	c-C ₆ H ₆ *
CO	HCN	NH ₃	HC ₃ N	CH ₃ CN	CH ₃ NH ₂	HC(O)OCH ₃	C ₆₀ * (?)
H ₂ *	HCO*	HNCO	CH ₂ NH	HC ₄ H*	CH ₃ CHO		(CH ₃) ₂ O
CH	C ₂ H	C ₂ H ₂ *	NH ₂ CN	HC(O)NH ₂	C ₂ H ₃ CN		
CS	HNC	H ₂ CS?	I-C ₃ H ₂	CH ₃ SH			
CH*	N ₂ H*	HOCO*	H ₂ CCN				
CN	OCS	c-C ₃ H	H ₂ CCO				
SO	HCO	H ₃ O*	C ₄ H				
SiO	H ₂ S	I-C ₃ H	HCOOH				
CO*	SO ₂	C ₃ N	C ₂ H ₃ * (2024)				
NO	HOC*	I-C ₃ H*					
NS	C ₂ S	H ₂ CN					
NH	H ₂ O*	H ₂ NC					
OH*	HCS*						
HF	H ₂ Cl*						
SO*	NH ₂						
ArH*							
CF*							
SH*							
O ₂ (?)							
PN							

Very low collision energies

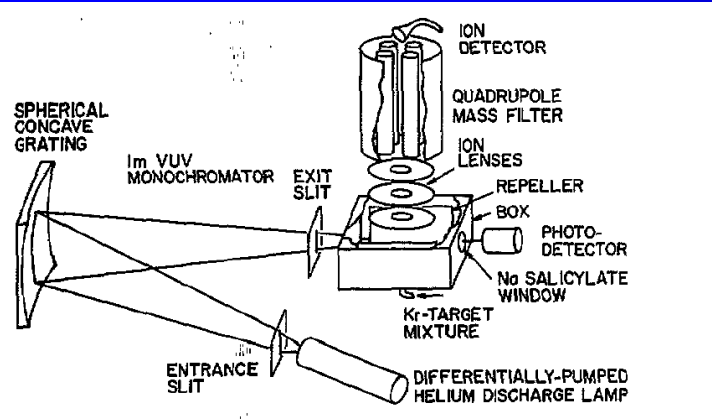
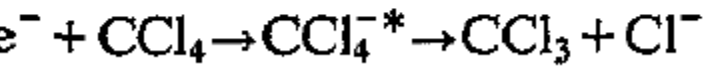
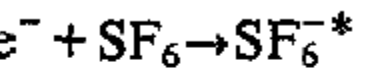
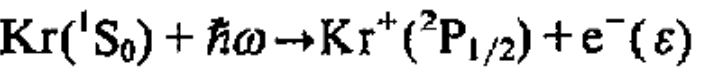
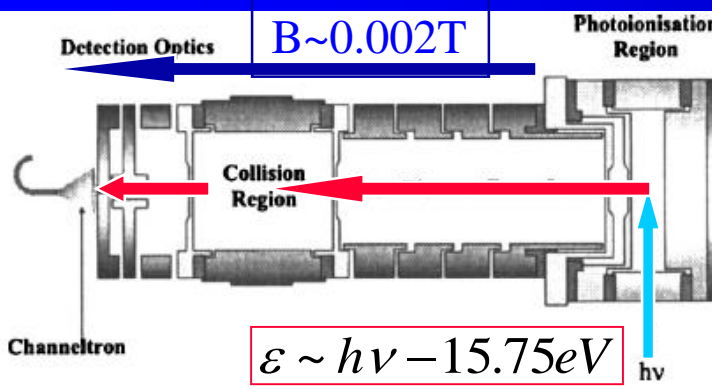


Figure 1. Schematic diagram of the vuv photoionization apparatus used for attachment studies (Chutjian and Alajajian 1985a, b).



TOPICAL REVIEW

J. Phys. B: At. Mol. Opt. Phys. 28 (1995) 1645-1672. Printed in the UK

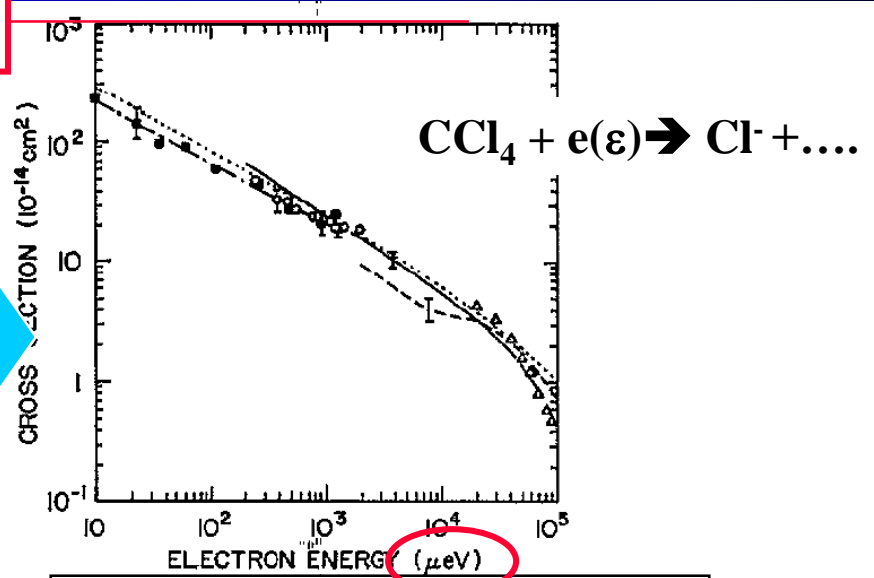
Electron-molecule collisions at very low electron energies

1995

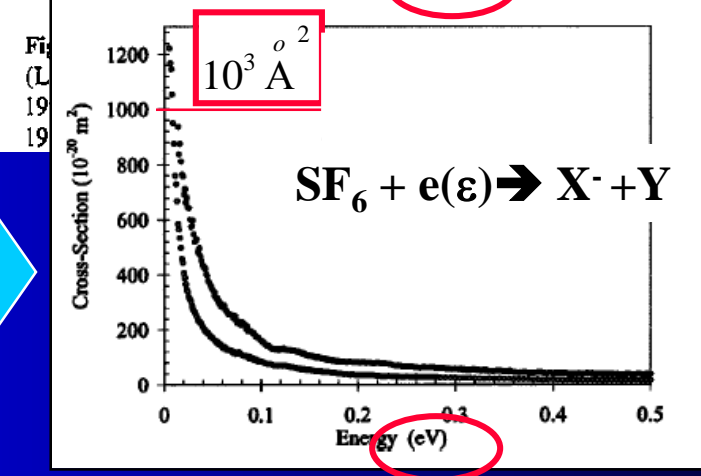
F B Dunning

Department of Physics and the Rice Quantum Institute, Rice University, PO Box 1892, Houston, TX 77251, USA

$10^5 \text{ } \overset{o}{\text{A}}$



1995



2004

$10^3 \text{ } \overset{o}{\text{A}}$

Fig. 19. (—) $\sigma_e(v) - \text{K}(np)$; (---) $\sigma_e(v) - \text{K}(np)$ free electrons (Klar et al); (---) $\sigma_e(v) - \text{K}(np)$ free electrons (Pai et al)

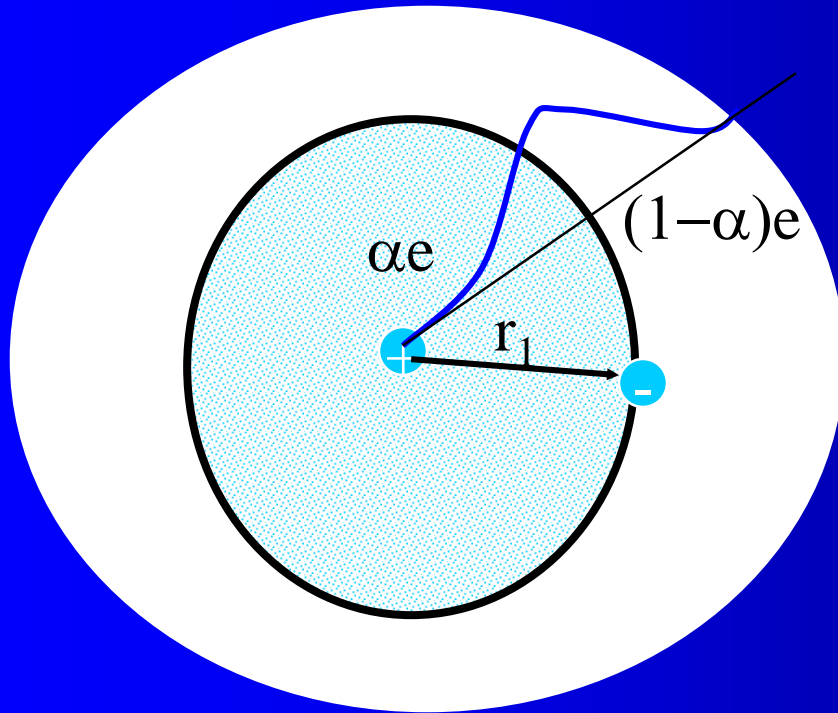
Negative ions

Interaction of electrons with atoms and molecules

Formation of negative ions attachment

Existence of negative ions

It is in case of H⁻ second electron in the field of proton and first electron



+e



-alpha e



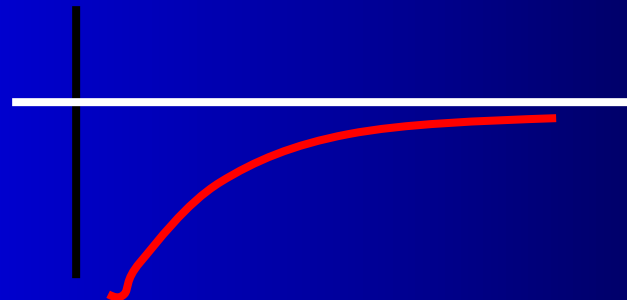
$$V_{\text{within}} = -(1-\alpha)e/r_1$$

$$\beta < 1$$

$$V_{\text{out}} = \beta(1-\alpha)e/r_1$$

Total potential energy of electron of the charge -e

$$U(r_1)_{\text{total}} = -(1-\beta)(1-\alpha)e^2/r_1$$



Calculation of H⁻ potential

The calculation of the potential energy of an electron in the field of a hydrogen atom may be carried out to a first approximation as follows. If we neglect polarization effects (which are actually decisive in determining the stability of H⁻) the probability of finding the atomic electron at a distance between r and $r + dr$ from the nucleus is $4\pi r^2 \psi^2 dr$, where $\psi = (\pi a_0^3)^{-1/2} \exp(-r/a_0)$ is the wave function of the ground state of hydrogen. The potential energy due to the atomic electron at a point distant r_1 from the nucleus is

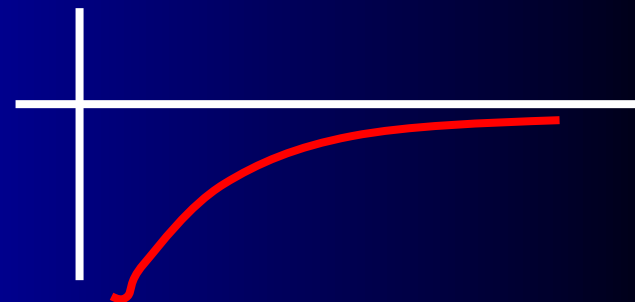
$$\frac{4\pi e^2}{r_1} \int_0^{r_1} \psi^2 r^2 dr + 4\pi e^2 \int_{r_1}^{\infty} \frac{\psi^2 r^2}{r} dr,$$

the first term arising from the charge within r_1 , the second from that without. Carrying out the elementary integrations involved gives

$$e^2 \left\{ \frac{1}{r_1} - \exp(-2r_1/a_0) \left(\frac{1}{r_1} + \frac{1}{a_0} \right) \right\}.$$

Adding the potential energy $-e^2/r_1$ due to the nucleus we find for the total potential energy

$$-e^2 \exp(-2r_1/a_0) \left(\frac{1}{r_1} + \frac{1}{a_0} \right). \quad (1.1)$$

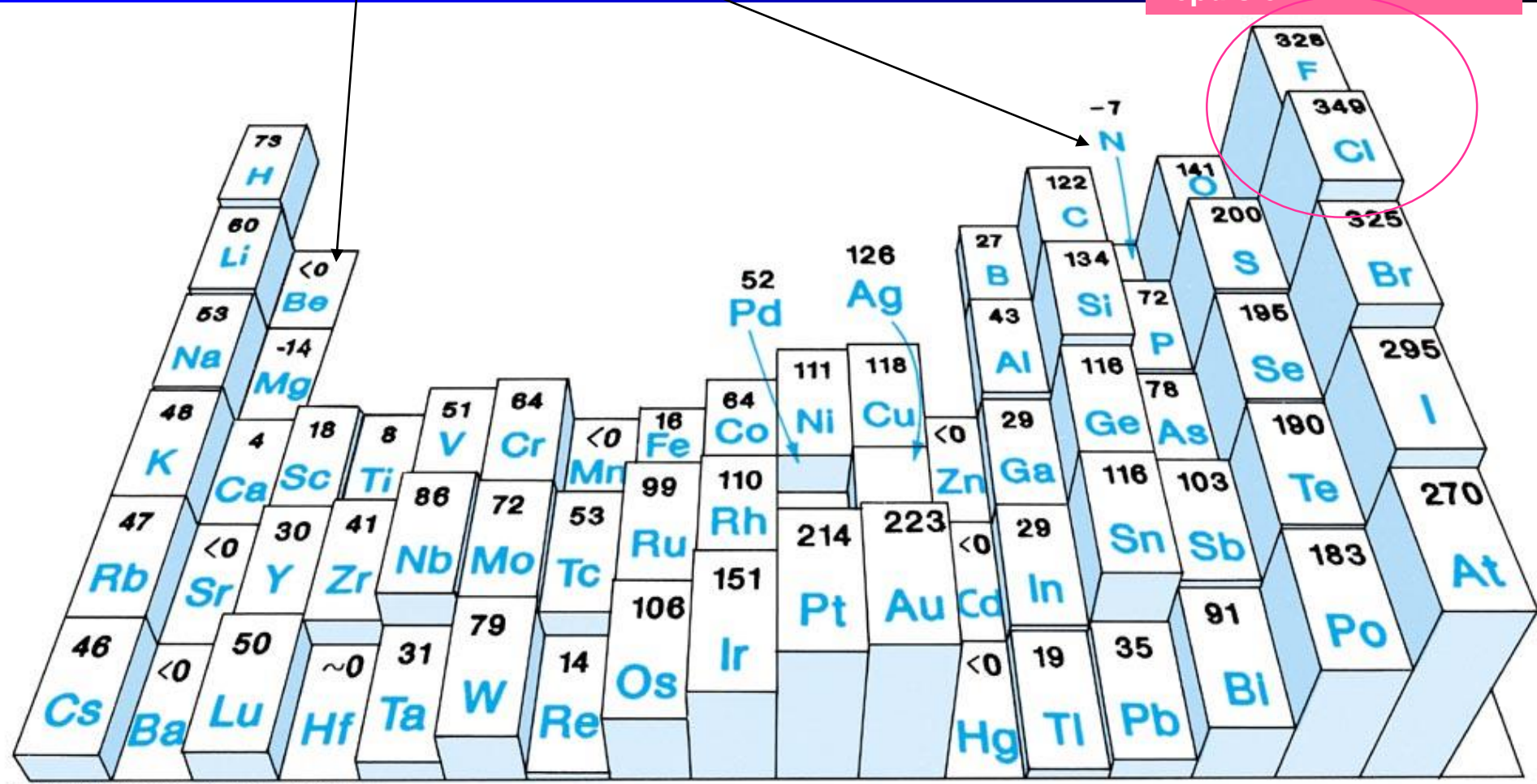


Electron Affinity : Attraction of e^- to neutral atom kJ/mol

96kJ/mol \sim 1eV

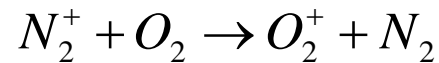
Exceptions: Be (EA < 0), N (EA < 0)

$|EA(Cl)| > |EA(F)|$?
Small F atom, greater e^- repulsion

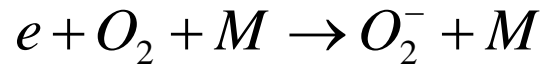


- The D Region

- The most complex and least understood layer in the ionosphere.
- The primary source of ionization in the D region is ionization by solar X-rays which ionize both N_2 and O_2
- Lyman- α ionization of the NO molecule.
- Precipitating magnetospheric electrons may also be important.
- Initial positive ions are N_2^+ , O_2^+ and NO^+



- The primary positive ions are O_2^+ and NO^+
- The most common negative ion is NO_3^-
 - The first step in making a negative ion is



Attachment (to molecule) and detachment

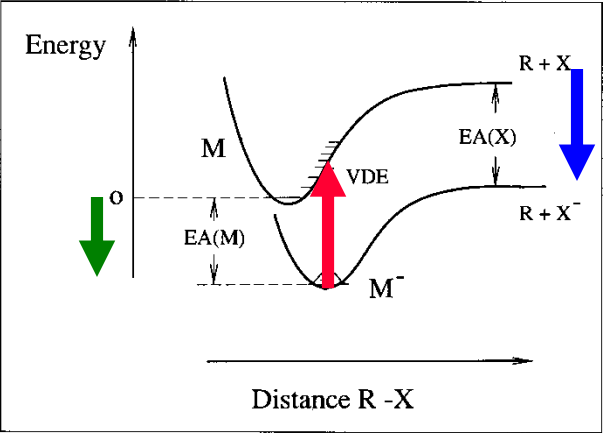


Fig. 1.1. Born-Oppenheimer potential energy curves illustrating electron affinity (EA) and vertical detachment energy (VDE).

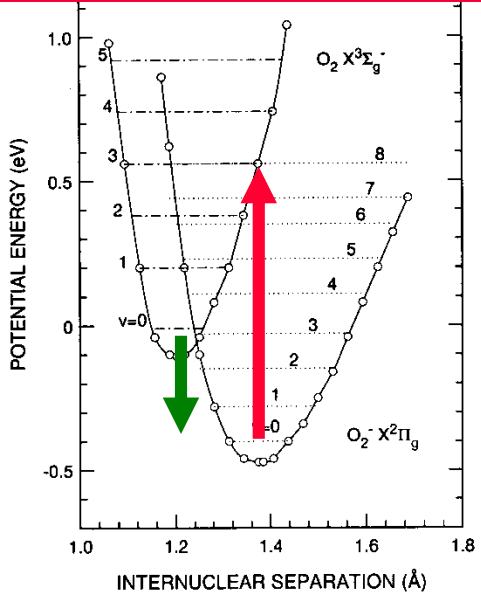


Figure 6-9-1. Approximate potential energy curves for O₂ and O₂⁻.

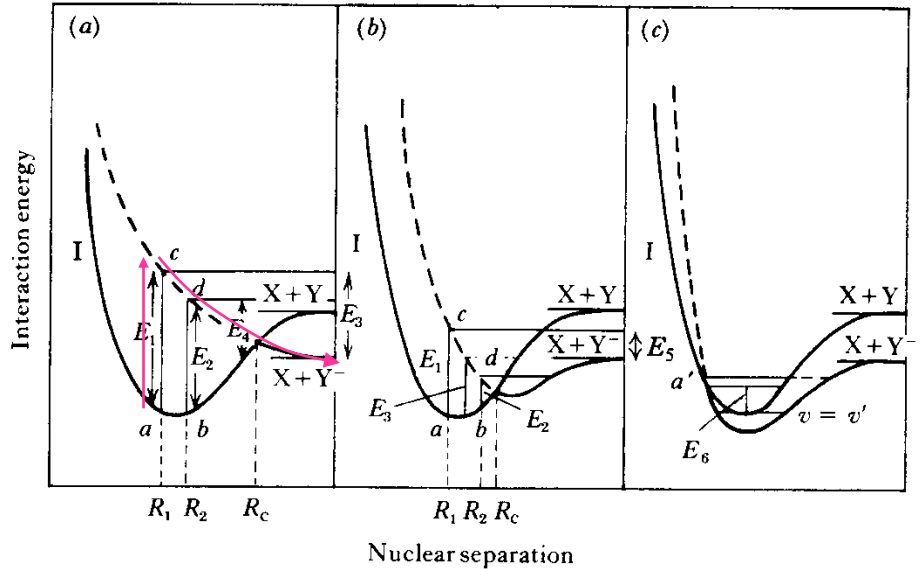


Fig. 9.1. Potential-energy curves illustrating three possible ways in which negative ions may be formed from a molecule XY by electron capture.

Photodetachment $O_2^- + h\nu \rightarrow O_2 + e$

Fig. 11.8 shows a typical arrangement used in the study of photodetachment from NO^- and O_2^- which is very similar to that used for He^- .

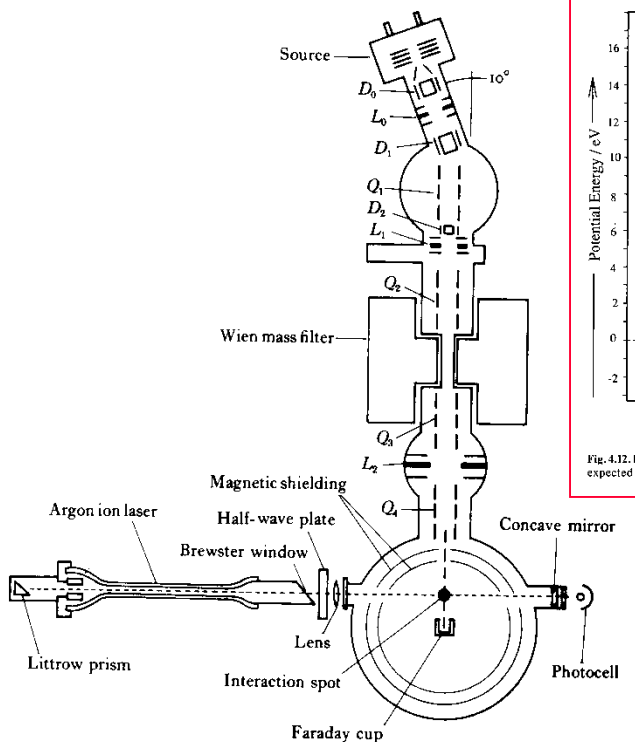
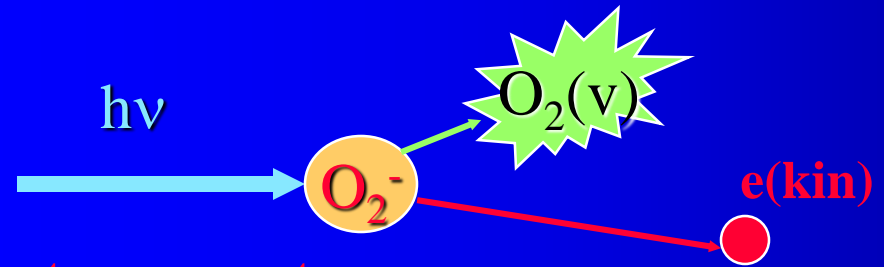


Fig. 11.8. Arrangement of the apparatus used for measurement of the angular and energy distribution of electrons resulting from photodetachment by laser light. From Siegel *et al.* (1972). D_0, D_1, D_2 , vertical and horizontal deflectors; L_0, L_1, L_2 einzel lenses; Q_1, Q_2, Q_3, Q_4 , twelve-element symmetrical quadrupole lenses.



Electron spectroscopy

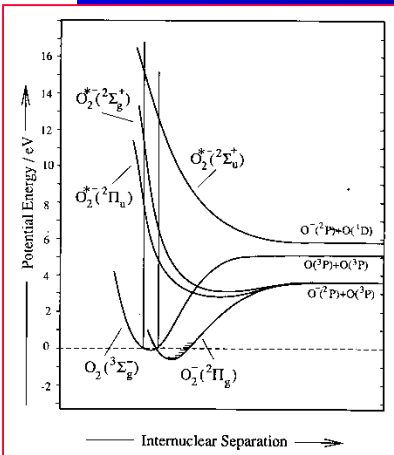


Fig. 4.12. Potential energy curves of O_2 and O_2^- . Only those negative ion states are shown which are expected to generate significant O yields via dissociative attachment.

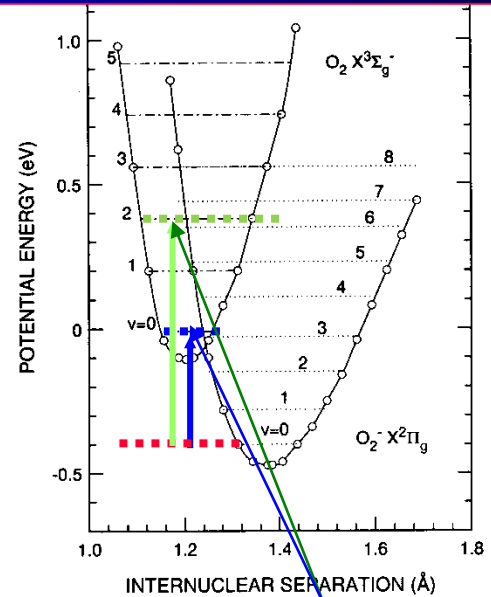


Figure 6-9-1. Approximate potential energy curves for O_2 and O_2^- .

Fig. 11.32 shows a typical photoelectron spectrum which they observed, using argon ion laser light at 4880 Å. It will be seen that there is evidence of two series of peaks, that the fourth and ninth

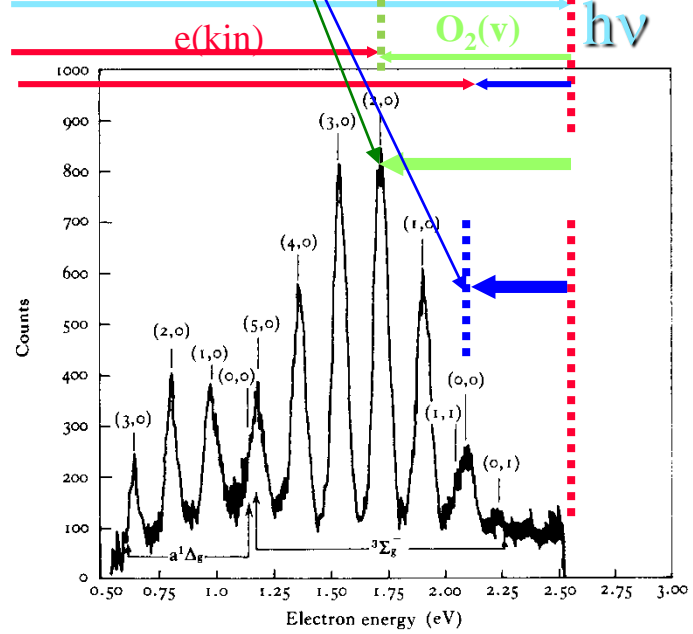


Fig. 11.32. Energy spectrum of the photoelectrons arising through photodetachment from O_2^- by argon ion laser light, as observed by Celotta *et al.* (1972).

Vibrational predissociation

Figure 1.10 illustrates vibrational predissociation. The coordinates Q_1 and Q_2 represent different molecular motions in a polyatomic molecule. The anion M^- formed on electron attachment has sufficient energy to dissociate but the energy is initially in vibrational modes that do not correspond to the reaction coordinate Q_2 .

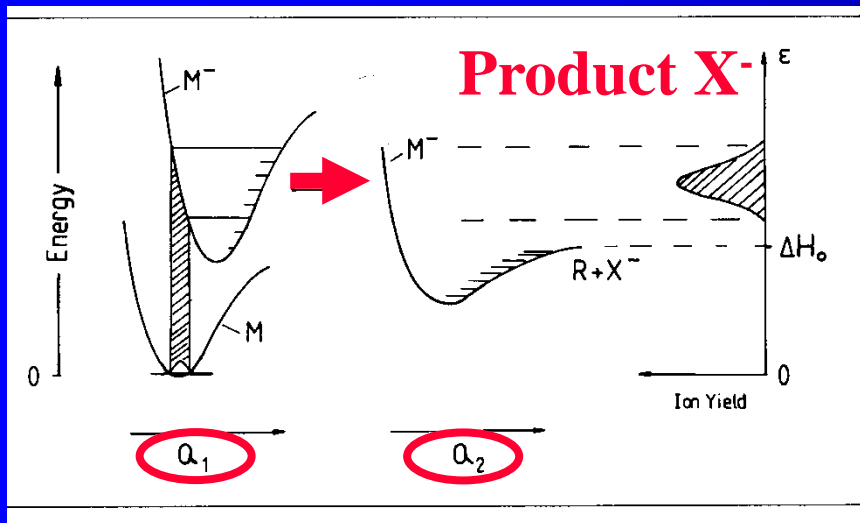


Fig. 1.10. Schematic potential energy curves illustrating dissociative electron attachment via vibrational predissociation. Q_1 and Q_2 represent different motions in a polyatomic ion.

Hydrogen molecule

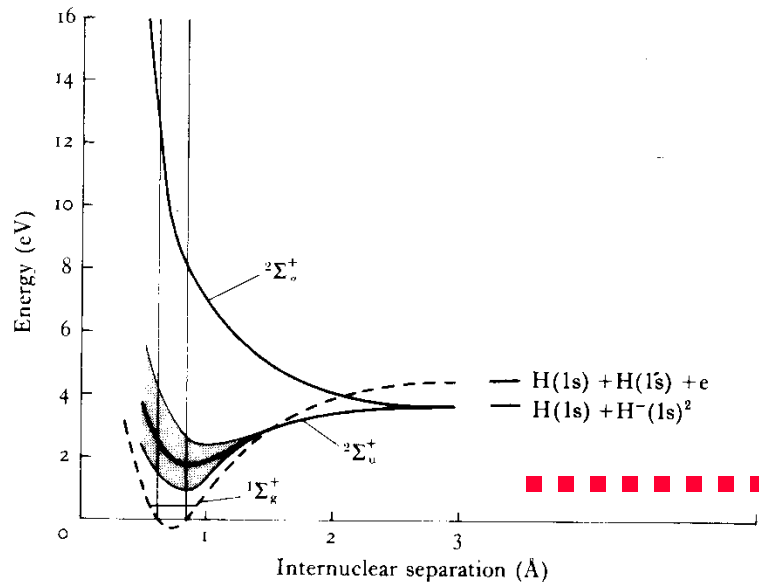
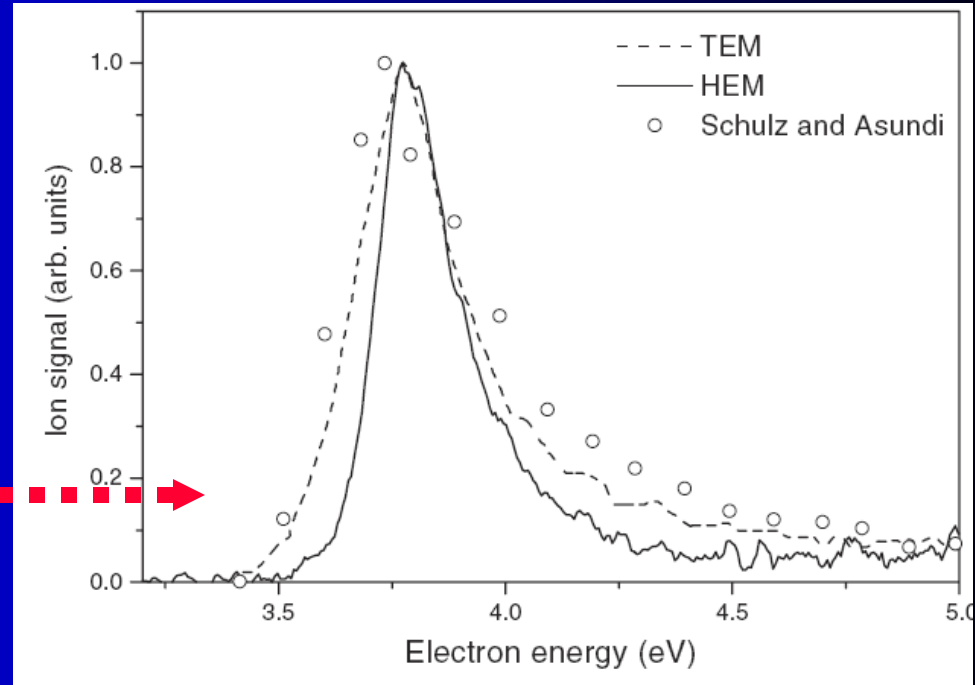


Fig. 9.23. Potential-energy curves of H_2^- responsible for dissociative attachment in H_2 . The broken curve is that for the ground Σ_g^+ state of H_2 .



The discovery of large concentrations of H^- ions (30%) in low-temperature hydrogen plasmas [1] has provided the possibility of producing intense beams of H^- ion sources for neutral beam heating [2, 3] of thermonuclear fusion devices [4, 5]. Modelling of such plasmas requires a detailed knowledge of the mechanism of dissociative electron attachment (DEA) of electrons to molecular hydrogen. Schematically the process may be written as a two-step process:



where ν and J denote the vibrational and rotational quantum numbers of the target hydrogen molecule. The incident electron is trapped by the neutral molecule in a resonant state, this trapping increasing the electron residence time sufficiently to allow the relatively slow moving nuclei to dissociate. In the present case the H_2^- ($1\sigma_g^2 1\sigma_u^2 + {}^2\Sigma_u^+$) resonance formed at a range of electron energies of around 4 eV is characterized by a very short lifetime against autodetachment when formed from the $\nu = 0$ level. Hence the cross section for product H^- is low.

Hydrogen molecule EA calculated by J. Horacek

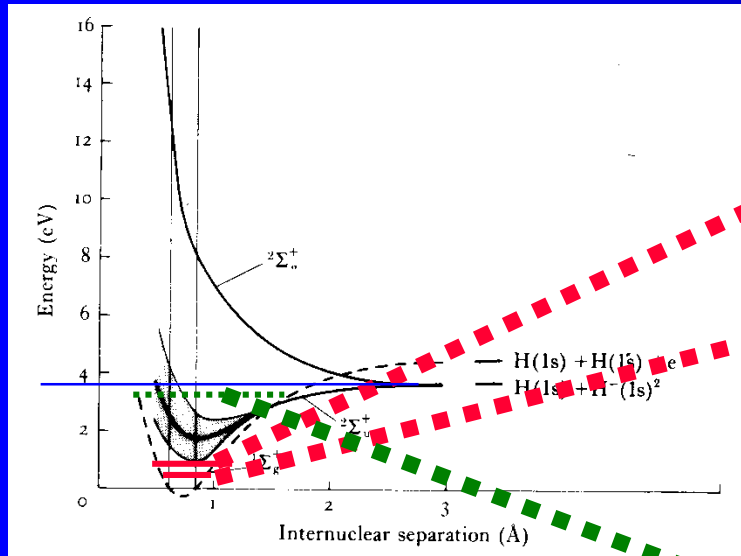


Fig. 9.23. Potential-energy curves of H_2^- responsible for dissociative attachment in H_2 . The broken curve is that for the ground Σ_g^+ state of H_2 .

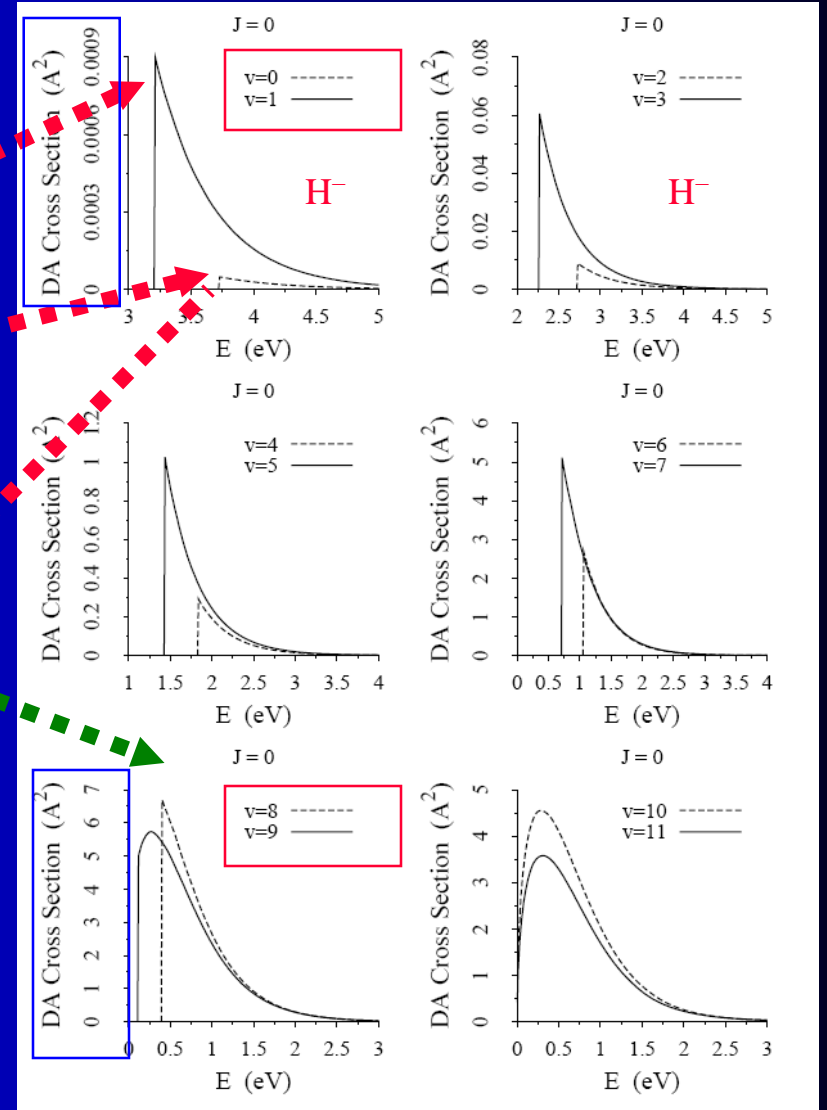
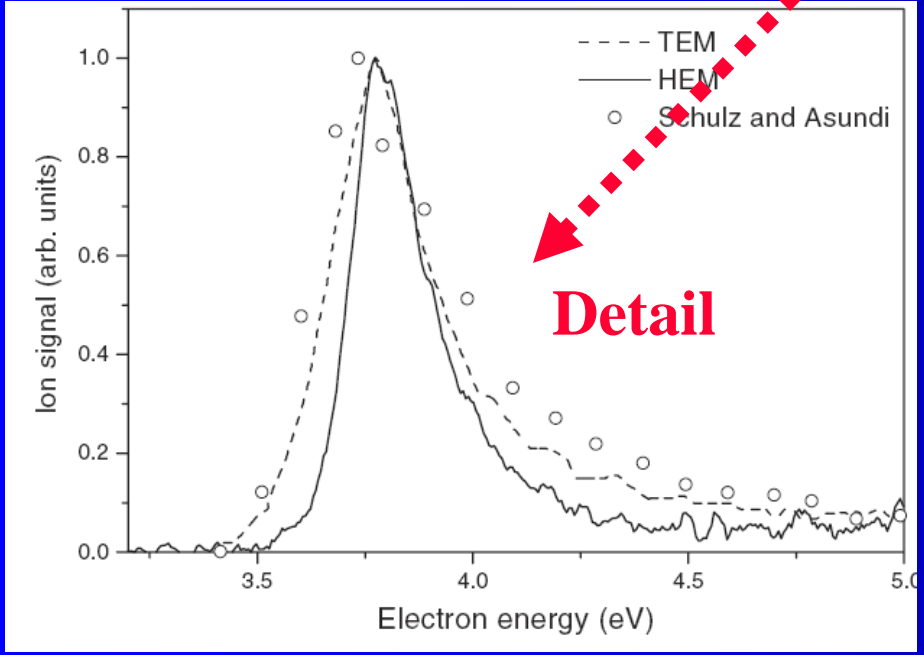


Figure 1: DA cross section for initial vibrational target states $v = 0, 1, \dots, 11$ for nonrotating hydrogen molecule.



Vibrational excitation of H_2
 $e^- + H_2(v, J) \rightarrow H_2^- \rightarrow H^- + H$

Hydrogen molecule

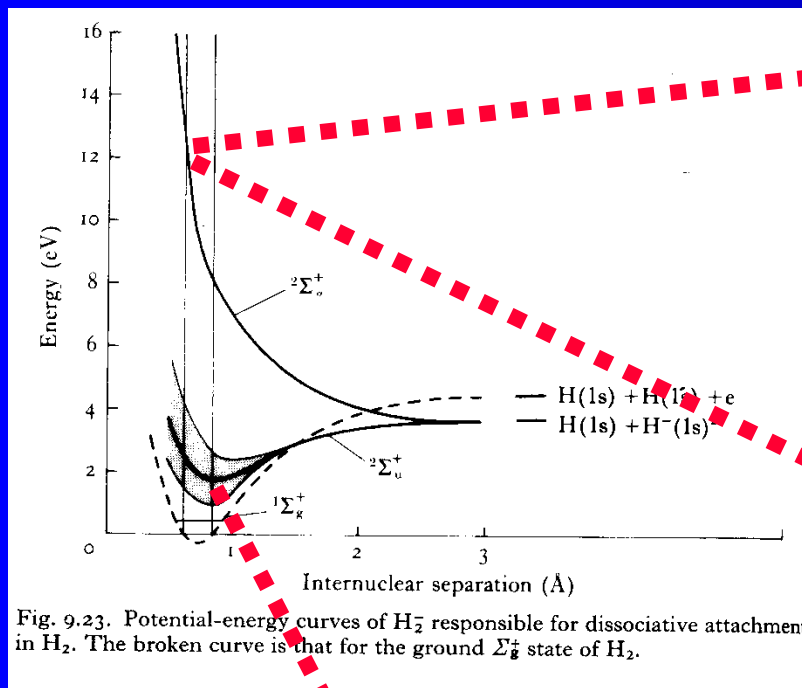


Fig. 9.23. Potential-energy curves of H_2^- responsible for dissociative attachment in H_2 . The broken curve is that for the ground Σ_g^+ state of H_2 .

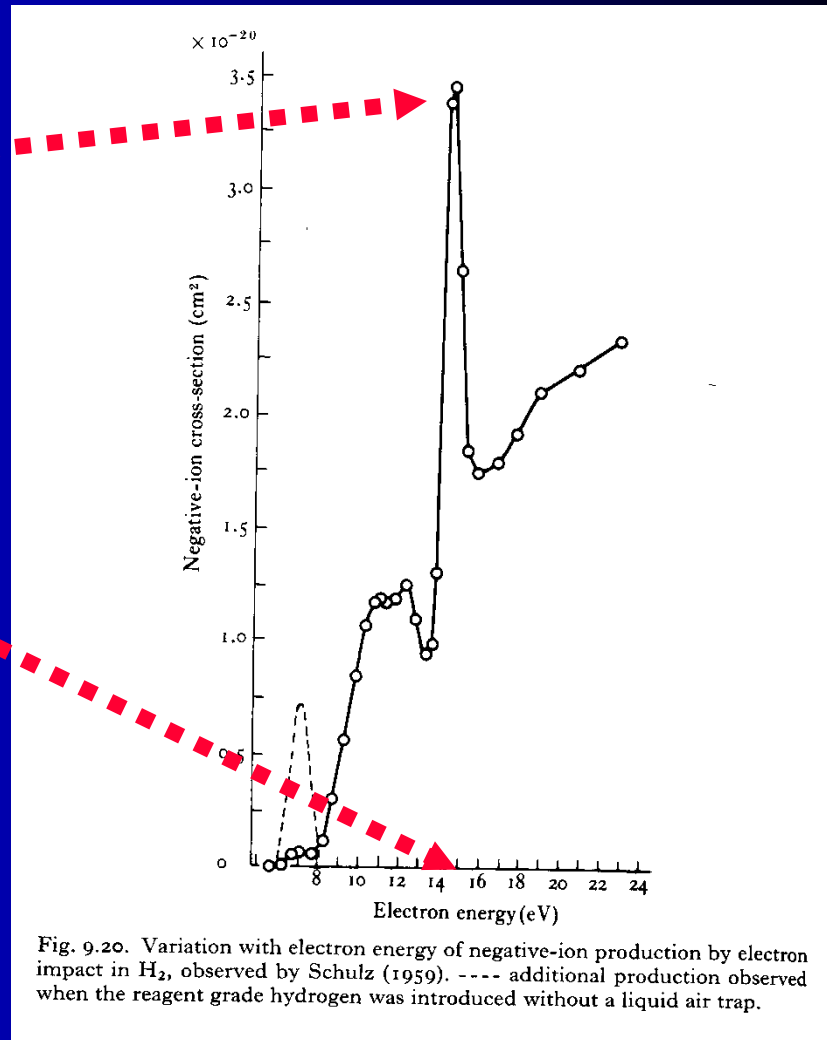
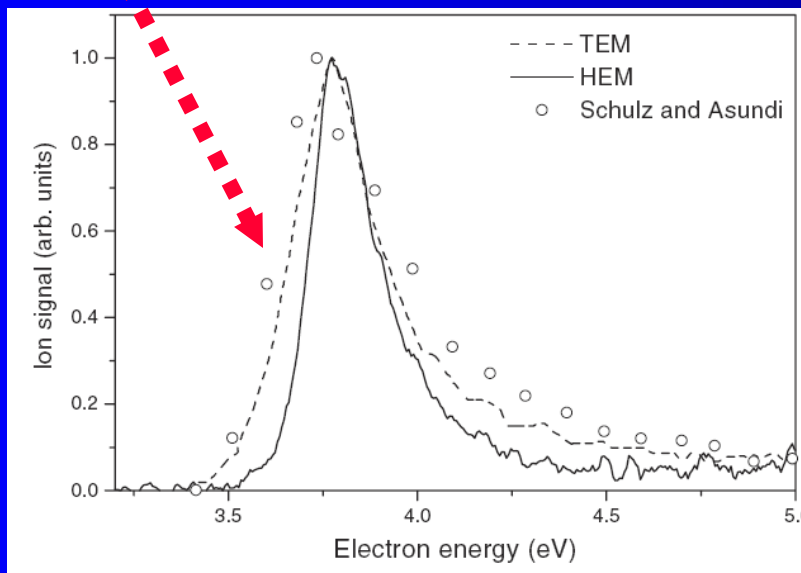


Fig. 9.20. Variation with electron energy of negative-ion production by electron impact in H_2 , observed by Schulz (1959). --- additional production observed when the reagent grade hydrogen was introduced without a liquid air trap.

Vibr. excitation of N_2 fine structure

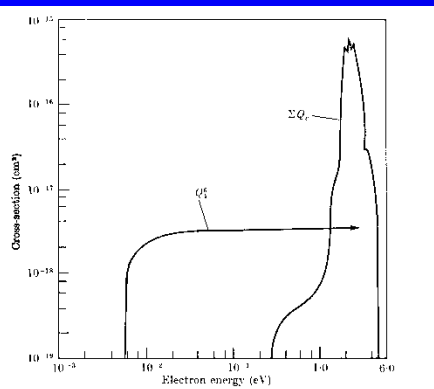


FIG. 11.31. Cross-sections for rotational and vibrational excitation of nitrogen. Q_4 is the cross-section for the rotational excitation $J = 4 \rightarrow J = 6$. ΣQ_4 is the sum of the cross-sections for vibrational excitation consistent with the swarm data.

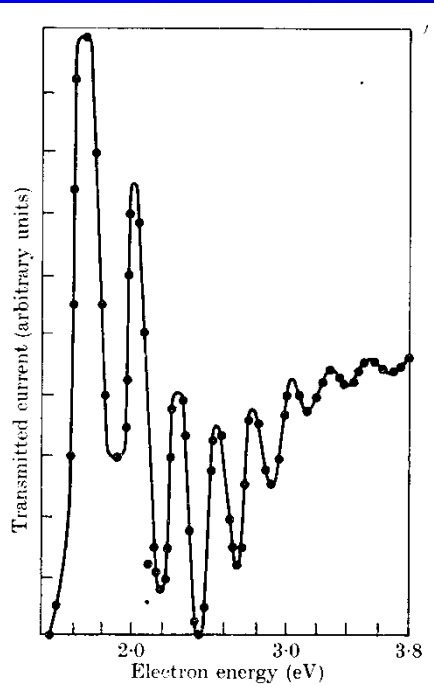


FIG. 10.32. Fine structure observed by Golden and Nakano in the transmission of electrons through N_2 . The points are obtained from a number of plots of the transmitted current. Because of electron optical effects no significance attaches to the relative magnitudes of peaks and troughs.

of a theory such as that outlined above. Haas suggested that we must regard the collisions as taking place in two stages—the incident electron is first captured to form a negative ion N_2^- that is energetically unstable but has a lifetime greater than a vibrational period. It eventually breaks up, becoming a neutral molecule that may be in an excited vibrational state—in other words, the process is regarded as a resonance of the same type as that found in elastic scattering of electrons by helium and other atoms and molecules (see Chap. 9).

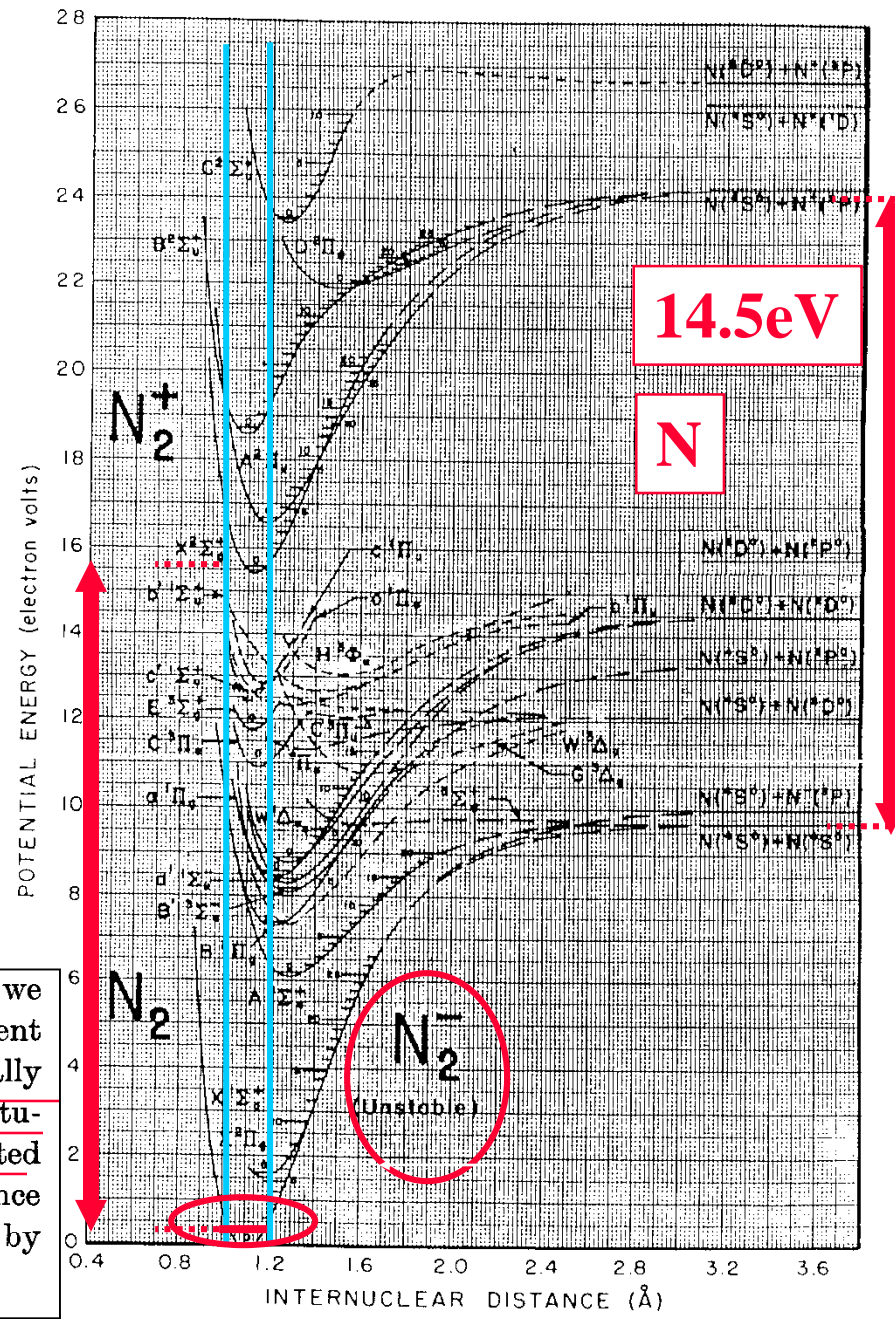


FIGURE 1. Potential energy curves for N_2 and N_2^- .

Rotational excitation N_2

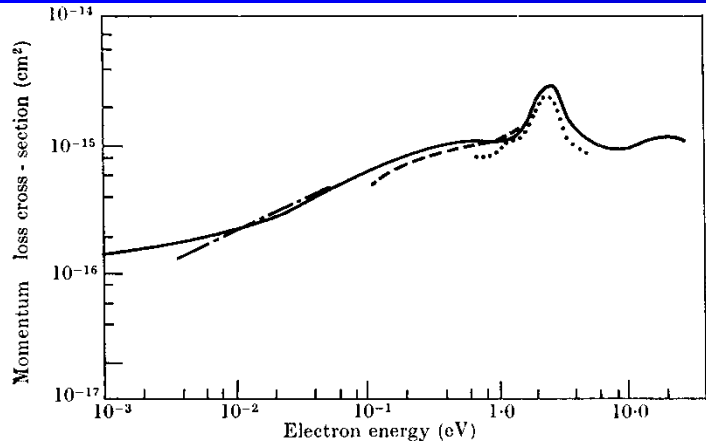


FIG. 11.30. Momentum-transfer cross-section for electrons in N_2 . — derived by Engelhardt, Phelps, and Risk from analysis of swarm data. - - - derived by Pack and Phelps from analysis of their drift velocity observations. - · - · derived from drift velocity observations of Crompton and Sutton. · · · total cross-section measured by Ramsauer method.

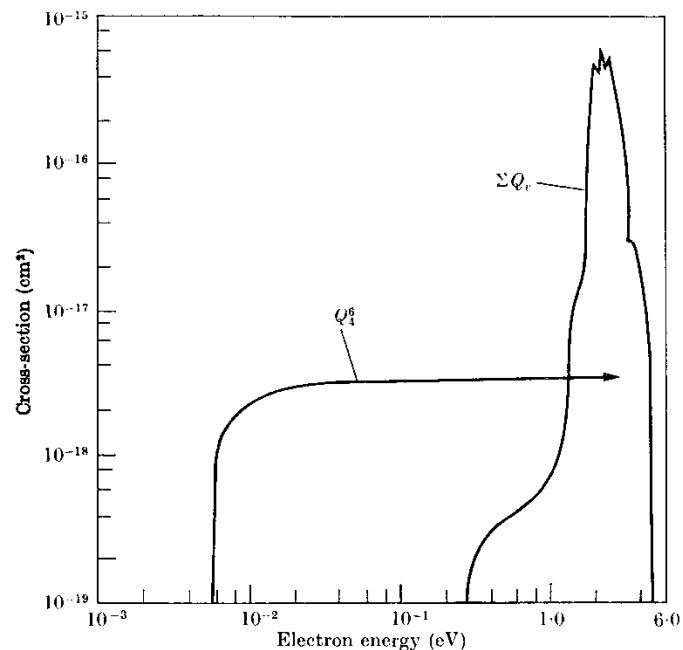


FIG. 11.31. Cross-sections for rotational and vibrational excitation of nitrogen. Q_4^6 is the cross-section for the rotational excitation $J = 4 \rightarrow J = 6$. $\Sigma_v Q_v$ is the sum of the cross-sections for vibrational excitation consistent with the swarm data.

106 EXCITATION, DISSOCIATION, AND ENERGY TRANSFER

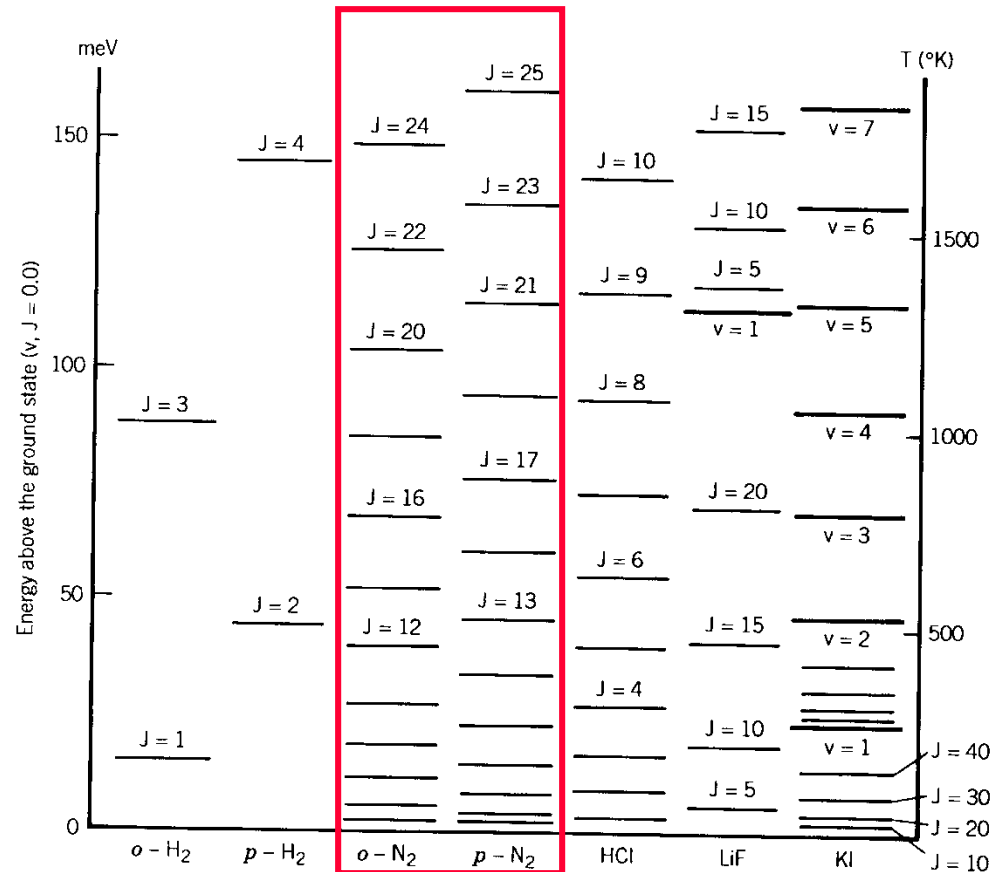
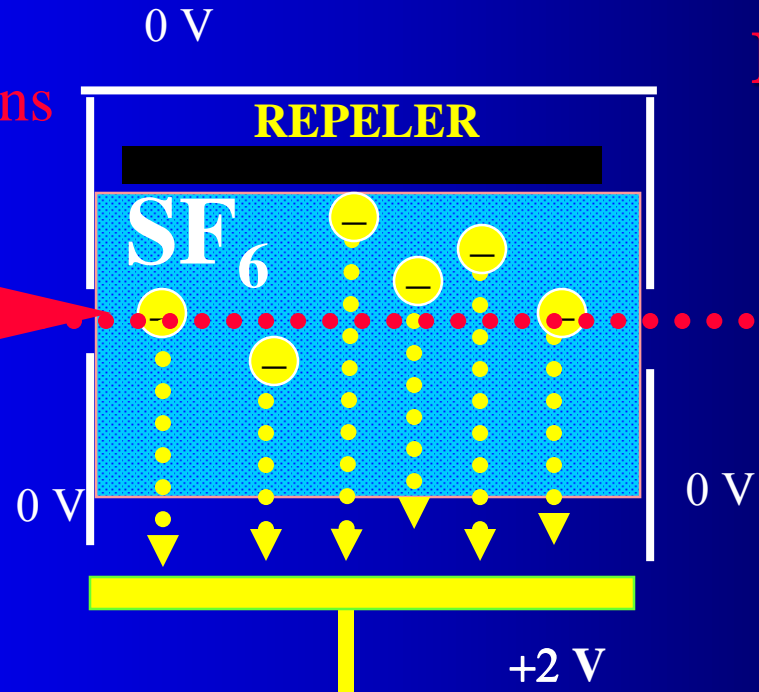
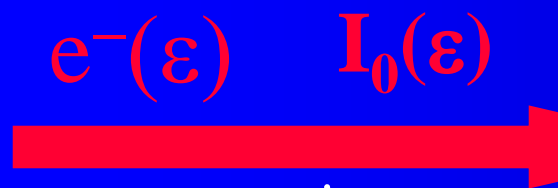


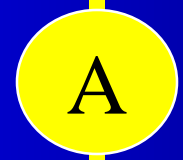
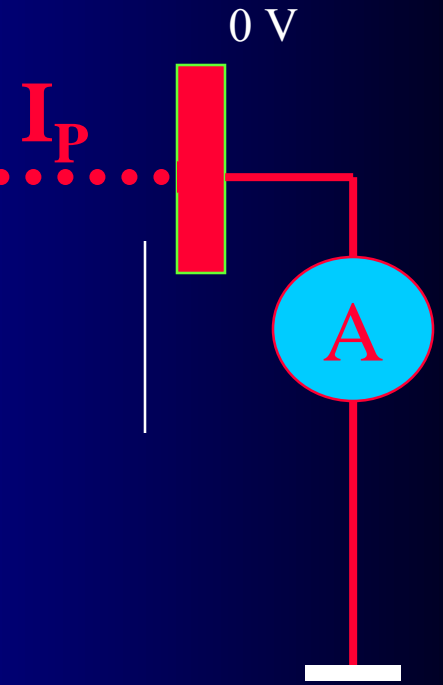
Figure 2-2-1. Vibrational-rotational levels (quantum numbers v and J) of a few diatomic molecules. The $(v = 1, J = 0)$ level of H_2 lies 0.54 eV above the ground state $(v = 0, J = 0)$. Rotational level spacings for H_2 are uniquely large, about $15J$ meV, where J is the quantum number for the upper level. For the ortho species of H_2 ($o-H_2$), the nuclear spins are parallel; for the para version ($p-H_2$), the nuclear spins are antiparallel. [From Shimamura (1984).]

Cross section of electron attachment – idea of experiment

Mono energetic electrons

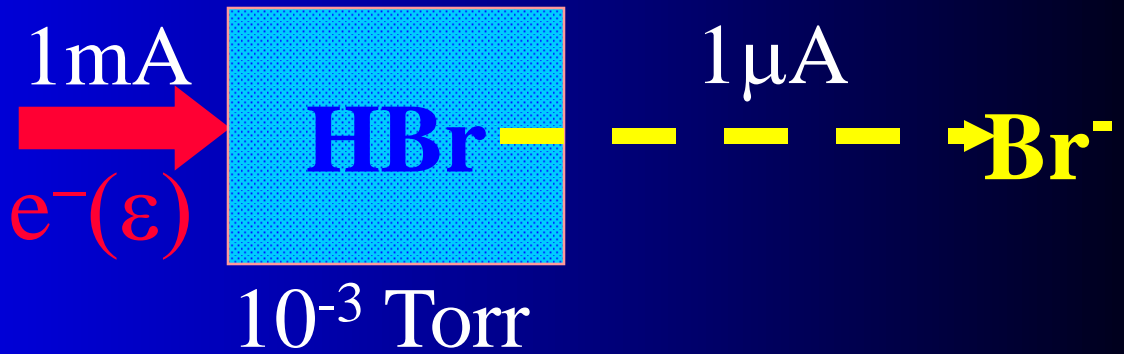
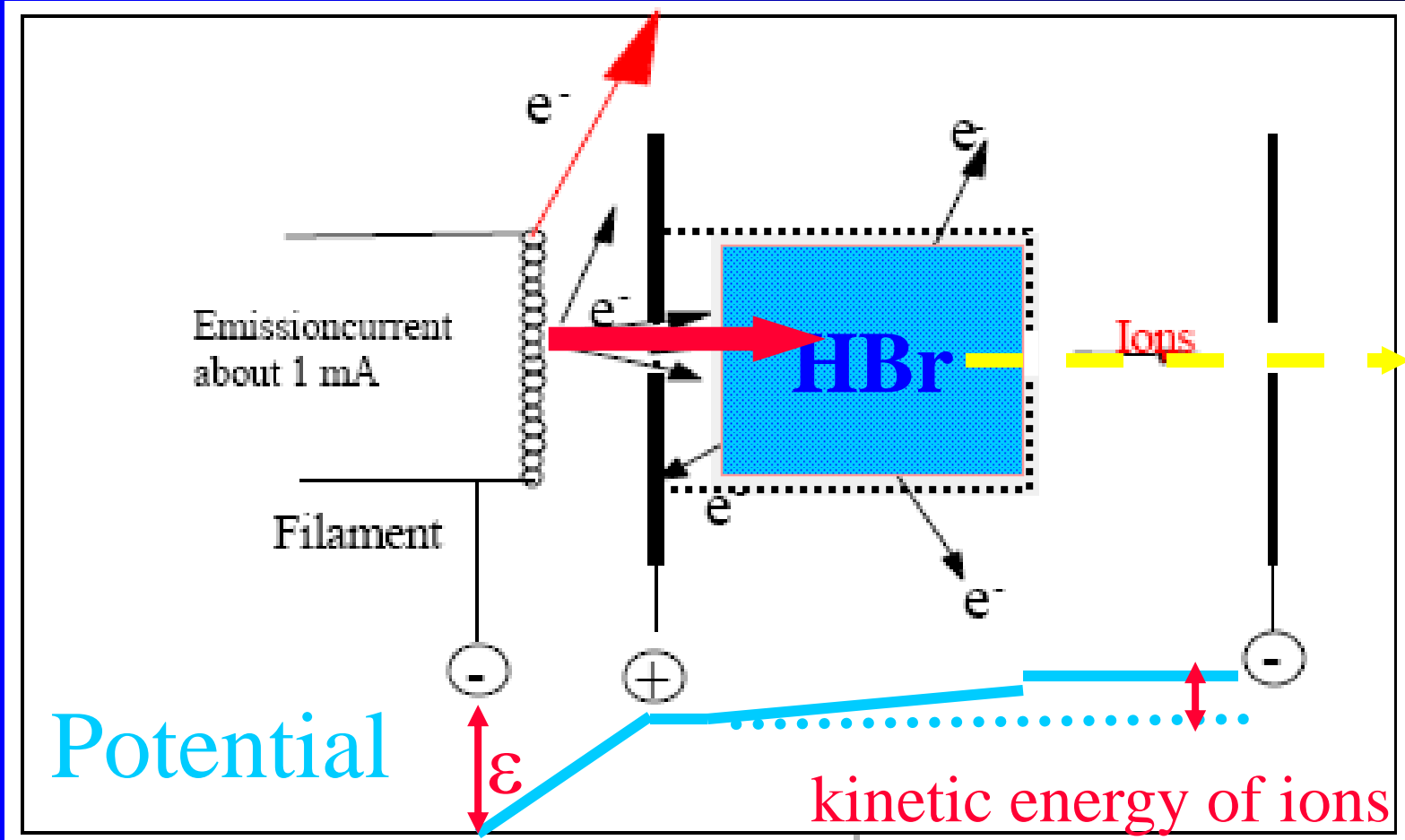


$$I_p = I_0 \exp(-\sigma N x)$$



$F^-, SF_5^-, SF_6^- \dots$

Electron attachment to HBr



EA to CCl_2F_2 absolute cross section

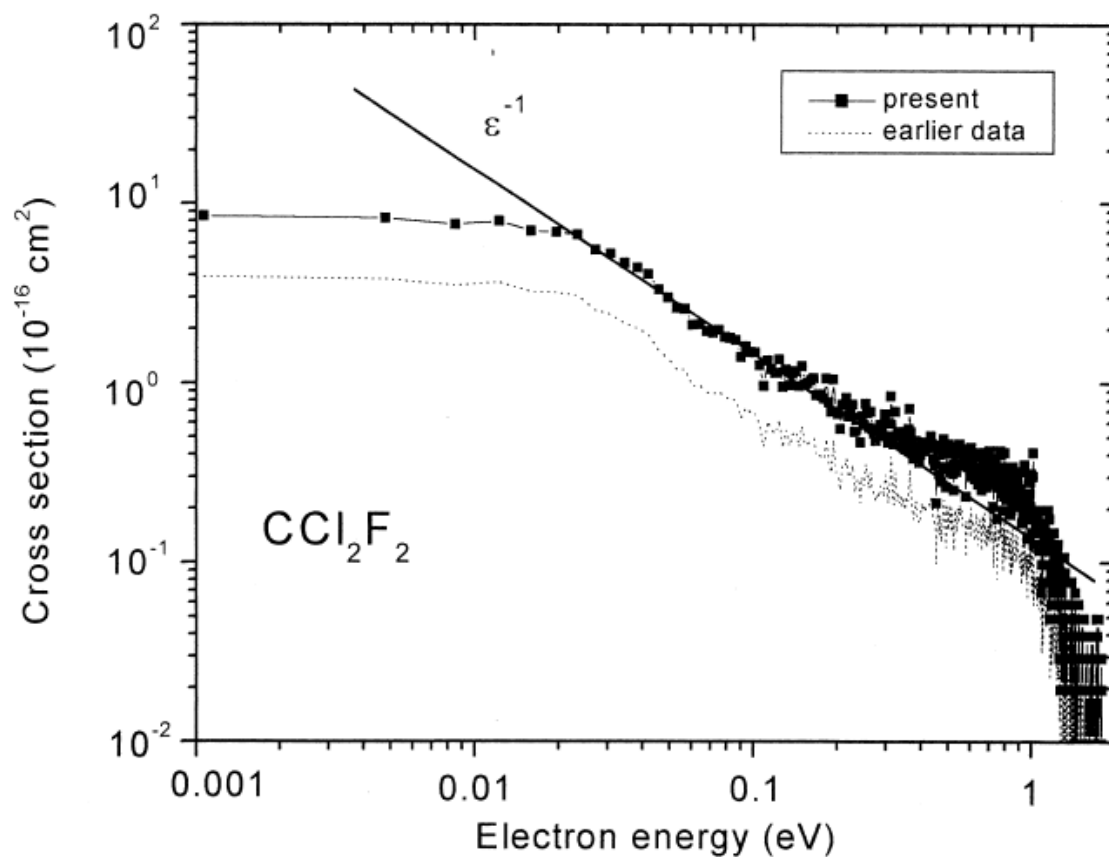


Fig. 1. Absolute electron attachment cross section vs. electron energy for the reaction $\text{CCl}_2\text{F}_2 + e \rightarrow \text{Cl}^-$. The present data (full line with full squares) were derived by using the calibration method outlined in the text [Eqs. (4) and (5)] involving integration of the measured anion signal. The earlier data (dashed line) are from [17] and have been obtained by [17] using the simple procedure employing Eq. (7). Also shown as full line designated ϵ^{-1} the predicted energy dependence for s-wave scattering.

Cross sections comparison

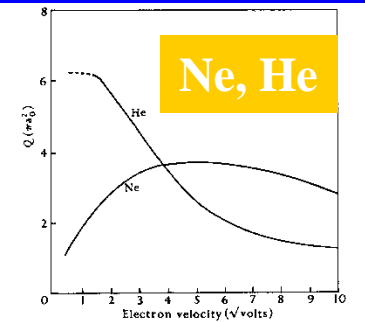


Fig. 1.10. Observed total collision cross-sections of He and Ne.

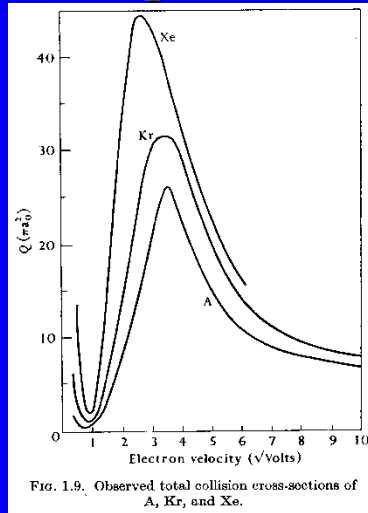


Fig. 1.9. Observed total collision cross-sections of A, Kr, and Xe.

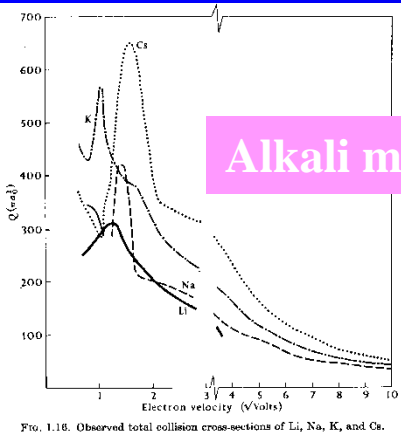
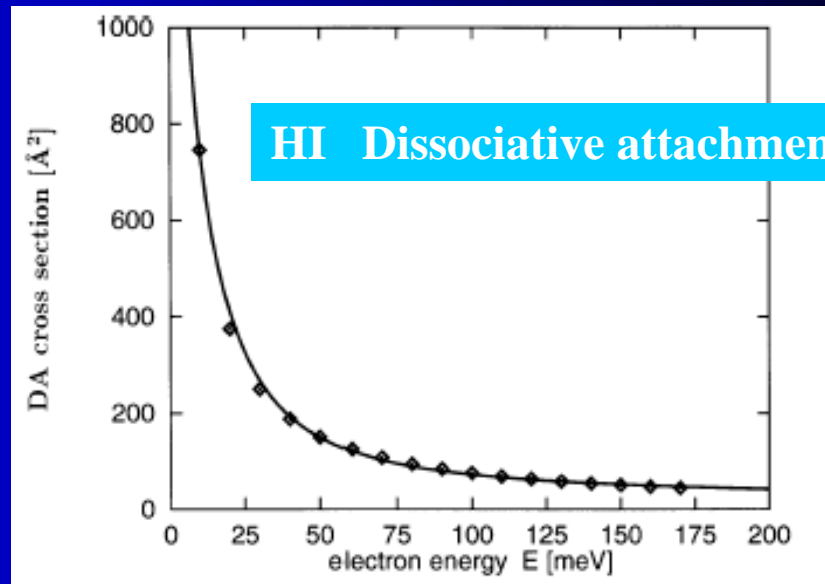


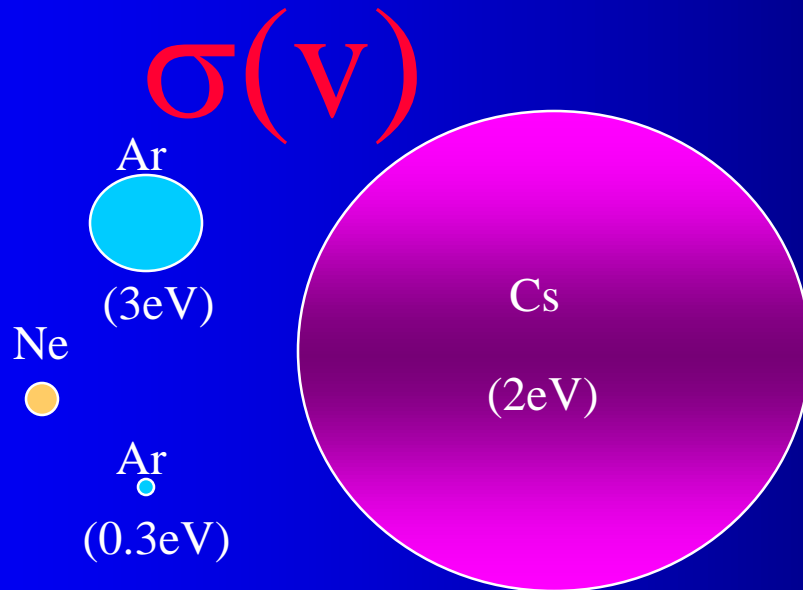
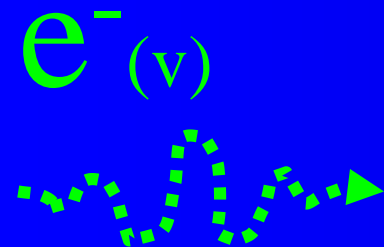
Fig. 1.18. Observed total collision cross-sections of Li, Na, K, and Cs.

Alkali metals



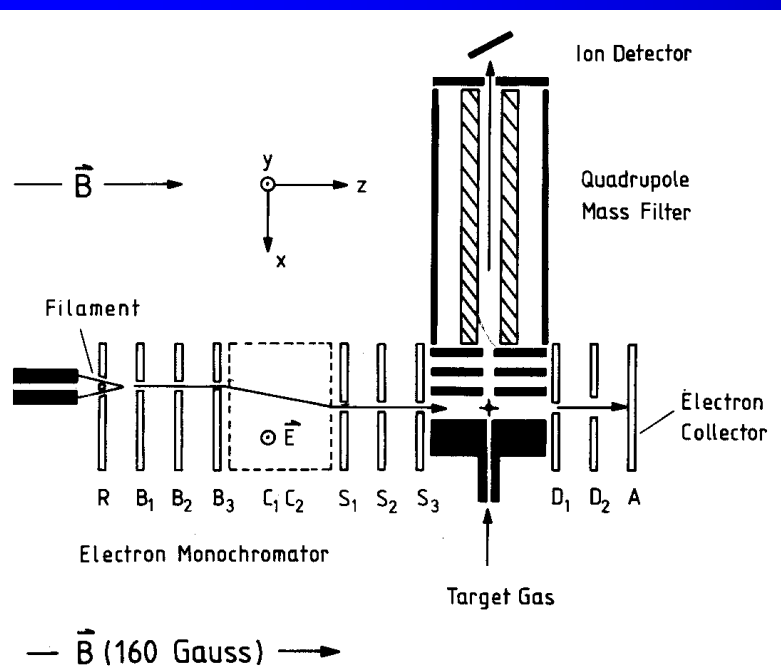
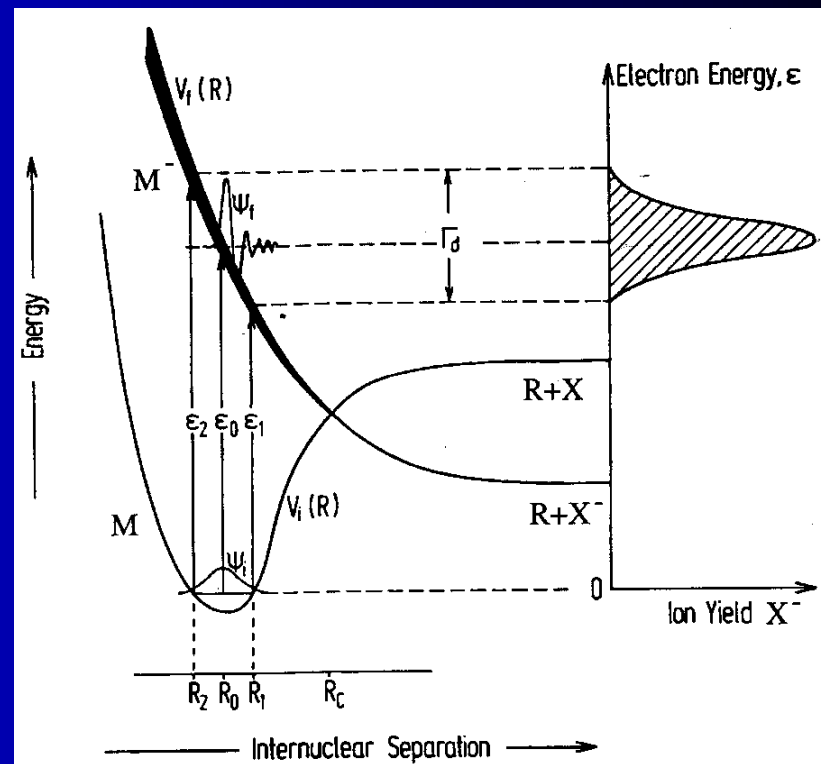
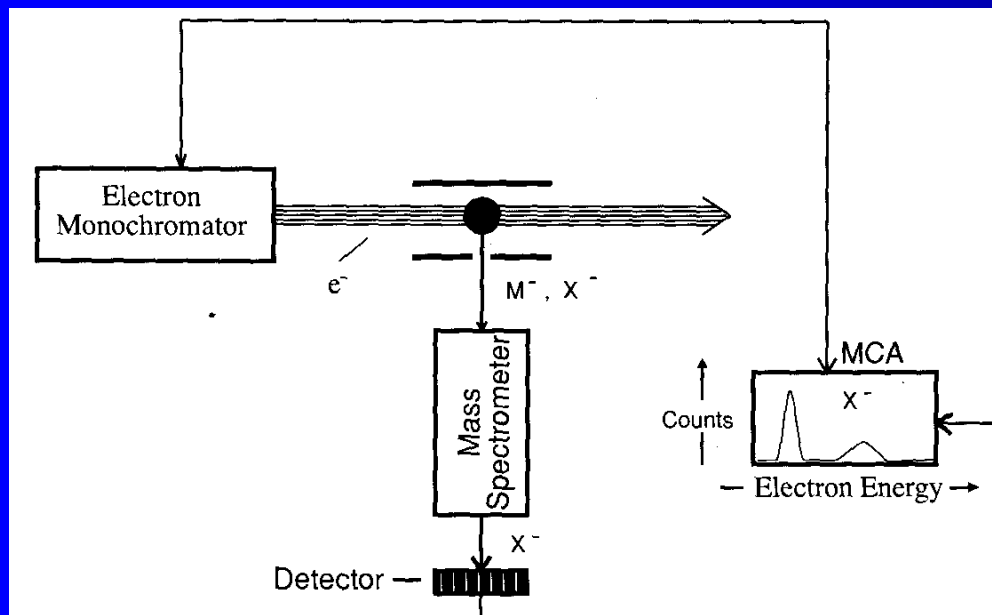
HI Dissociative attachment

Calculated DA cross section in HI (full curve). Diamonds represent the experimental data of Klar et al. [24]

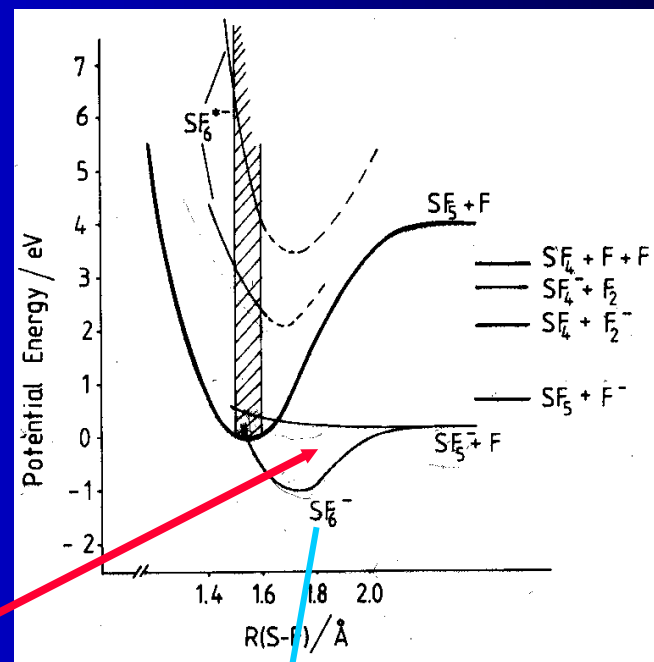
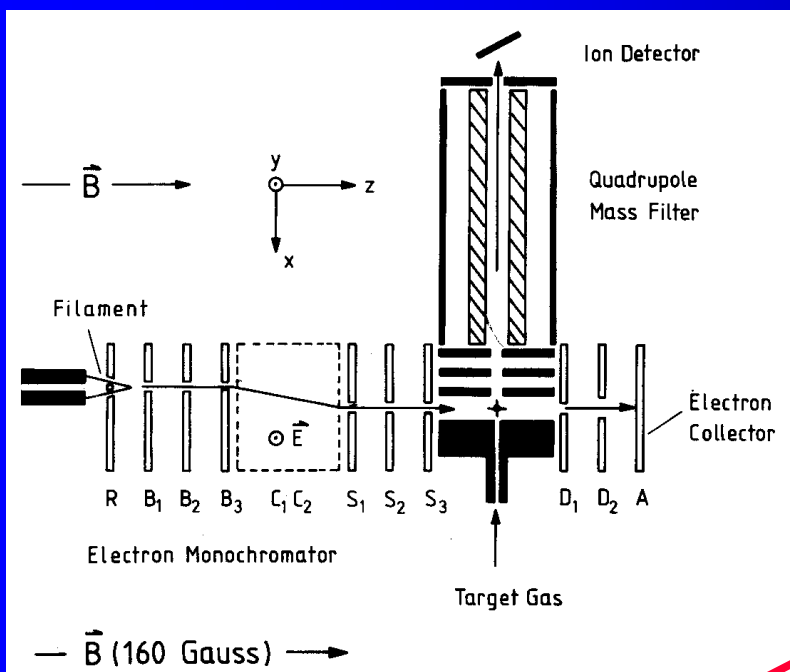


Attachment
HI
20meV

Electron Attachment Spectroscopy (EAS)



Electron Attachment Spectroscopy – electron energy distribution



Three-body attachment

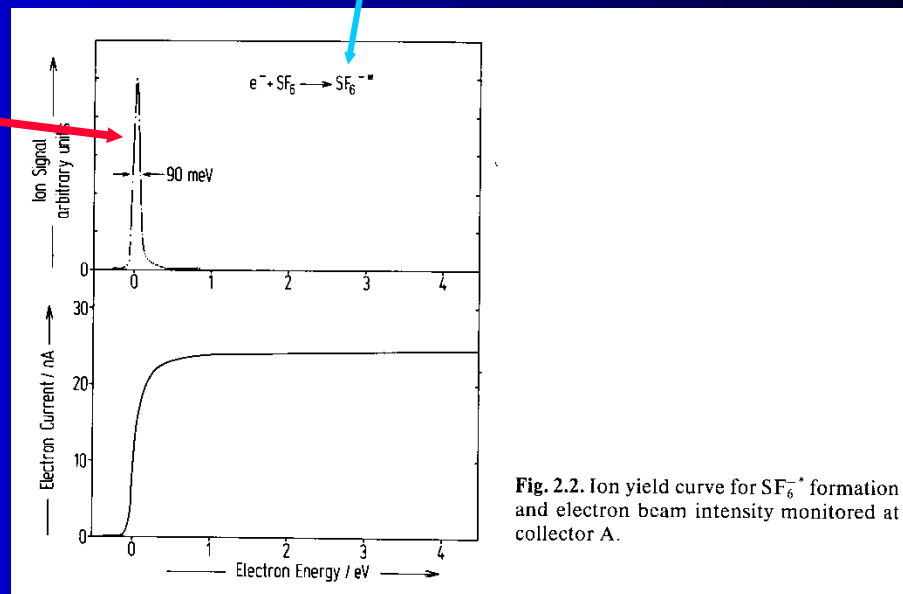
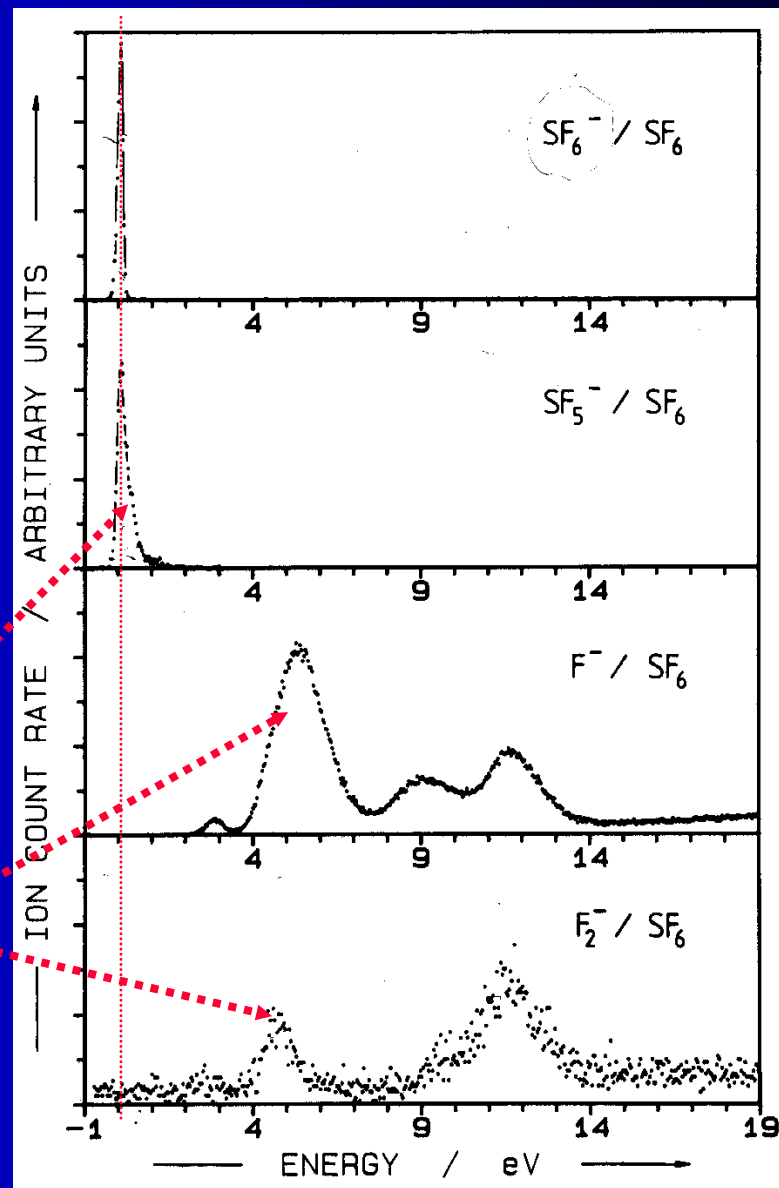
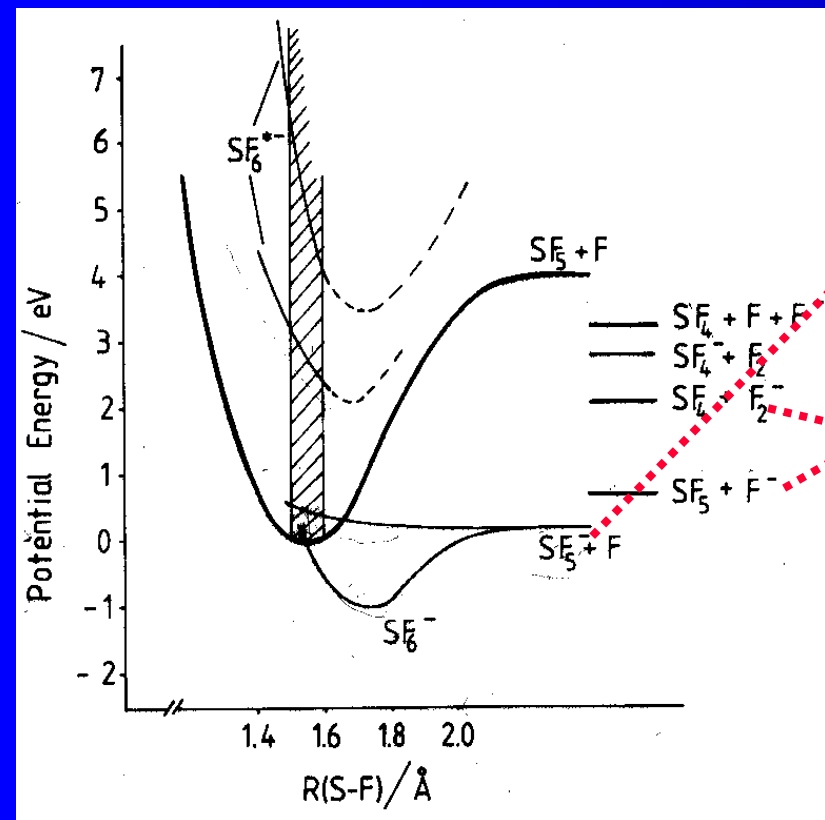
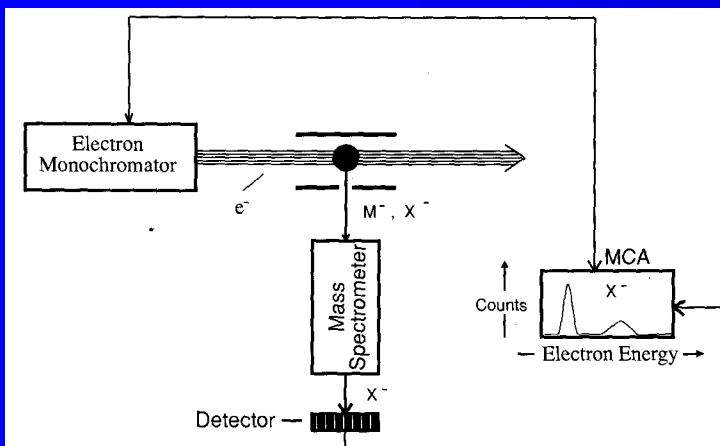


Fig. 2.2. Ion yield curve for SF_6^- formation and electron beam intensity monitored at collector A.

EA SF₆



EA SF₆ temperature dependence

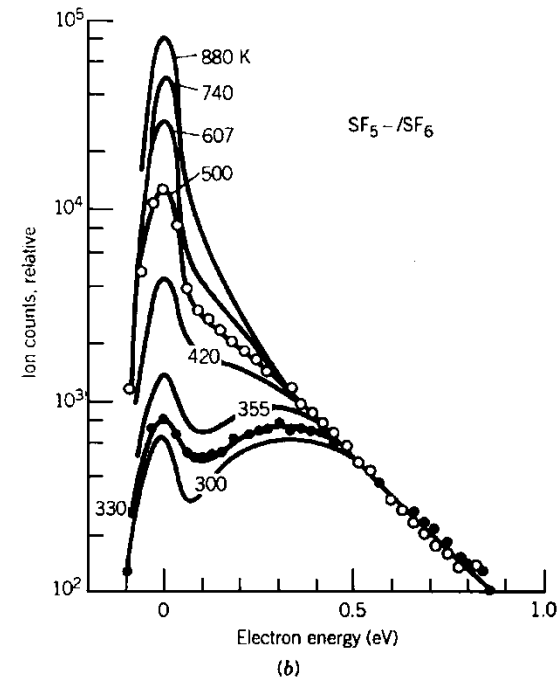
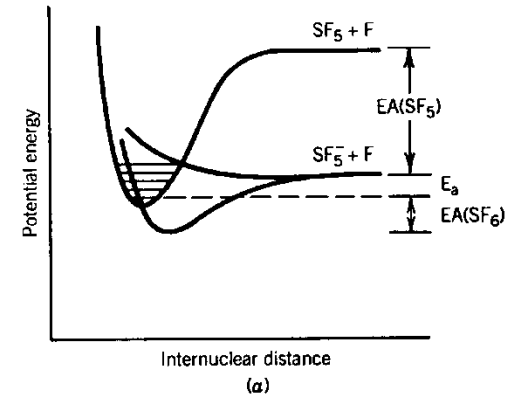


Figure 6-8-9. (a) Schematic potential energy curves for SF₆ and SF₅⁻. (b) Electron attachment to form SF₅⁻ from SF₆ versus electron energy, for various gas temperatures. [From Chen and Chantry (1979).]

Attachment NO to particular channel

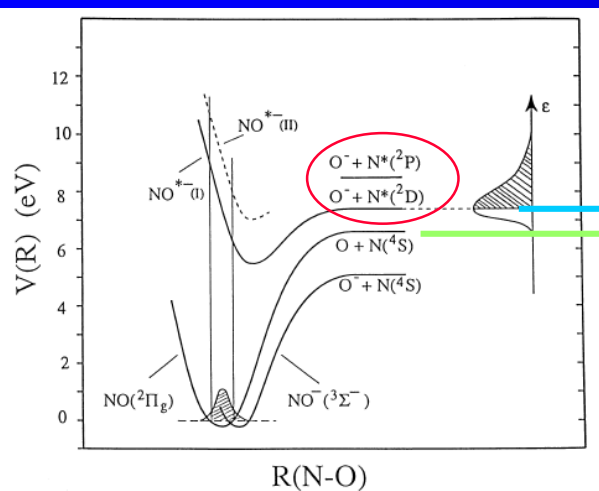


Fig. 5. Schematic potential energy curves for the ground states of NO and NO⁻ and two excited states of NO^{*-} after Ref. [8]. Also shown is the relative DA cross-section curve for the reaction NO + e → O⁻(²P) + N^{*}(²D) obtained by applying the reflection principle.

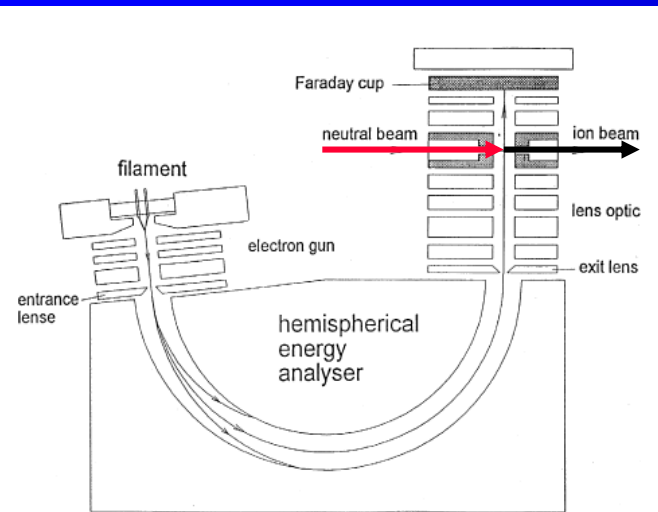
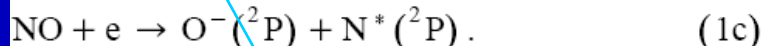
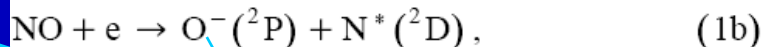
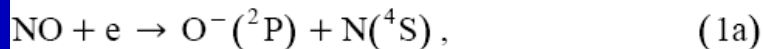


Fig. 1. Schematic diagram of the apparatus. Electrons are emitted from a hot filament, formed into a beam, pass the hemispherical energy selector at a constant energy of ~ 2 eV and are focused and brought to the final collision energy before they interact with the neutral beam and are collected at a Faraday cup.

Dissociative electron attachment to NO close to threshold may in principle proceed via the following channels:



The threshold energies of 5.074, 7.457 and 8.650 eV, respectively, can be derived using the bond dissociation energy $D(\text{N-O}) = 6.535$ eV [10], the electron affinity $\text{EA}(\text{O}) = 1.461$ eV [11] and the excitation energies $E(\text{N}^*({}^2\text{D})) = 2.383$ eV and $E(*\text{N}({}^2\text{P})) =$

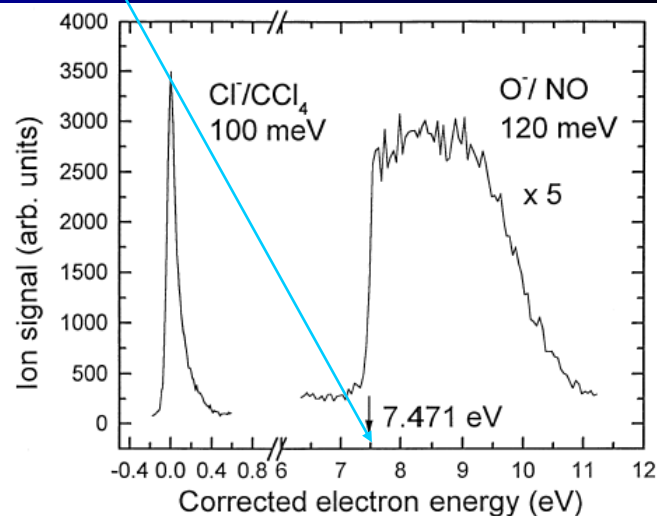
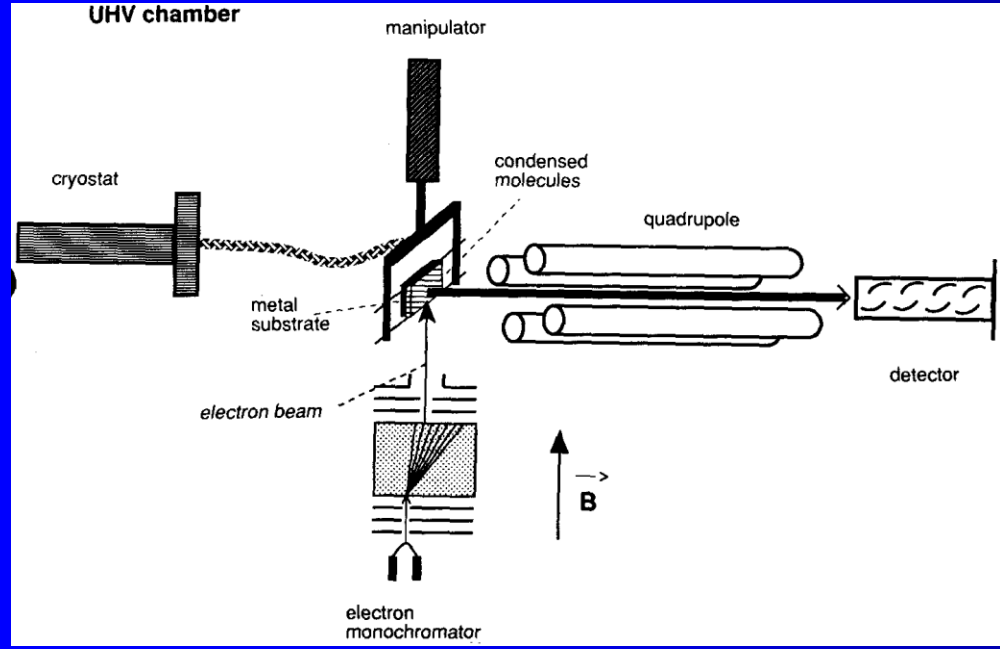
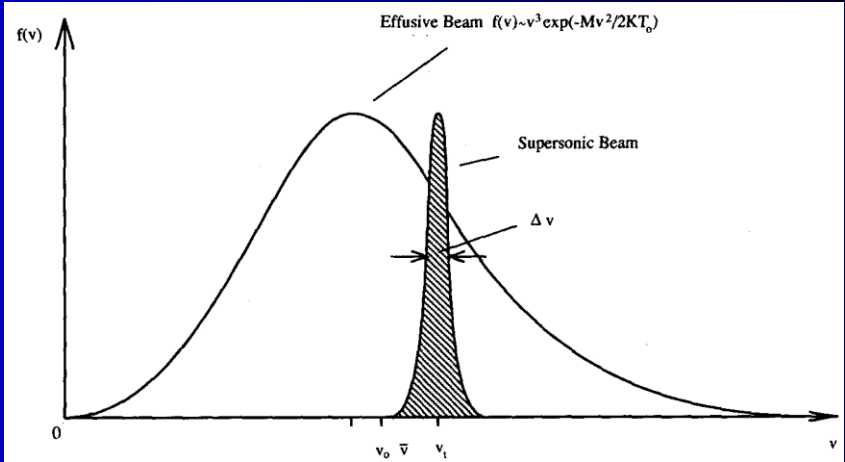
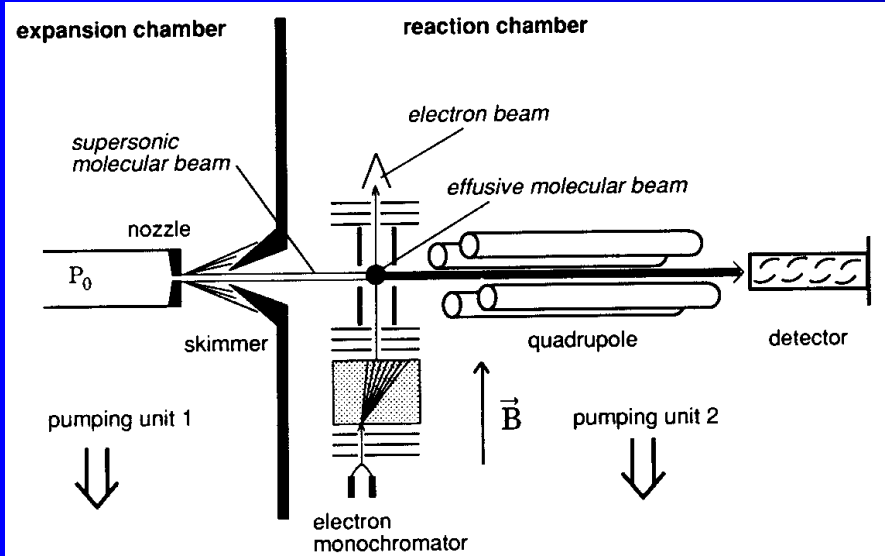


Fig. 4. Formation of O⁻ from NO by electron impact. The Cl⁻/CCl₄ cross-section curve is used to calibrate the electron energy scale and to determine the electron energy resolution (120 meV). The arrow points to the presently determined threshold energy of the reaction $\text{NO} + e \rightarrow \text{O}^-({}^2\text{P}) + \text{N}^*({}^2\text{P})$.

EA clusters and surface



Energy levels in clusters

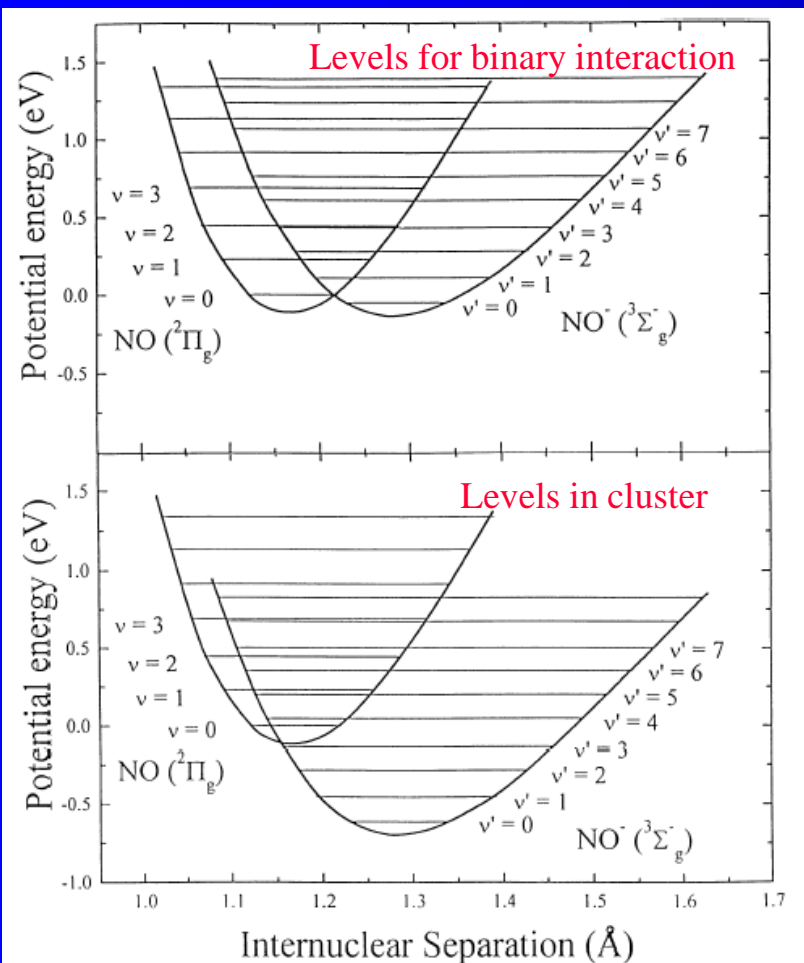


Fig. 3. Upper panel: approximate potential energy diagrams for NO and NO^- adapted from Ref. [5]. The $v=0$ level is located at 26 meV below the $v=0$ level of neutral NO. Lower panel: potential energy curves as above but shifted for the anion due to the polarization interaction of the negative charge with surrounding NO molecules. The NO^- curve is positioned (arbitrarily) so that the $v=4$ level is accessible by 40 meV electrons, in accordance with the experiment.

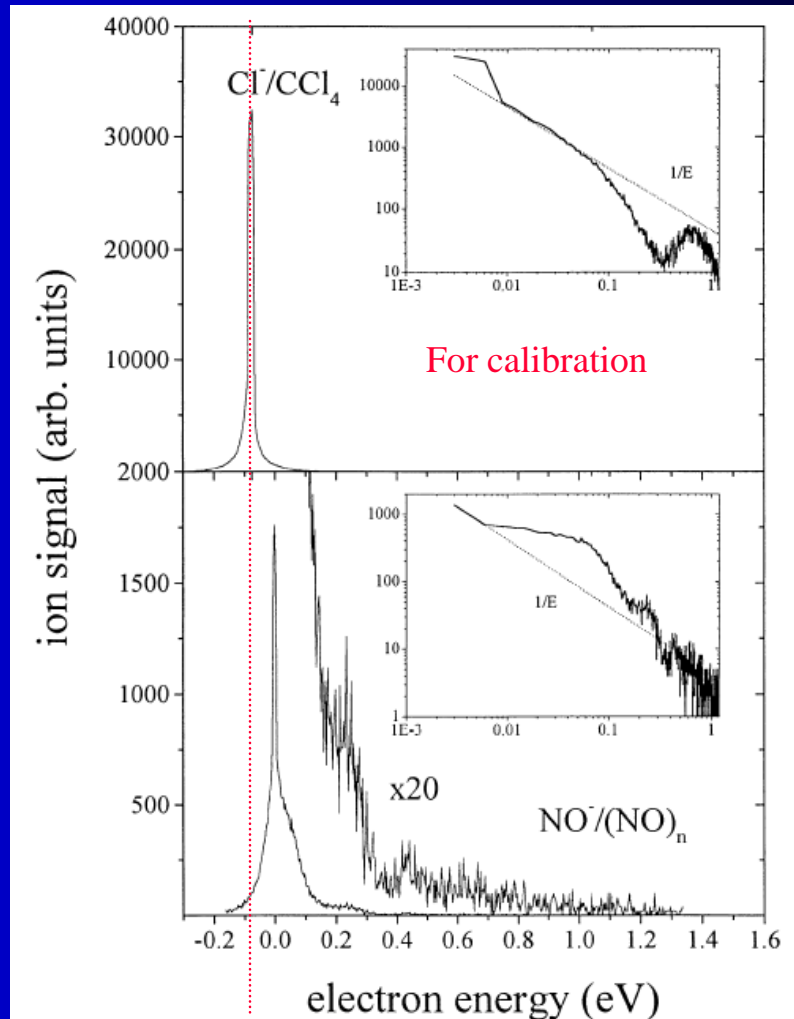


Fig. 1. NO^- signal observed from electron attachment to an NO cluster beam as a function of the electron energy. For comparison the energy calibration signal Cl^- from CCl_4 is also shown. Insets: count rate versus electron energy on a log-log scale. Dotted lines indicate the $1/E$ dependence predicted by s-wave scattering theory.

Negative ions, formation of negative clusters

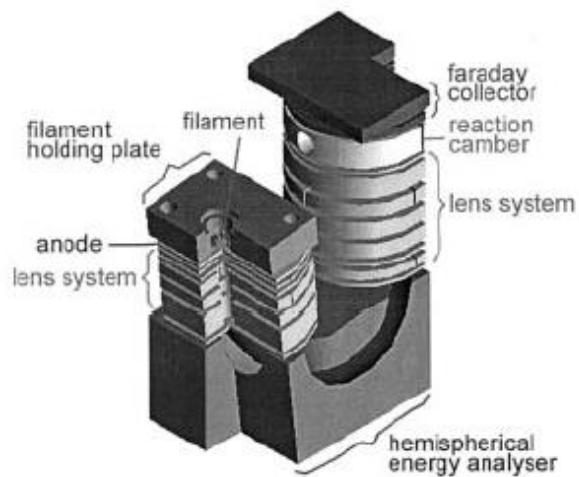
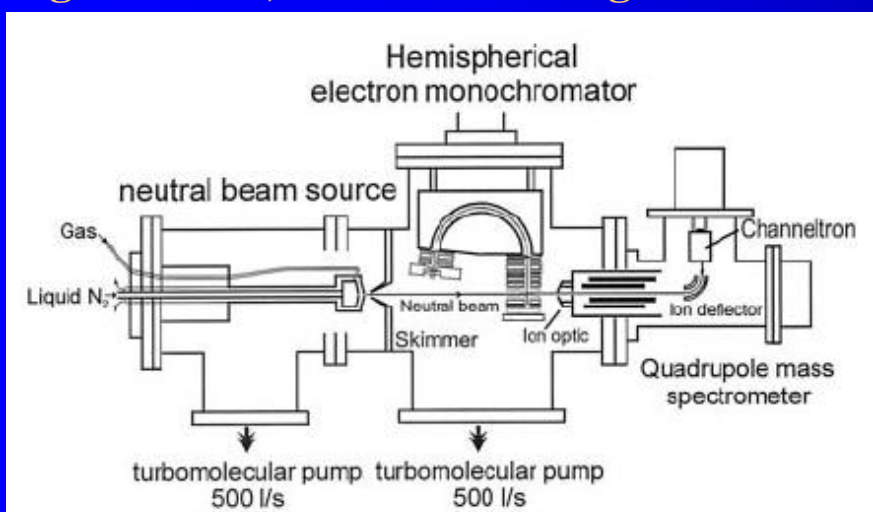


Fig. 1. Schematic diagram of the instrument. Electrons are emitted from a hot filament, and focused into a beam. They pass the hemispherical energy selector at a constant energy of about 4 eV and are focused and brought to the final collision energy before they interact with the neutral beam and are collected at a Faraday cup. Also shown is a close-up of the monochromator in a three dimensional view.

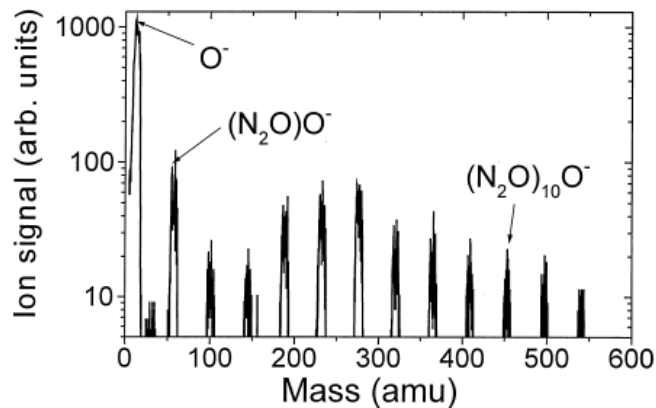


Fig. 2. Mass spectrum for $(N_2O)_nO^-$ cluster anions produced by electron attachment (using 2 eV electrons) to a N_2O cluster beam formed with the stagnation gas temperature at room temperature and the stagnation gas pressure of 3 bar.

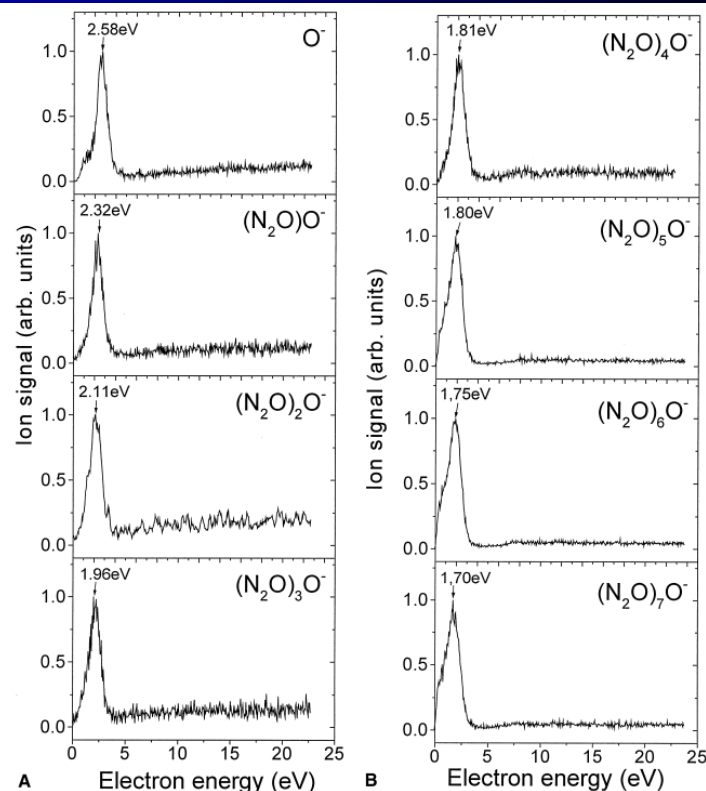


Fig. 6. Energy dependence of the $(N_2O)_nO^-$ yield for various cluster sizes (all curves are normalized to the same maximum value) for an extended range of electron energy (as compared to results shown in Fig. 4 which only cover the range up to 4 eV).

Rydberg atom attachment apparatus

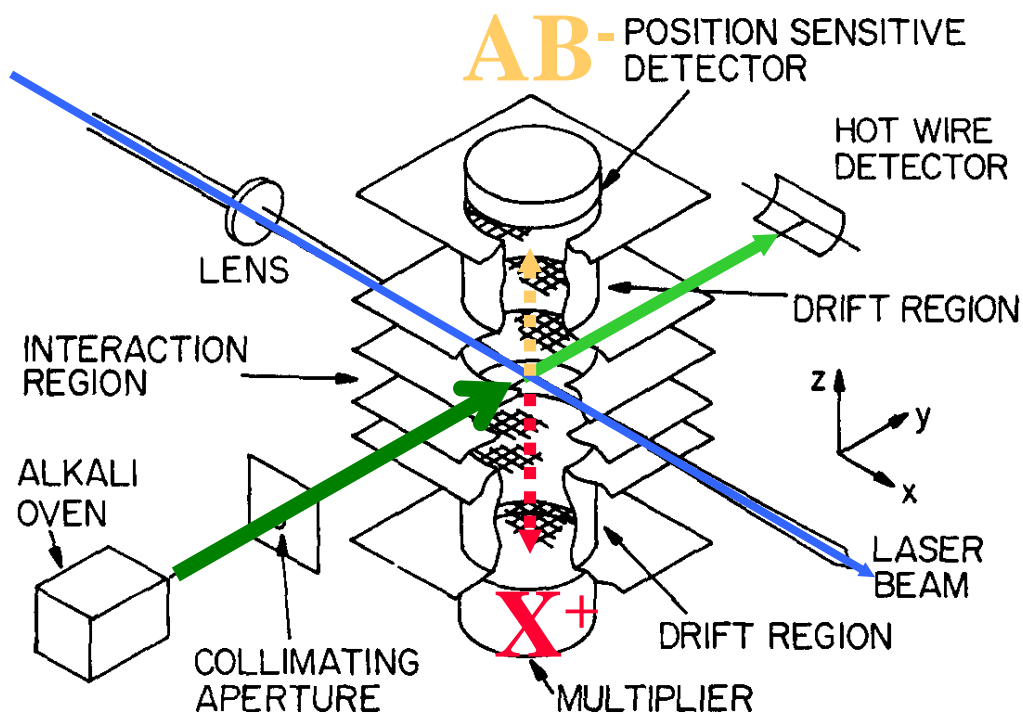


Figure 6-6-2. Dunning's Rydberg atom attachment apparatus. [From Dunning (1987).]

X^* are produced by laser excitation



X^+ and AB^- are detected by the pair of opposing detectors. Time-of-flight technique can be used to determine the mass of the negative ions. The density of Rydberg atoms in the interaction region can be determined by applying sufficiently strong electric field to ionize the atoms and then counting the ions thus formed.

Electron attachment from laser excited Rydberg atoms - Hotop

X^* are produced by laser excitation

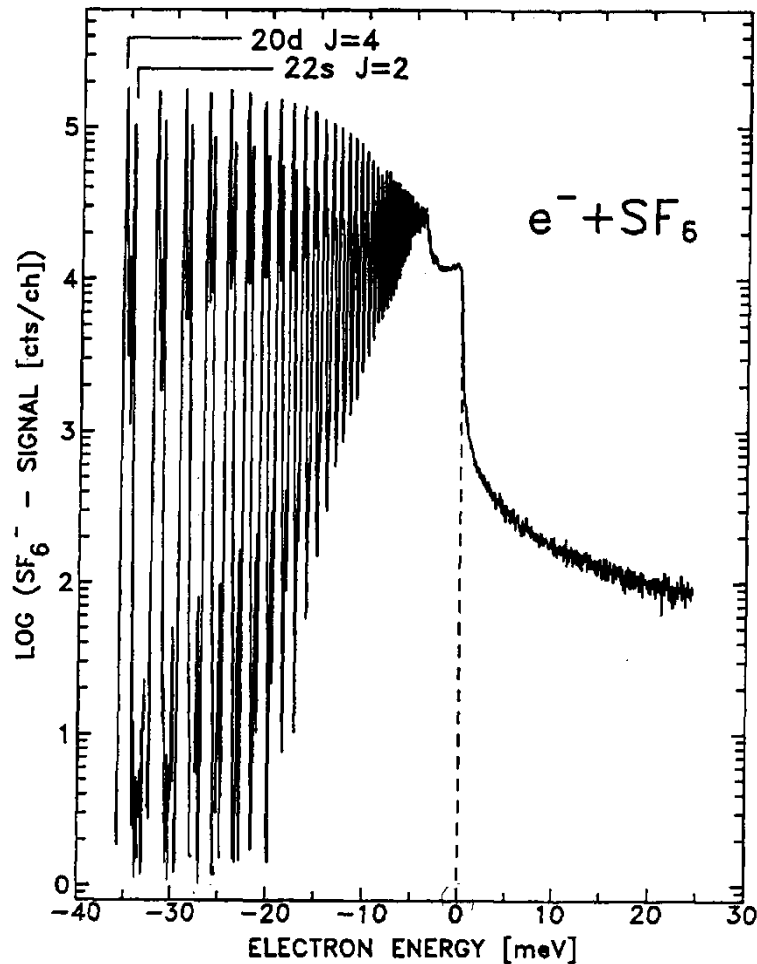


Figure 6-6-6. Results from Hotop's experiments on electron attachment from laser-excited Rydberg atoms and photodetached threshold electrons. [From Klar et al. (1991).]

Photodetachment of negative ions

Atomic Collisions – Heavy particle projectiles (1993)
 E.W.McDaniel, J.B.A.Mitchell, M.E.Rudd,

6-10. DETACHMENT PROCESSES

A. Photodetachment of Negative Ions

The detachment of electrons from negative ions by photon impact has been the subject of intensive investigation since the pioneering work of Branscomb and collaborators in the 1950s and 1960s (Branscomb, 1962). Recent reviews of progress in this area have been given by Miller (1981), Drzaic et al. (1984), Mead et al. (1984), and Ervin and Lineberger (1991). By measuring the location of photodetachment thresholds, it is possible to obtain extremely accurate values of electron affinities for atomic and some molecular negative ions, as discussed in Section 6-2. The high photon flux available from laser light sources has led to improvements in accuracy of many orders of magnitude for such measurements.

A typical apparatus used for photodetachment studies is that shown in Fig. 6-10-1. Negative ions are produced in a hot-cathode arc discharge or cold-

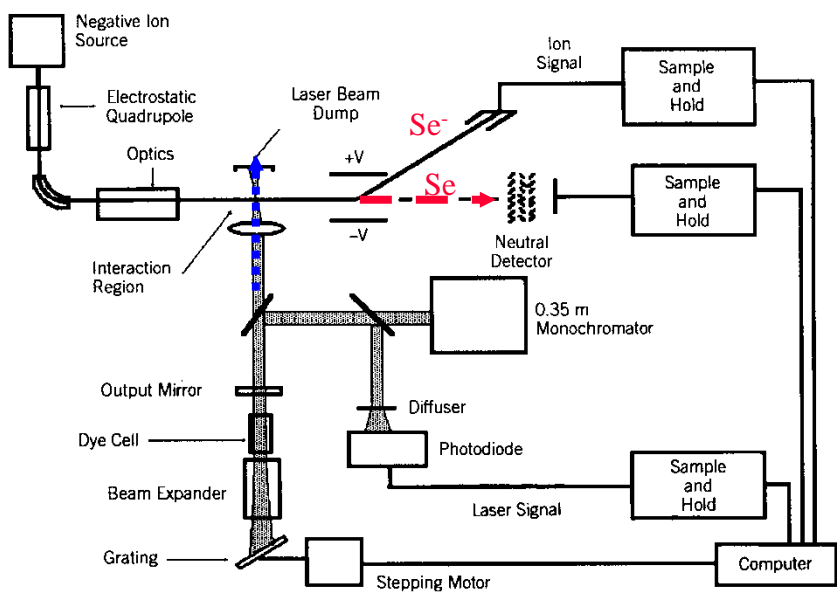


Figure 6-10-1. Apparatus used by Lineberger and Woodward (1970) for studying photodetachment with a tunable dye laser as a light source.

Threshold Studies

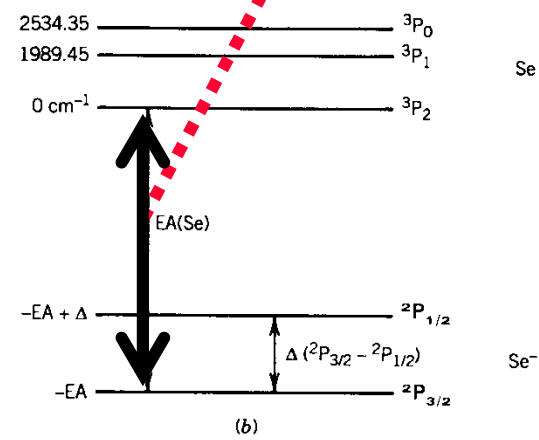
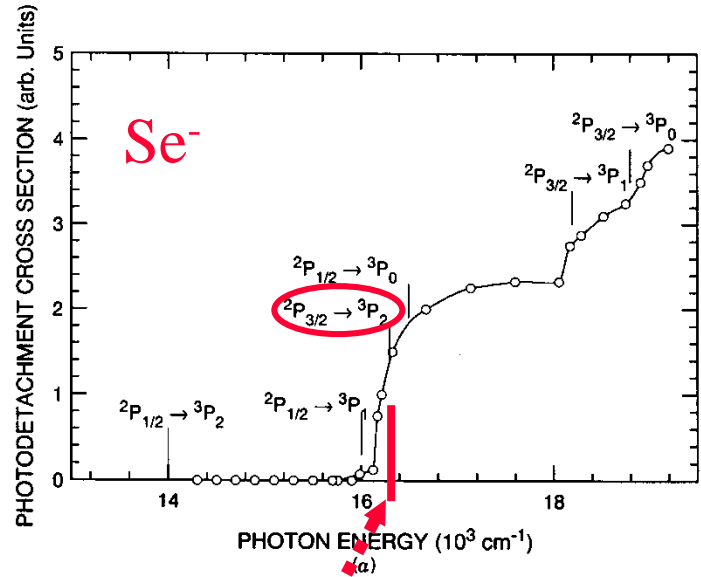


Figure 6-10-3. (a) Photodetachment cross sections for Se^- , measured with a tunable dye laser as a light source, by Lineberger and Woodward (1970) and by Hotop et al. (1973), respectively. (Not all measured data points are shown.) (b) Energy levels of Se and Se^- .

Cross section

Photodetachment $O^- + h\nu \rightarrow O + e$

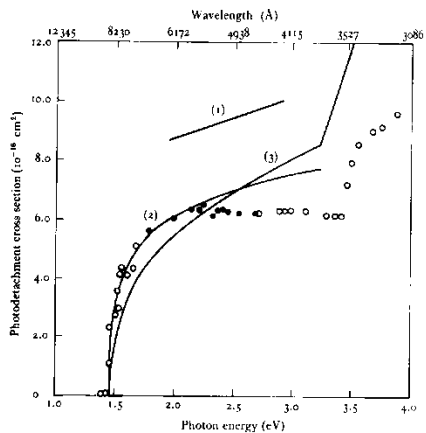


Fig. 11.15. Photodetachment cross-sections for O^- . ●, ○, observed by Branscomb *et al.* (1965), (1) derived from analysis of arc emission spectra by Boldt (1956) (see Chapter 8, p. 253), (2) calculated by Cooper and Martin (1962), (3) calculated by Robinson and Geltman (1967).

Electron affinity of O is 1.46eV

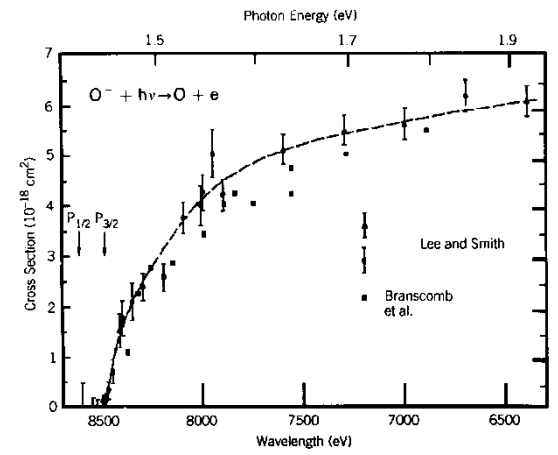


Figure 6-10-6. Photodetachment cross sections for O^- . [From Lee and Smith (1979).]

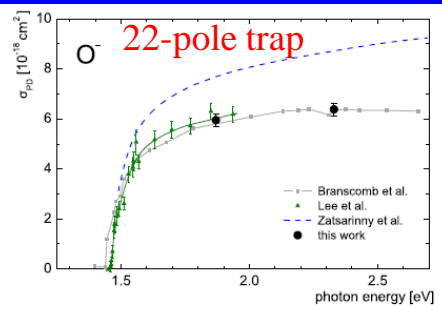


FIG. 2. (Color online) Measured cross section of O^- as a function of the photon energy. Our data (large full circles) is compared with the relative measurements of Refs. 13 and 25 (squares and small triangles), which were calibrated to hydrogen anion measurements. The dashed line shows the *ab initio* calculation of Ref. 15.

Photodetachment $OH^- + h\nu \rightarrow OH + e$

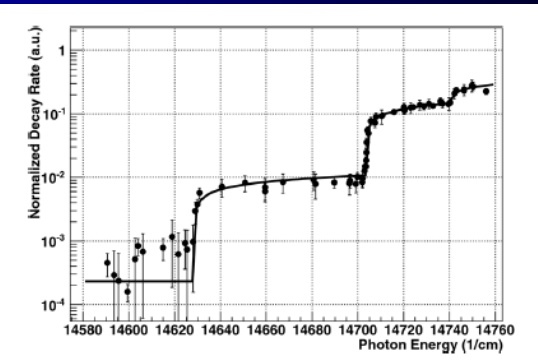
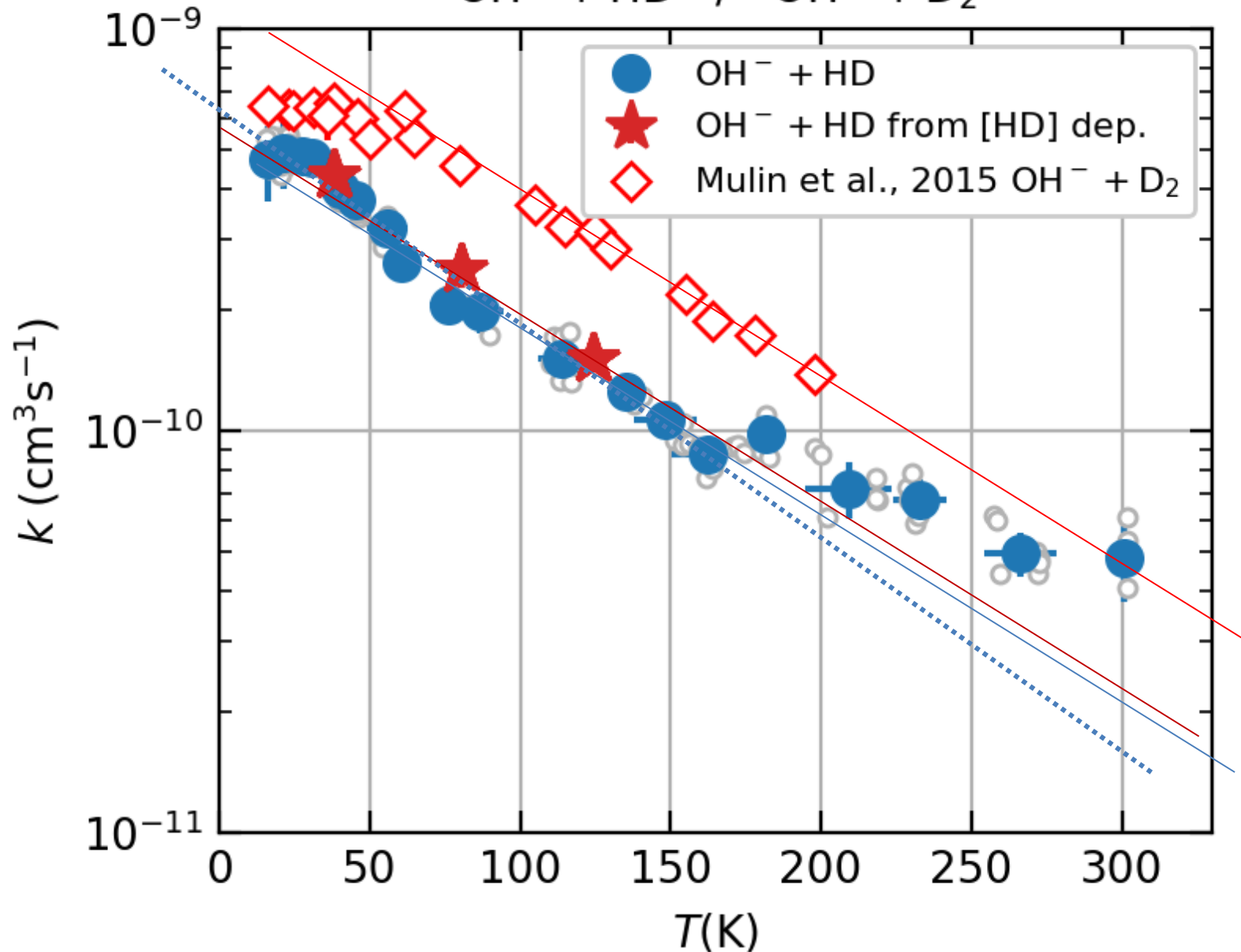


Fig. 3 Photodetachment cross section of OH^- at a trap temperature of 50 K for varying photon energy. The steps in the cross section are due to the opening of loss channels corresponding to the $J = 2, 1$ and 0 rotational states of the anion.

$\text{OH}^- + \text{HD} / \text{OH}^- + \text{D}_2$



na tomto obrázku data od Mulin 2015 byla korigovaná na $T_{22\text{PT}}+5$ K! Teploty pro data od Mulin 2015 jsou přepočtené na srážkové teploty $T = T_{22\text{PT}}+5$ K.

Photodetachment $O^- + h\nu \rightarrow O + e$

Photodetachment $OH^- + h\nu \rightarrow OH + e$

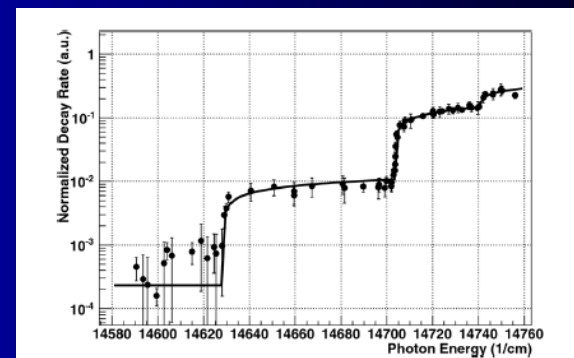


Fig. 3 Photodetachment cross section of OH^- at a trap temperature of 50 K for varying photon energy. The steps in the cross section are due to the opening of loss channels corresponding to the $J = 2, 1$ and 0 rotational states of the anion.

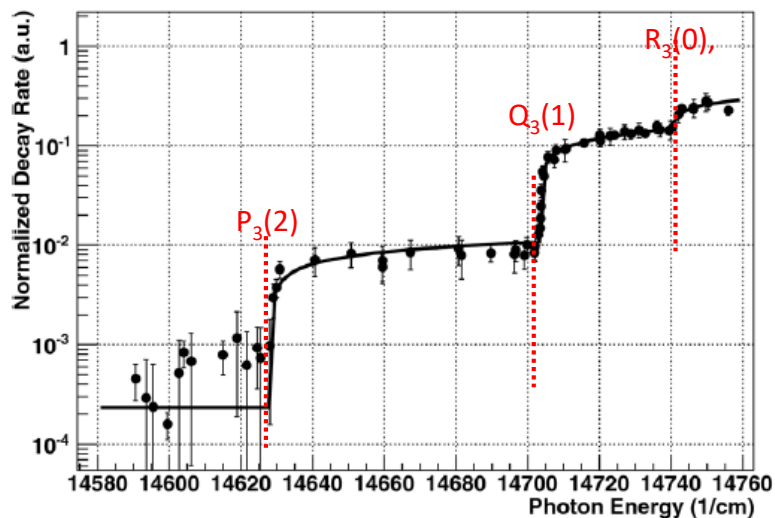
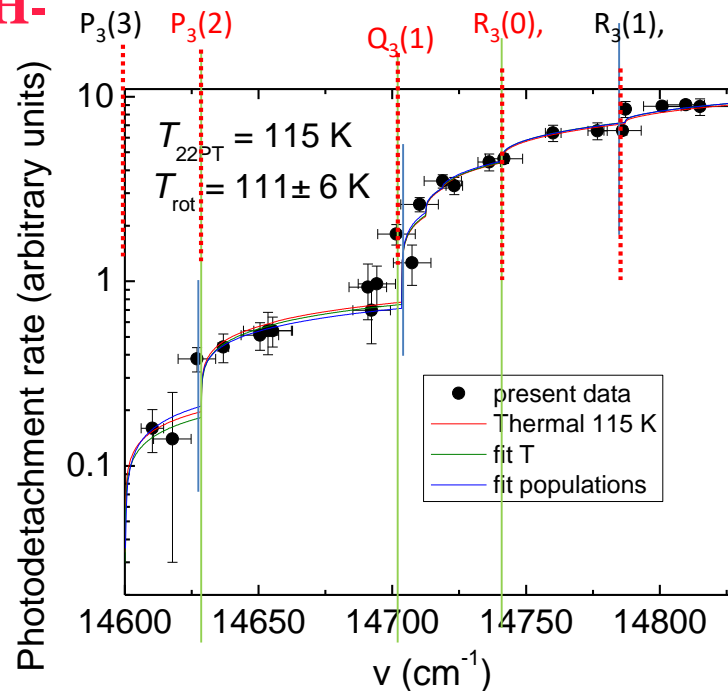


Fig. 3 Photodetachment cross section of OH^- at a trap temperature of 50 K for varying photon energy. The steps in the cross section are due to the opening of loss channels corresponding to the $J = 2, 1$ and 0 rotational states of the anion.

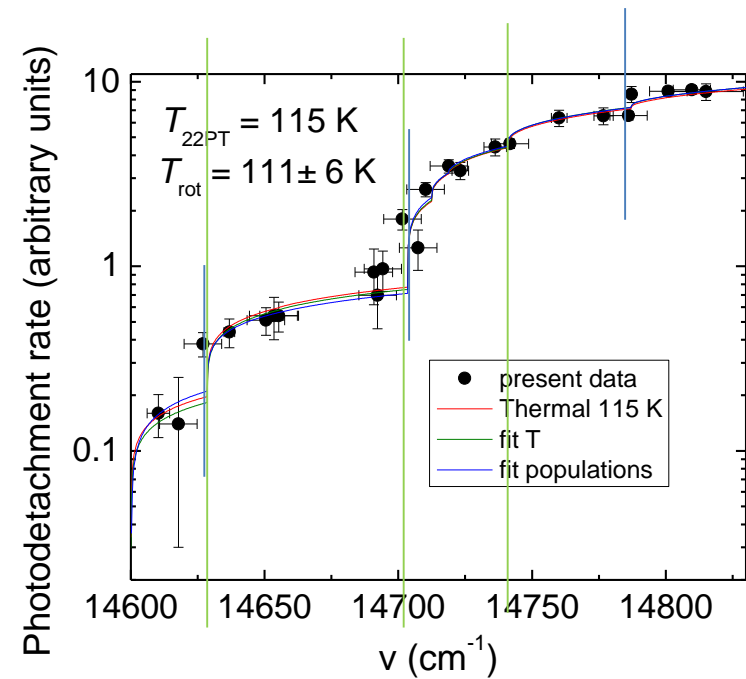
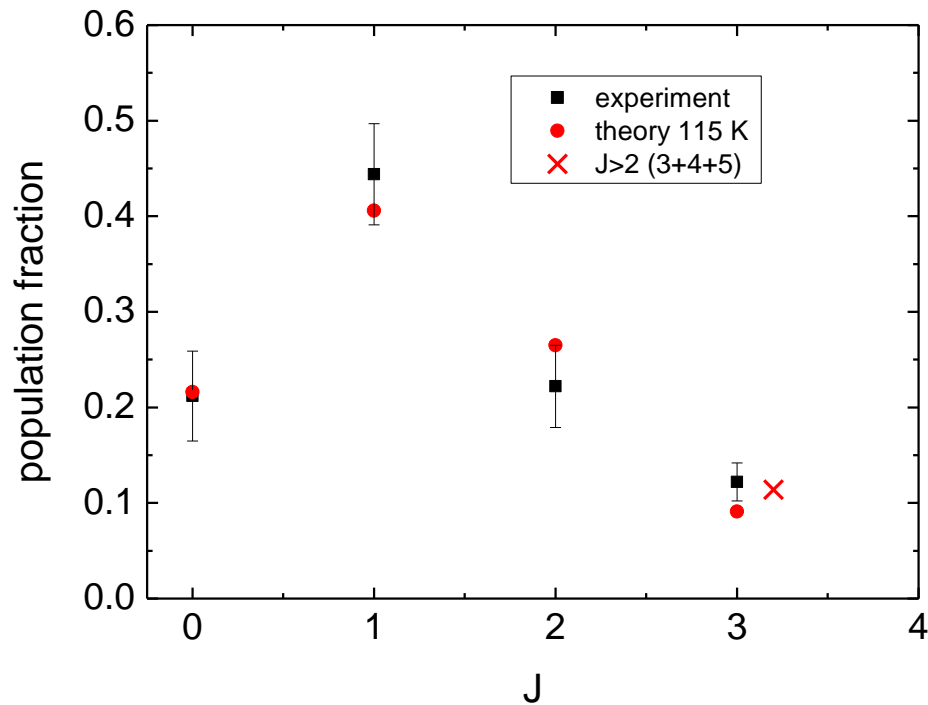
OH-



$R_3(0)$, $Q_3(1)$ and $P_3(2)$

transitions	threshold energies ϵ_i (cm^{-1})	transitions	threshold energies ϵ_i (cm^{-1})
$O_3(4)$	14450.8	$P_1(3)$	14703.6
$O_3(3)$	14516.4	$Q_3(2)$	14712.5
$P_3(4)$	14569.1	$Q_3(3)$	14718.8
$P_3(3)$	14600.2	$Q_3(4)$	14723.0
$P_3(2)$	14628.6	$R_3(0)$	14740.9
$P_1(4)$	14655.7	$R_3(1)$	14787.2
$Q_3(1)$	14703.5	$Q_1(4)$	14796.1

Table 1. The list of transitions and corresponding threshold energies used in present study. Note that only the transitions $R_3(0)$, $Q_3(1)$ and $P_3(2)$ were considered in the study by Otto et al. (2013).



transitions	threshold energies ϵ_i (cm ⁻¹)	transitions	threshold energies ϵ_i (cm ⁻¹)
O ₃ (4)	14450.8	P ₁ (3)	14703.6
O ₃ (3)	14516.4	Q ₃ (2)	14712.5
P ₃ (4)	14569.1	Q ₃ (3)	14718.8
P ₃ (3)	14600.2	Q ₃ (4)	14723.0
P ₃ (2)	14628.6	R ₃ (0)	14740.9
P ₁ (4)	14655.7	R ₃ (1)	14787.2
Q ₃ (1)	14703.5	Q ₁ (4)	14796.1

Fig 2. Experimentally determined relative populations of the lowest rotational states of OH⁻ anion (squares) compared to calculated thermal populations at 116 K (circles). Due to the position of the corresponding photodetachment thresholds, the value obtained for J = 3 consists from indistinguishable contributions from states with J = 3, 4 and 5. Sum of the calculated relative thermal populations of these states is denoted by cross.

OH⁻

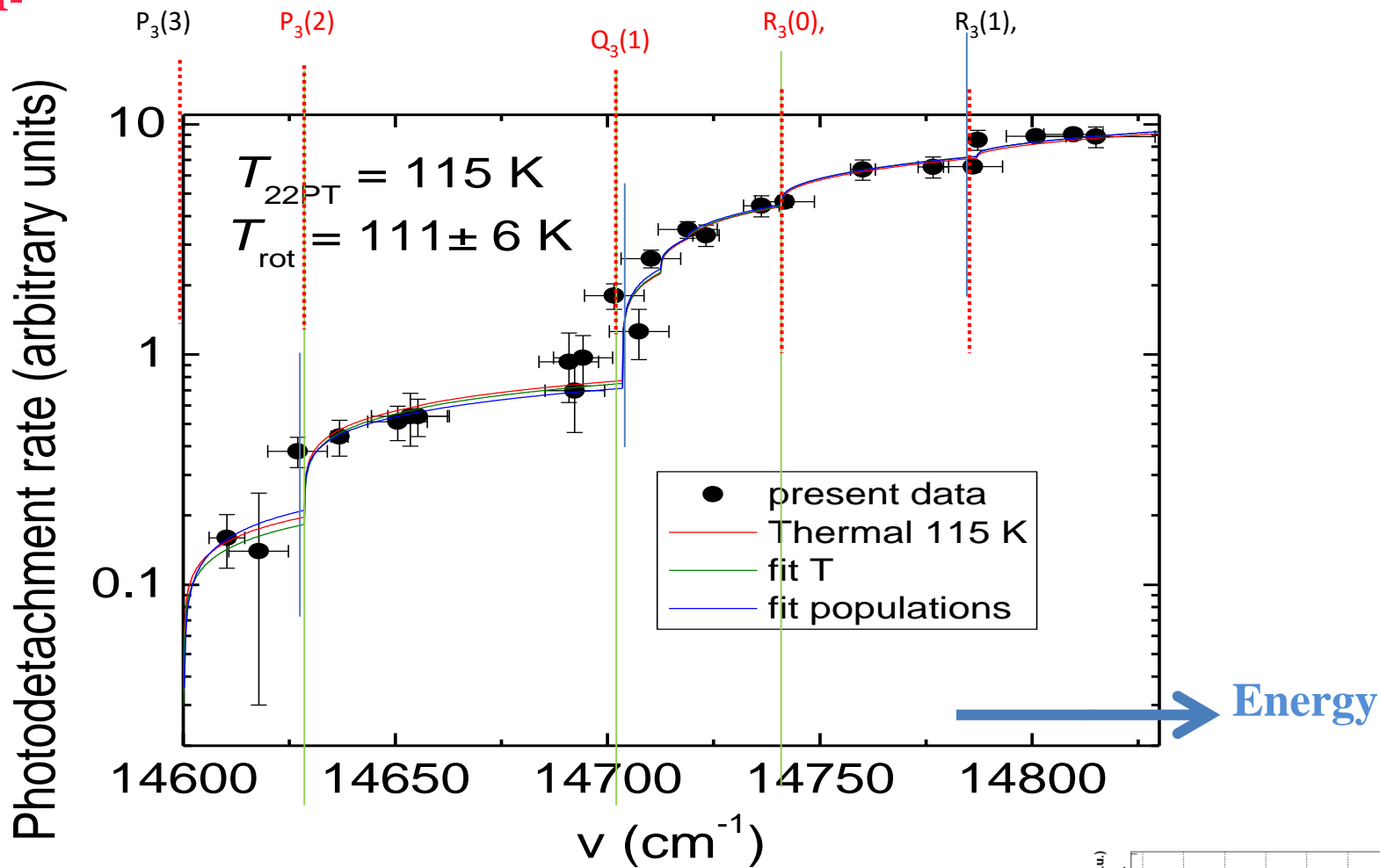


Fig 1. Photodetachment rate at trap temperature of 115 K. The obtained rotational temperature is $T_{\text{rot}} = 111 \pm 6 \text{ K}$. Red line is the expected photodetachment cross section at 115 K under assumption of thermal population of OH⁻ rotational states. Green line denotes fit of the data by equation (1) under assumption of thermal population of states with temperature as a free parameter and the blue line denotes fit of the obtained data by equation (1) with the populations of rotational states up to $J=3$ as free parameters.

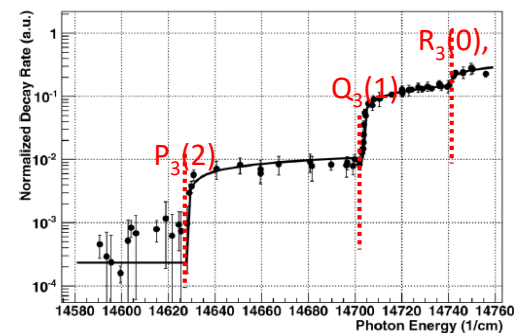


Fig. 3 Photodetachment cross section of OH⁻ at a trap temperature of 50 K for varying photon energy. The steps in the cross section are due to the opening of loss channels corresponding to the $J = 2, 1$ and 0 rotational states of the anion.

Cross sections comparison

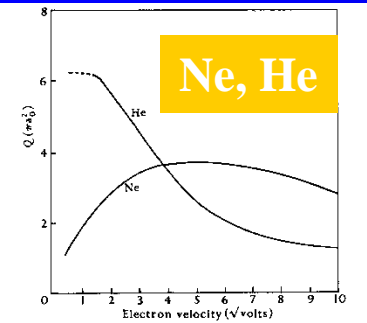


Fig. 1.10. Observed total collision cross-sections of He and Ne.

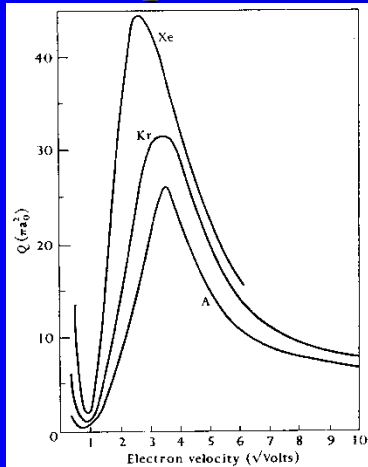


Fig. 1.9. Observed total collision cross-sections of A, Kr, and Xe.

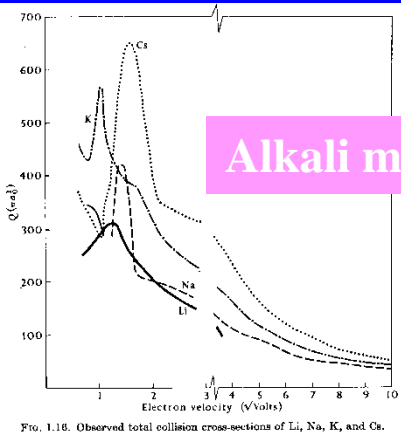
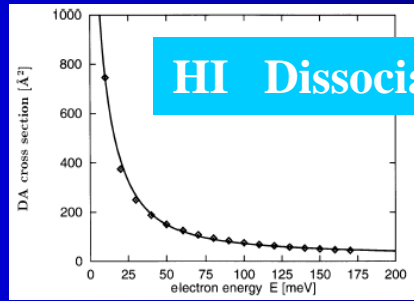


Fig. 1.18. Observed total collision cross-sections of Li, Na, K, and Cs.



HI Dissociative attachment

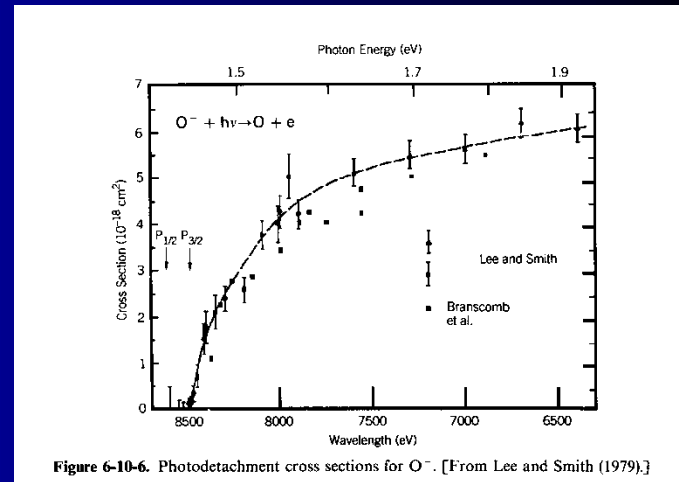


Figure 6-10-6. Photodetachment cross sections for O^- . [From Lee and Smith (1979).]

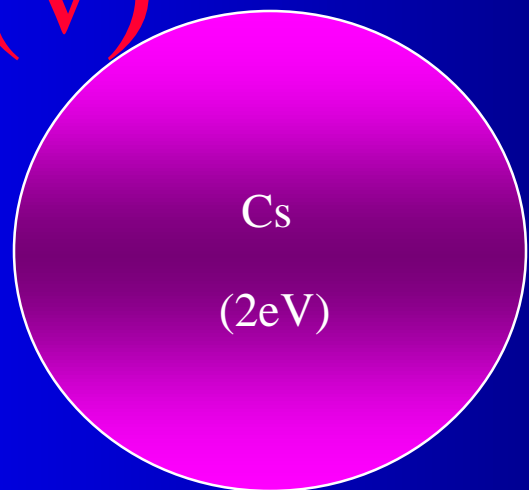
Alkali metals

$\sigma(v)$

Ar
(3eV)

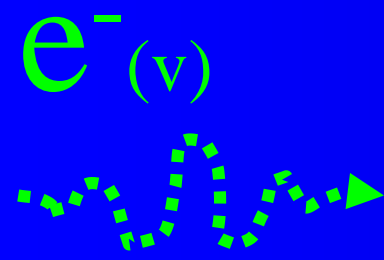
Ne

Ar
(0.3eV)



Attachment
HI

Photodetachment $\times 10^{-2}$



Photodetachment $H^- + h\nu \rightarrow H(n) + e$

Cross section

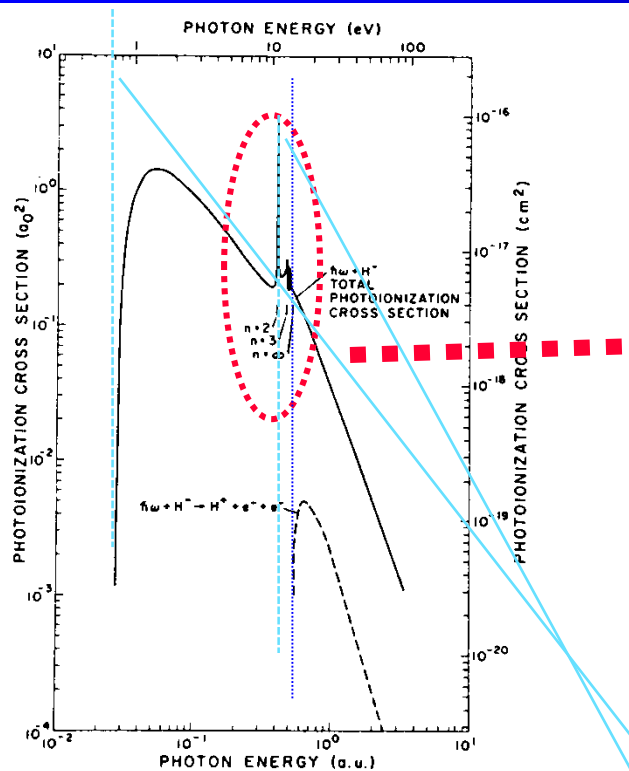


Figure 6-10-7. Theoretical photodetachment cross sections for H^- . [From Broad and Reinhardt (1976).]

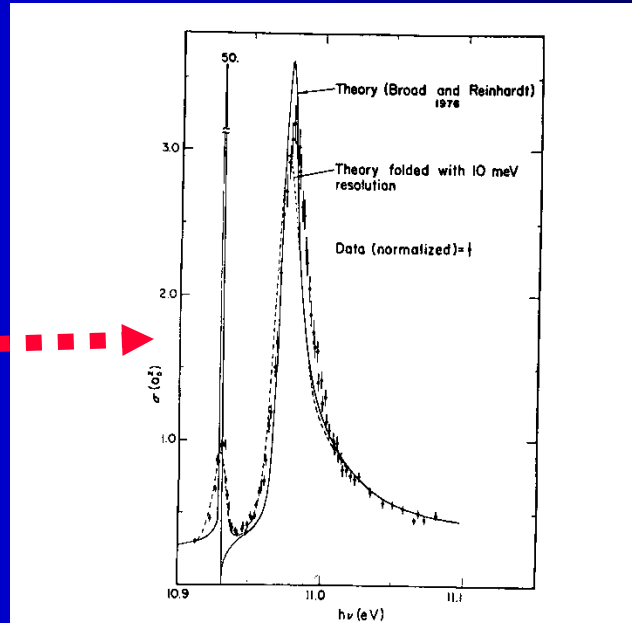
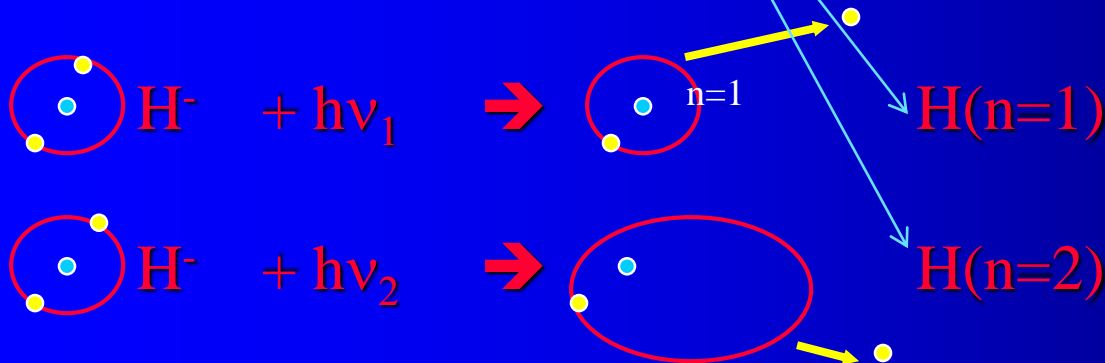
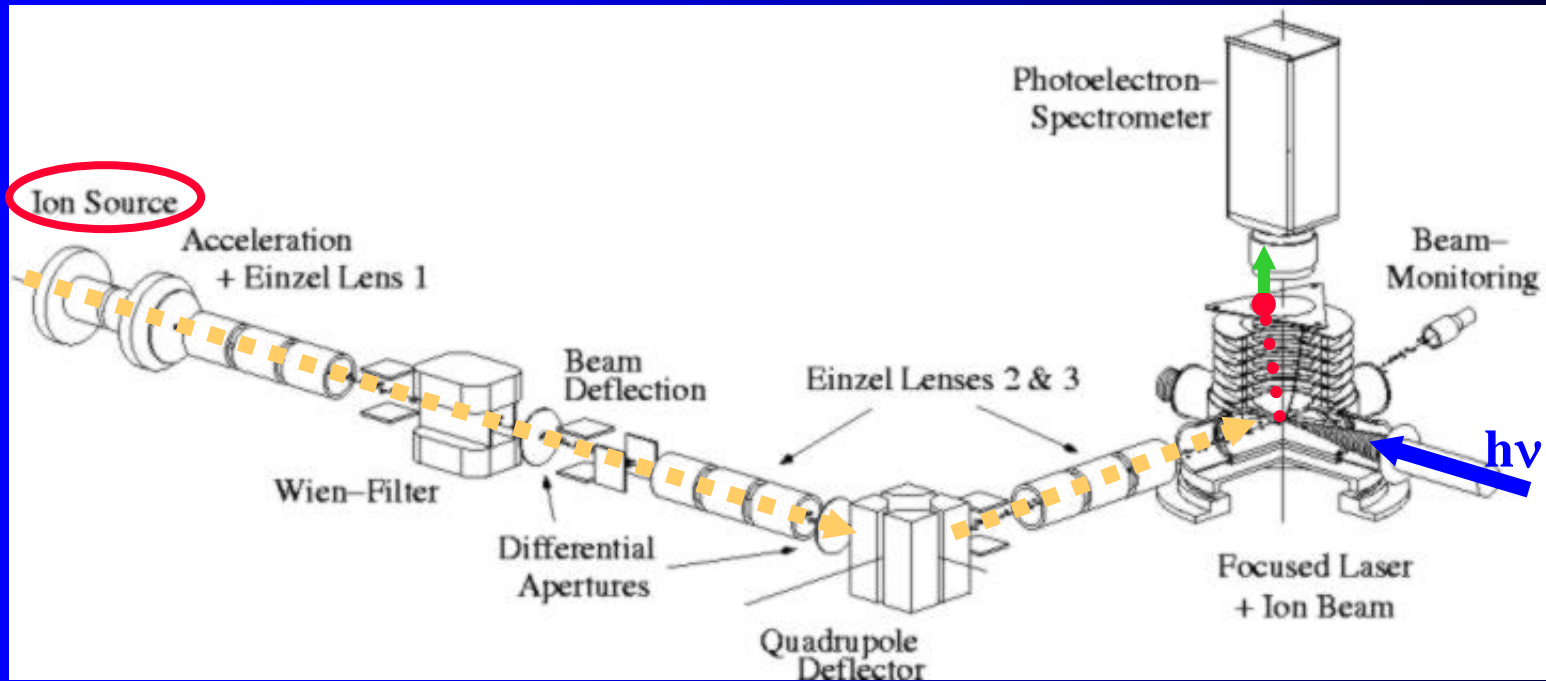


Figure 6-10-8. Comparison of calculated photodetachment cross section for H^- (Broad and Reinhardt, 1976) with experimental results measured using the LAMPF accelerator. [From Gram et al. (1978).]



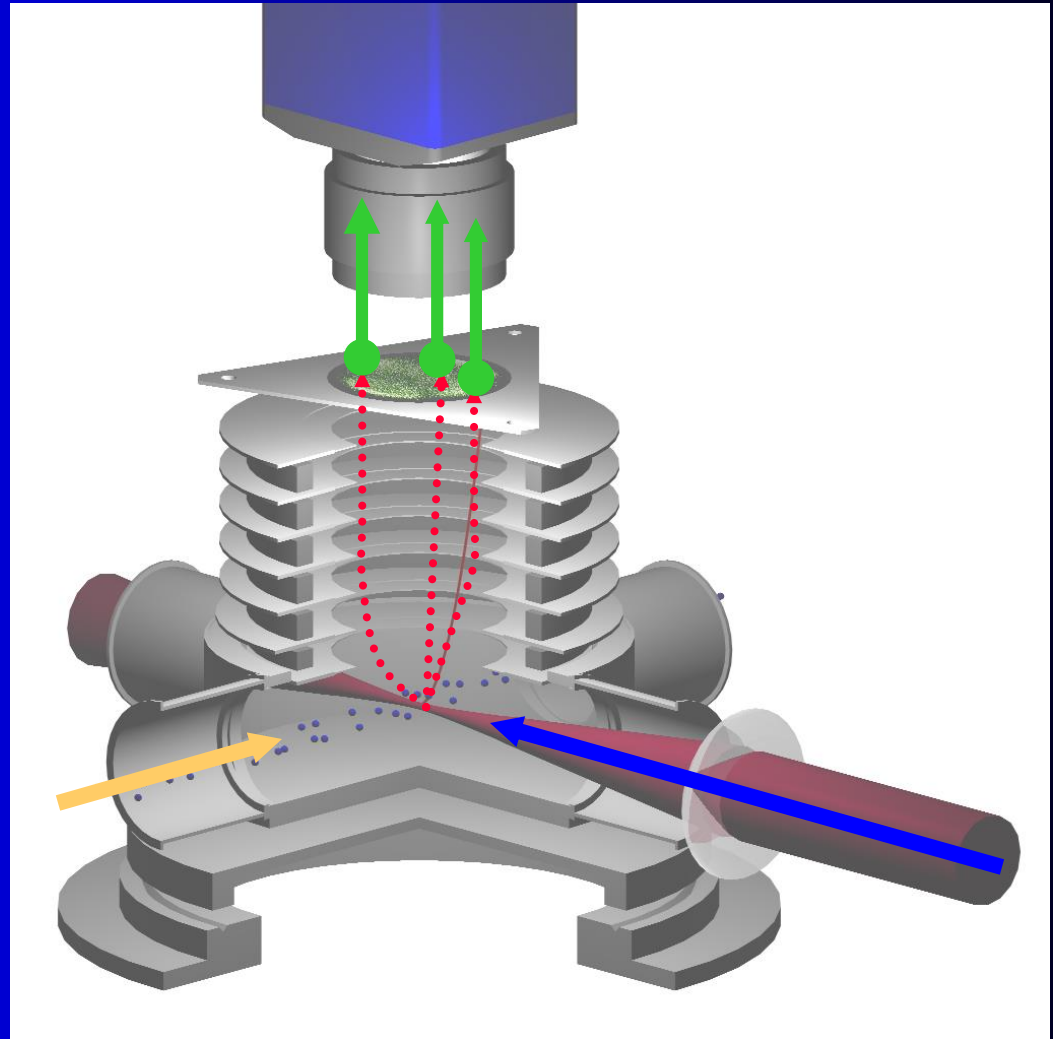
Hanspeter Helm - Photoelectron spectrometer - Experimental setup



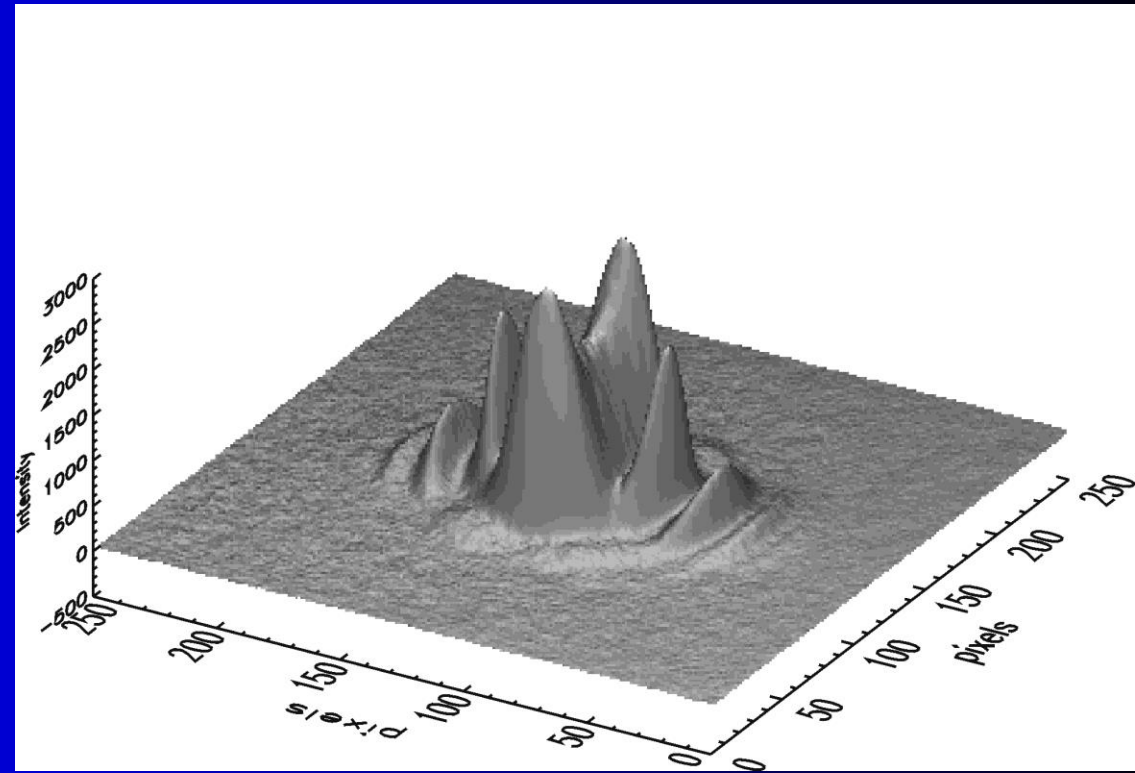
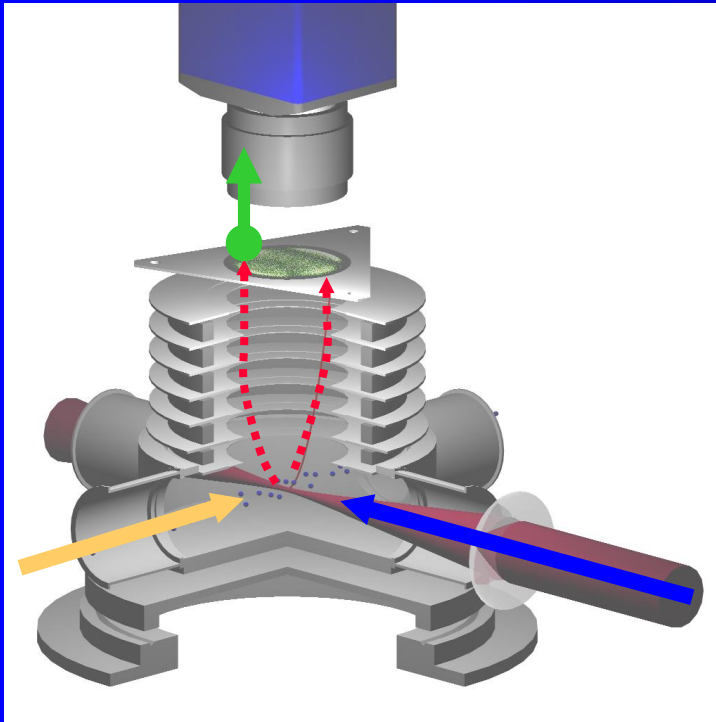
Schematic view of the fast negative ion beam imaging spectrometer. A fast beam of negative hydrogen ions is formed in a hollow cathode discharge ion source, and shaped by an einzel lens 1. The einzel lens 1 collimates the 3 keV beam for optimal passage through the Wien-Filter. The settings of the Wien-Filter also prohibit the passage of electrons co-propagating in the beam into subsequent vacuum chambers. The einzel lenses 2 and 3 serve as an electrostatic telescope to control the collimation and convergence properties of the beam in the interaction chamber. **The H- flux corresponds to a current of 100 nA** and arrives at the center of the photoelectron spectrometer with a beam waist of 400 μm . The 90 degree beam bend in the quadrupole deflector removes neutral hydrogen atoms from the beam. These are produced by collisional detachment with residual gas atoms in the first two vacuum sections where a higher residual pressure prevails. The three vacuum sections are differentially pumped to maintain a residual pressure of $5 \cdot 10^{-10}$ mbar in the third section during operation. Intense laser pulses of an energy of 56 μJ , a pulse length of 250 fs and a wavelength of 2.15 μm cross the ion beam under 90 degrees and interact with atomic particles at a repetition rate of 1 kHz. We use a standard Ti:Sapphire laser system with a regenerative amplifier and an optical parametric amplifier (OPA). The outgoing pulses are linearly polarized along the ion beam propagation axis and focused at the center of the ion beam. The heart of our setup is an imaging spectrometer that was first introduced by Helm *et al*, see following box.

Hanspeter Helm Photoelectron spectrometer

The principle of our Photoelectron spectrometer is shown on the right. Electrons produced in the interaction volume by laser irradiation of atoms, ejected in a solid angle of 4π are mapped onto a 2D position sensitive detector. The projection is achieved by homogeneous or weakly inhomogeneous electrical fields of 80 V/cm^2 in the inner spectrometer region. The detector consists of a Chevron stack of 2 inch diameter high-quality Multi-Channel Plates (MCPs) and a phosphor screen coated by a transparent, conducting gold layer. The amplified signal of an electron impact is drawn onto the phosphor screen by a potential of 2 keV to enhance in phosphorescence yield. This finite-sized light spots are accumulated and integrated by a 12 bit charge-coupled-device (CCD) camera and the data are taken by a frame grabber. The total electron yield is 10^7 - 10^8 spatially resolved electrons per hour acquisition time. Conventional photoelectron spectroscopy usually requires higher repetition laser systems in order to achieve similar statistics.



Hanspeter Helm 3D



Projection of a continuous 3D electronic wavefunction in momentum space onto a 2D imaging detector. It consists of a mixture of different partial waves and discrete energies. Their energetic spacing corresponds to the photon energy of the laser (EPD Excess Photon Detachment). The modulus of the 3D wavefunction can be reconstructed using numerical inversion routines, since dipole transitions possess an intrinsic cylindrical symmetry.

Absolute photodetachment cross section measurements of the O⁻ and OH⁻ anionP. Hlavenka, R. Otto, S. Trippel, J. Mikosch,^{a)} M. Weidemüller,^{b)} and R. Wester^{c)}

Absolute total photodetachment cross sections of O⁻ and OH⁻ anions stored in a multipole radio frequency trap have been measured using a novel laser depletion tomography method. For OH⁻ the total cross sections of $8.5(1)_{\text{stat}}(3)_{\text{sys}}$ and $8.1(1)_{\text{stat}}(7)_{\text{sys}} \times 10^{-18}$ cm², measured at 662 and 632 nm, respectively, were found constant in the temperature range of 8–300 K. The O⁻ cross sections $5.9(1)_{\text{stat}}(2)_{\text{sys}}$ and $6.3(1)_{\text{stat}}(2)_{\text{sys}} \times 10^{-18}$ cm² measured at 170 K at 662 and 532 nm, respectively, agree within error estimations with preceding experiments and increase the accuracy of the widely used calibration standard for relative photodetachment measurements of diverse atomic and molecular species. © 2009 American Institute of Physics. [DOI: 10.1063/1.3080809]

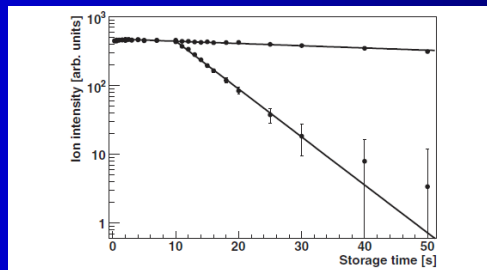


FIG. 2. Measured OH⁻ ion signal as a function of storage time in the trap. The upper set of points shows the signal in the absence of the photodetachment laser. The lower points show that, when the laser is switched on at 10 s, a fast additional loss channel due to photodetachment appears. The decay rates are obtained from exponential fits (solid lines).

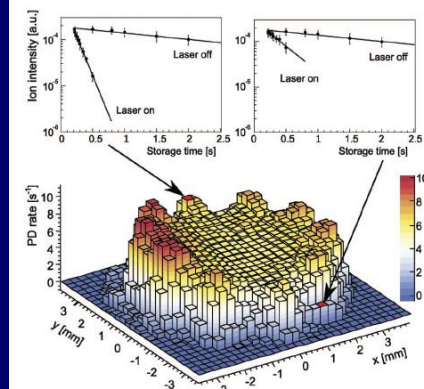


FIG. 1. (Color) Histogram of the measured photodetachment rate for O⁻ as a function of the transverse position of the laser light in the ion trap. The graph reflects the ion density distribution in the 22-pole trap, as the ion column density is proportional to the detachment rate. The insets show two examples for individual loss rate measurements.

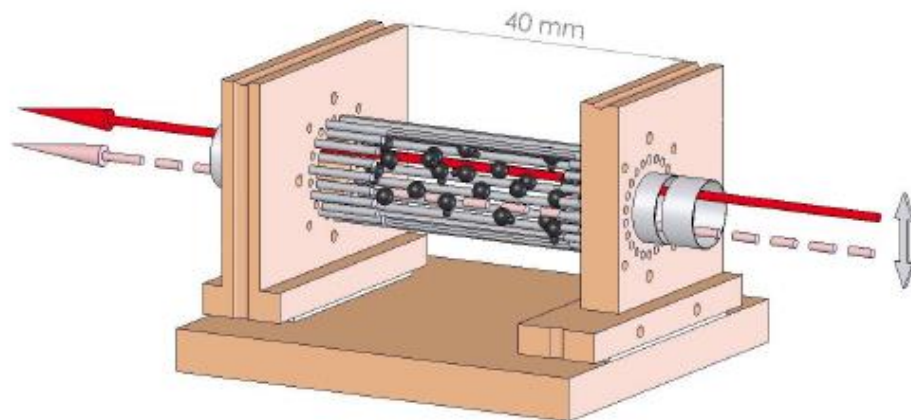


FIG. 1 (color online). Schematic view of the 22-pole ion trap with the rf electrodes for radial and the cylindrical dc end-cap electrodes for axial confinement. The position of the photodetachment laser is scanned along the vertical axis.

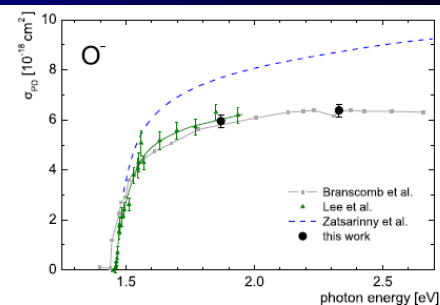


FIG. 2. (Color online) Measured cross section of O⁻ as a function of the photon energy. Our data (large full circles) is compared with the relative measurements of Refs. 13 and 25 (squares and small triangles), which were calibrated to hydrogen anion measurements. The dashed line shows the *ab initio* calculation of Ref. 15.

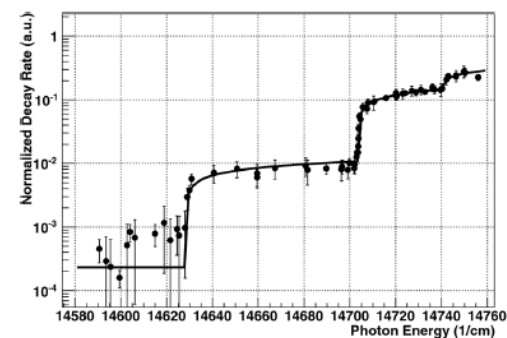
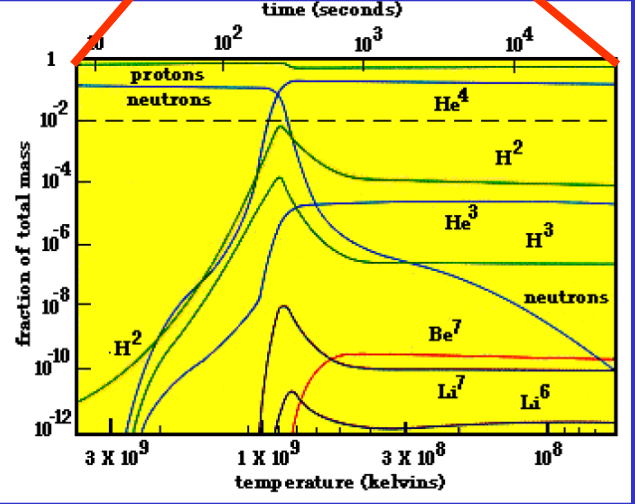
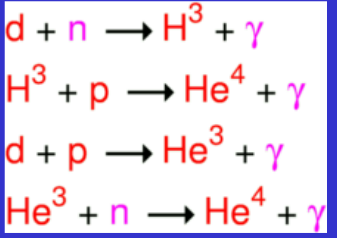
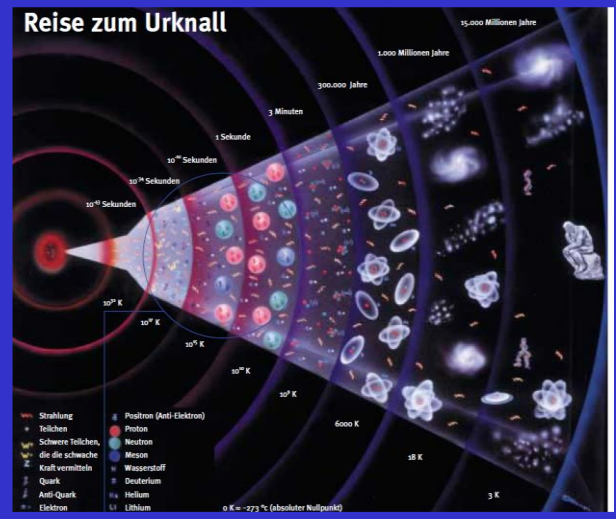
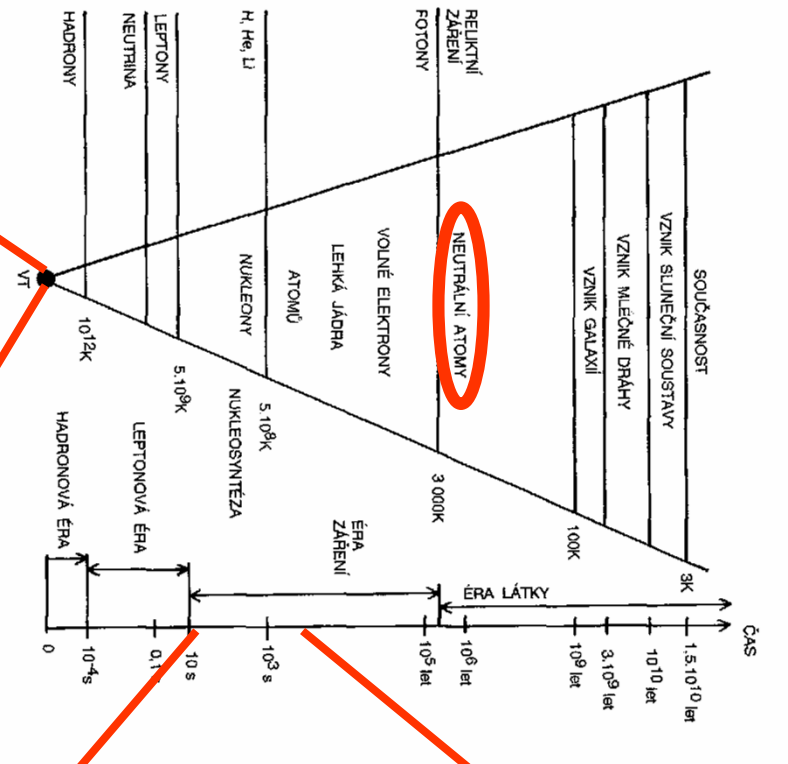


FIG. 3 Photodetachment cross section of OH⁻ at a trap temperature of 50 K for varying photon energy. The steps in the cross section are due to the opening of loss channels corresponding to the $J = 2, 1$ and 0 rotational states of the anion.

Starting with simple ...

$e^-, H^+, H, H^-, H_2^+, H_2, \dots H_3^+$

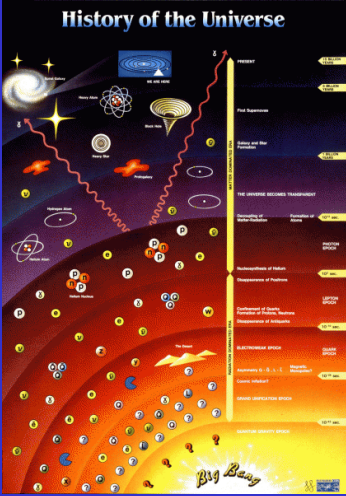


In a diffuse cosmic gas of primordial composition, molecular hydrogen (H_2) forms via a sequence of reactions



H_2 molecules so formed induce the initial cooling and collapse of primordial clouds.

Hydrogen Chemistry



• The formation of H_2^+ and H_2 in the recombination era was first suggested by Saslaw and Zipoy (1967).

MFF UK
exp. theory

Radiative Attachment

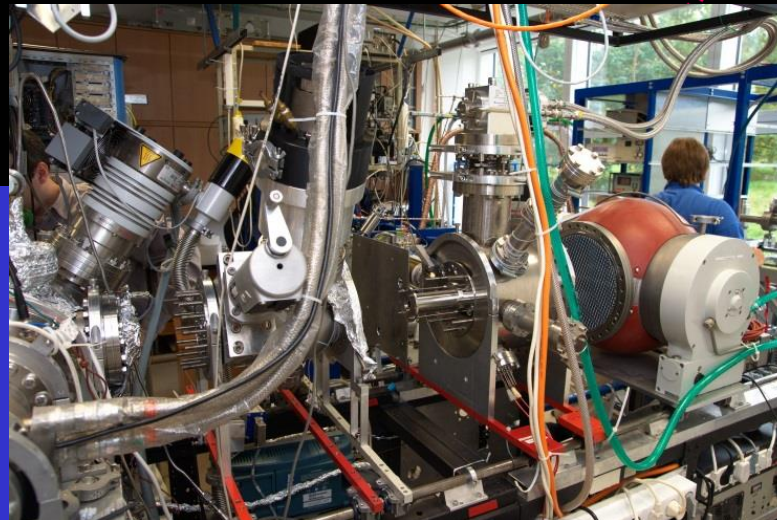
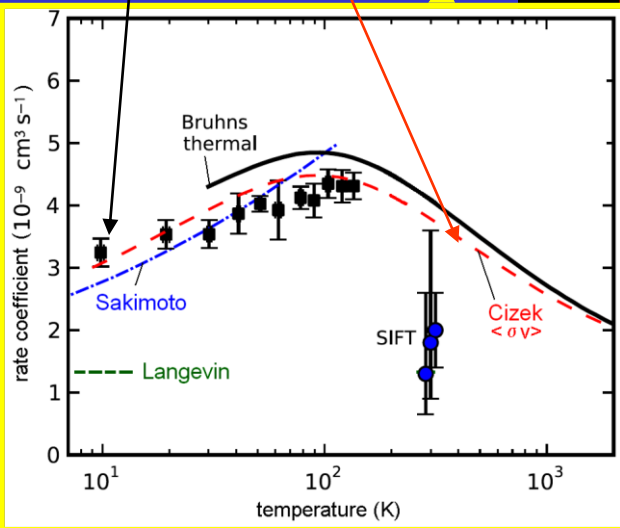


Associative Detachment

Radiative Association



Charge Transfer



He

Chemie des frühen Universums
Prof. Dr. Dieter Gerlich



Doc. M. Čížek

Experimental Results for H₂ Formation from H⁻ and H and Implications for First Star Formation

H. Kreckel,^{1*†} H. Bruhns,^{1‡} M. Čížek,² S. C. O. Glover,³ K. A. Miller,¹ X. Urbain,⁴ D. W. Savin¹

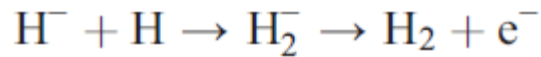
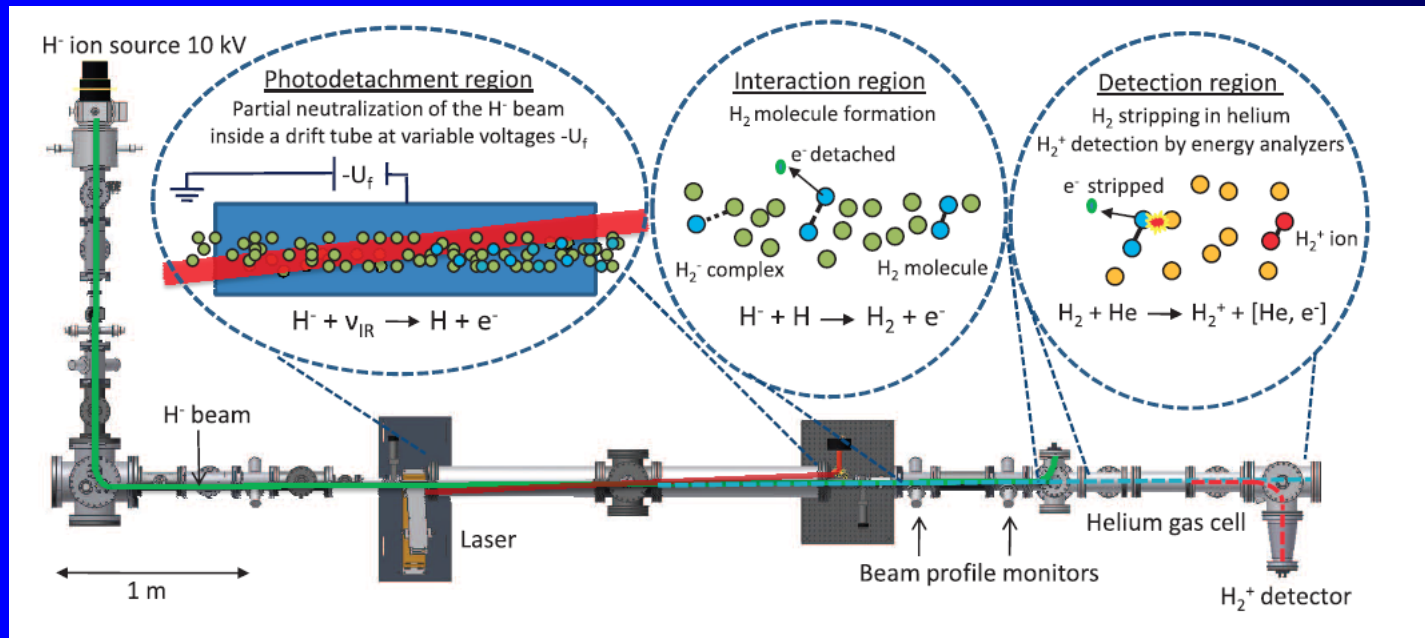
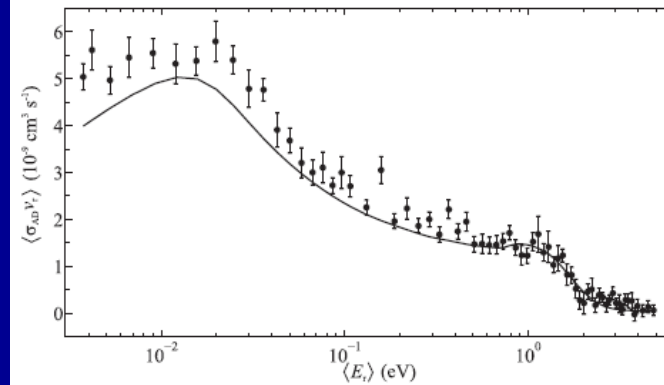


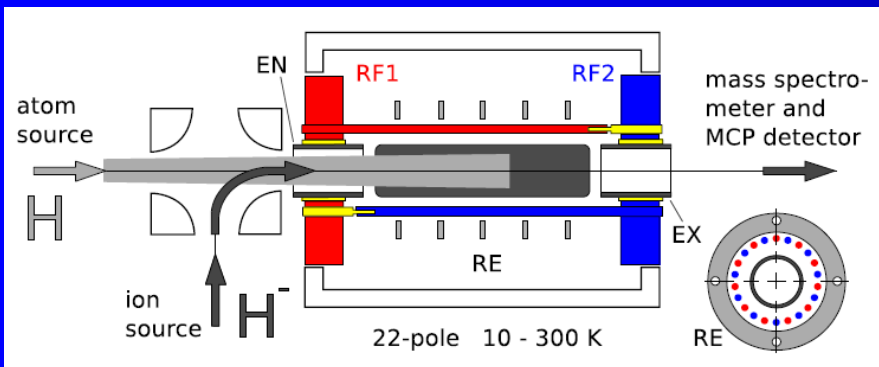
Fig. 1. Schematic of the merged-beams apparatus used to measure the H₂ associative detachment reaction. Infrared laser photons are denoted by ν_{IR} .

During the epoch of first star formation, molecular hydrogen (H₂) generated via associative detachment (AD) of H⁻ and H is believed to have been the main coolant of primordial gas for temperatures below 10⁴ kelvin. The uncertainty in the cross section for this reaction has limited our understanding of protogalaxy formation during this epoch and of the characteristic masses and cooling times for the first stars. We report precise energy-resolved measurements of the AD reaction, made with the use of a specially constructed merged-beams apparatus. Our results agreed well with the most recent theoretically calculated cross section, which we then used in cosmological simulations to demonstrate how the reduced AD uncertainty improves constraints of the predicted masses for Population III stars.



ION TRAP STUDIES OF $H^- + H \rightarrow H_2 + e^-$ BETWEEN 10 AND 135 K

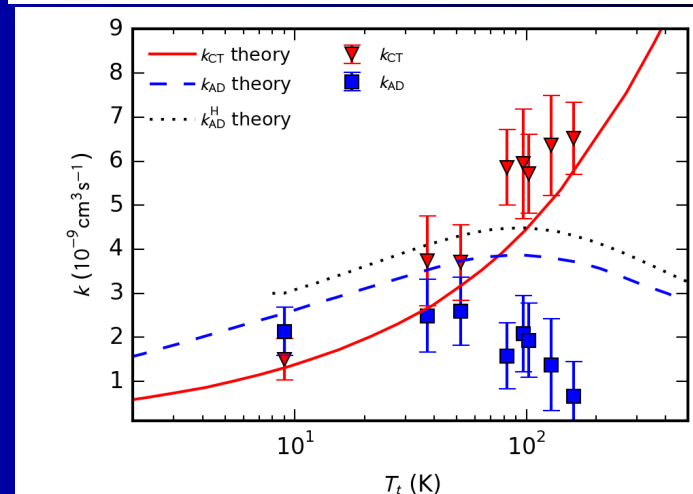
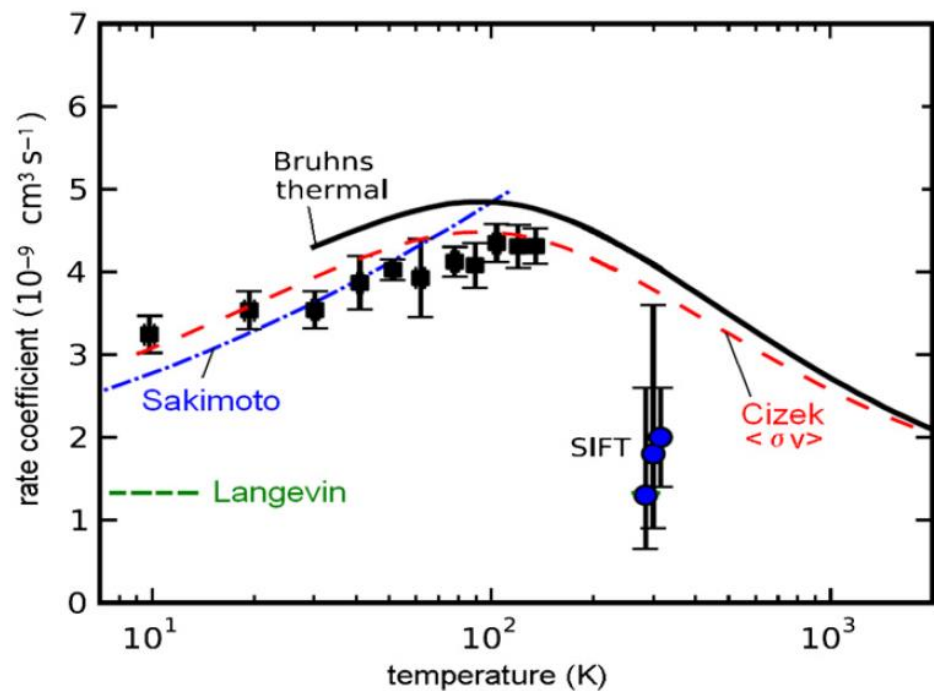
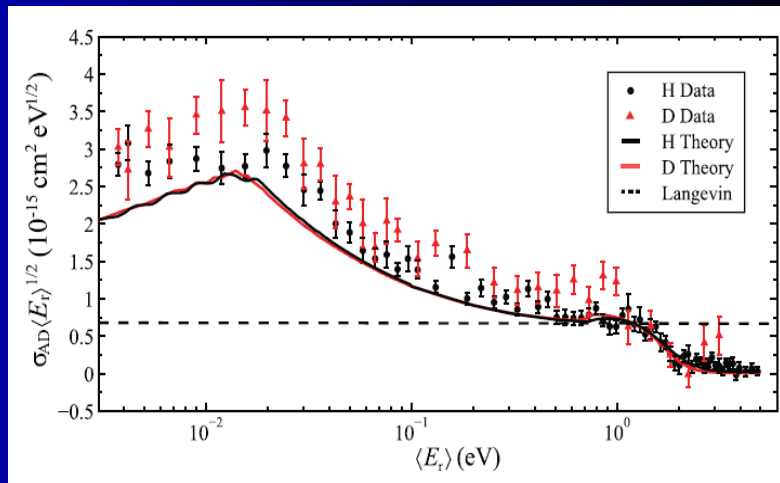
DIETER GERLICH^{1,2}, PAVOL JUSKO¹, ŠTĚPÁN ROUČKA¹, ILLIA ZYMAK¹, RADEK PLAŠIL¹, AND JURAJ GLOŠÍK¹

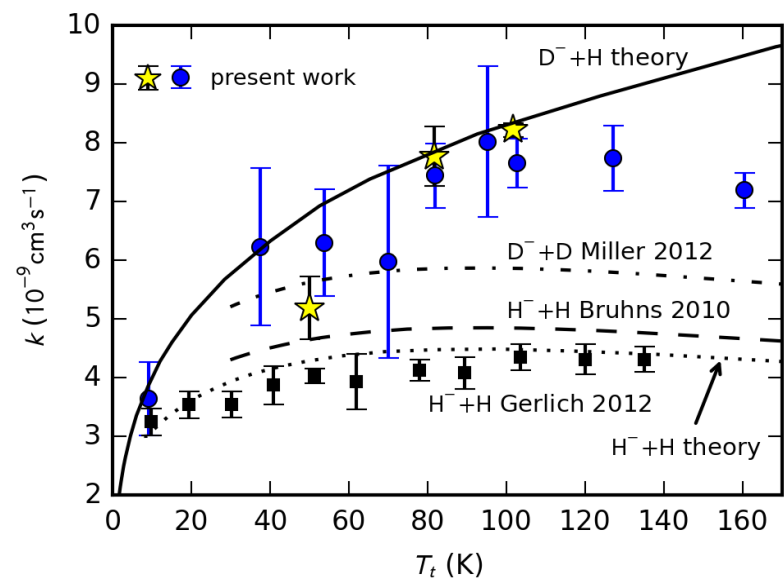
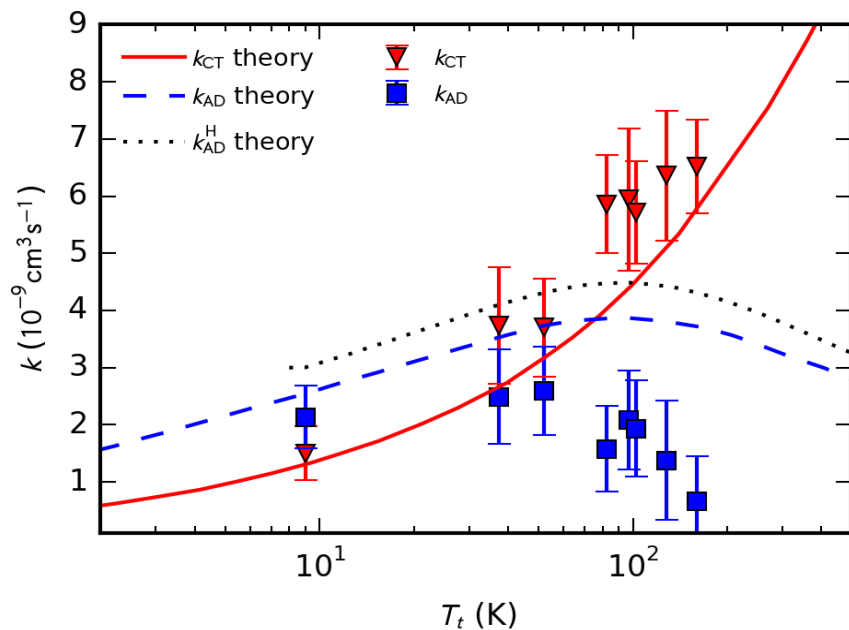
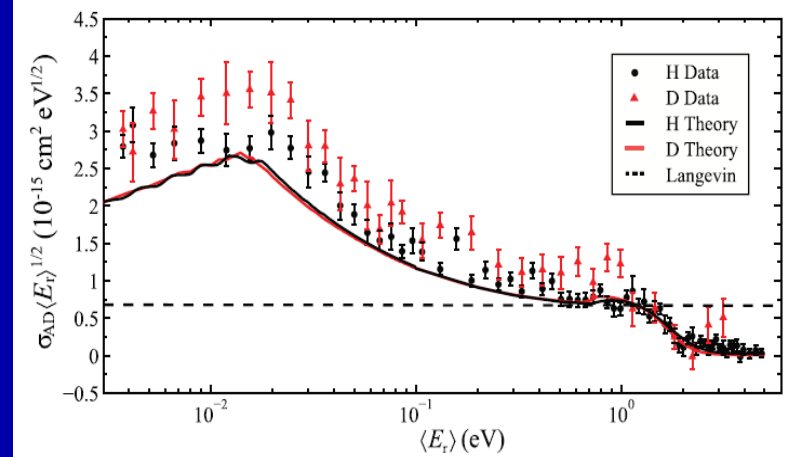
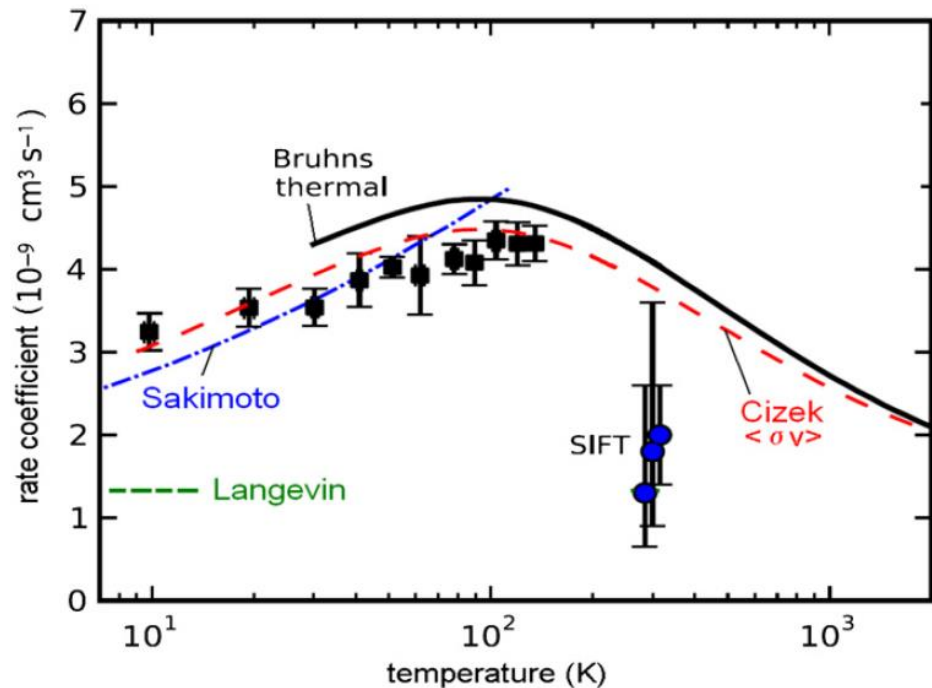


PHYSICAL REVIEW A 86, 032714 (2012)

Isotope effect for associative detachment: $H(D)^- + H(D) \rightarrow H_2(D_2) + e^-$

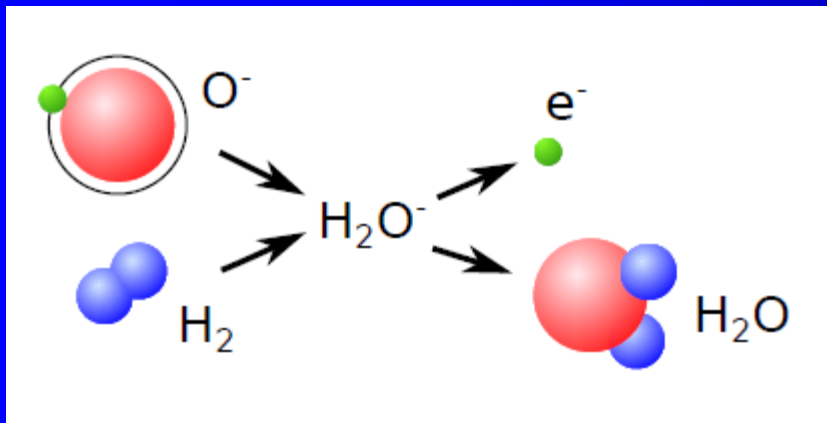
K. A. Miller,¹ H. Bruhns,^{1,*} M. Čížek,² J. Eliášek,² R. Cabrera-Trujillo,³ H. Kreckel,^{1,†}
 A. P. O'Connor,¹ X. Urbain,⁴ and D. W. Savin¹





Ion trap study of $O^- + H_2$ at low temperatures

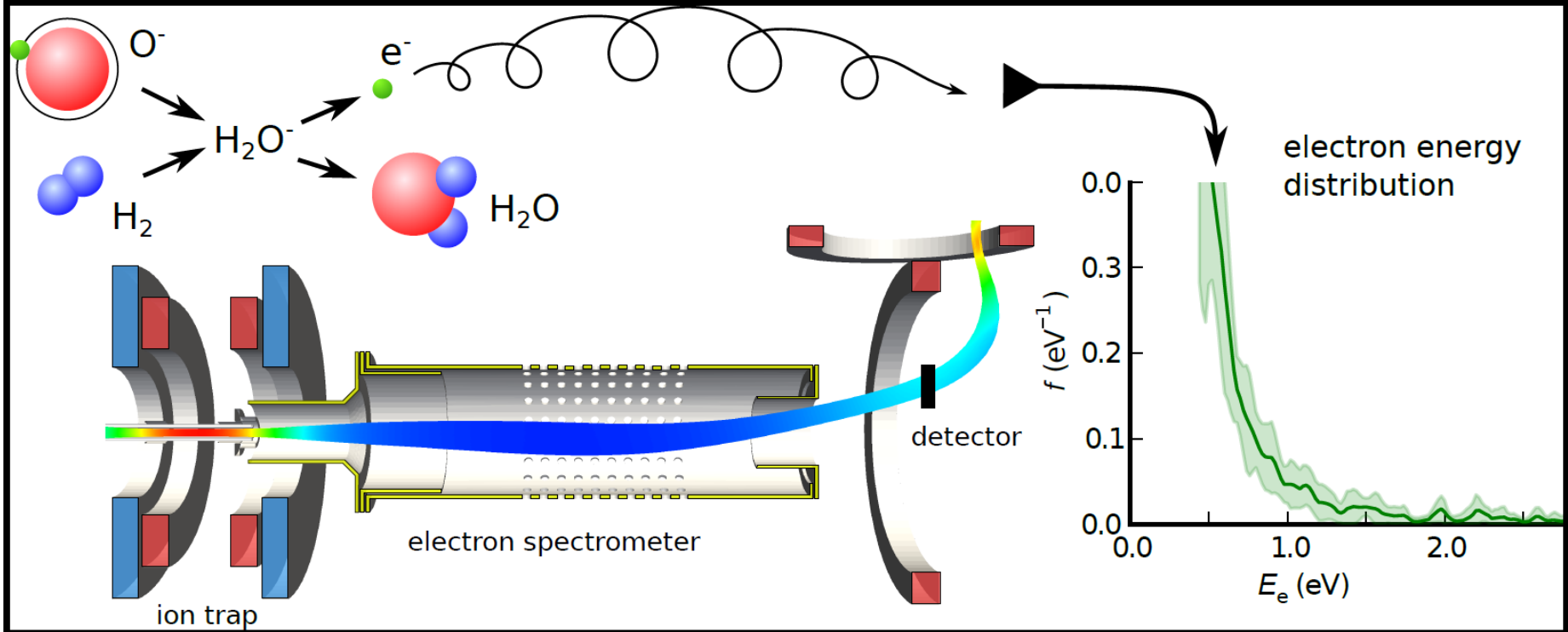
Roučka, Š.¹; Jusko, P.¹; Mulin, D.¹; Zymak, I.¹; Plašil, R.¹;
Gerlich, D.¹; Glosík, J.¹ Čížek, M.²; Houfek, K.²



Determining the energy distribution of electrons produced in associative detachment: The electron spectrometer with multipole trap

P. Jusko, Š. Roučka*, R. Plašil, J. Glosík

International Journal of Mass Spectrometry 352 (2013) 19–28



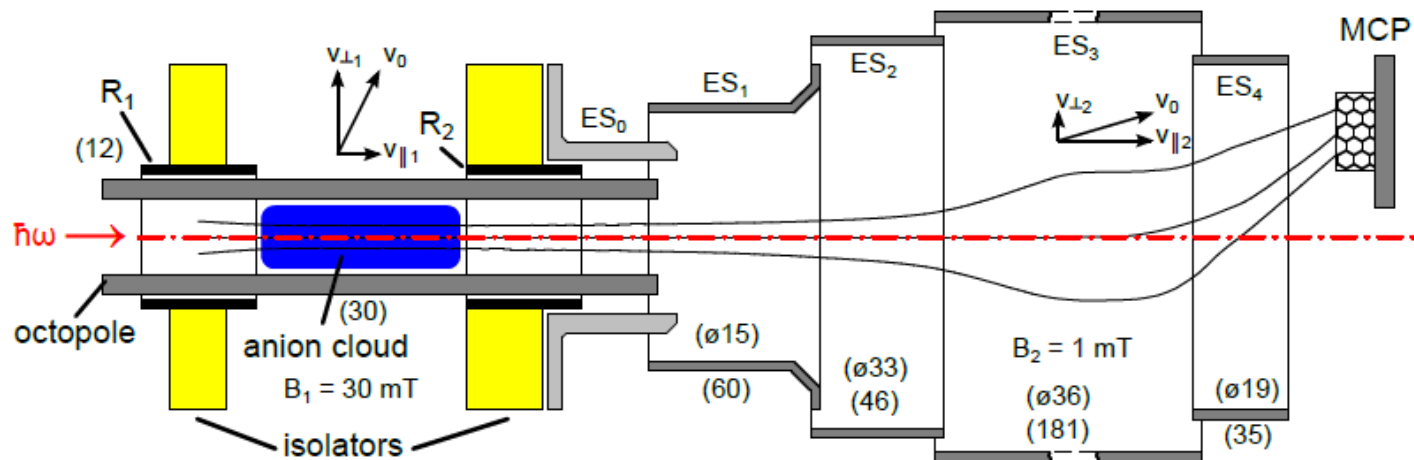


Fig. 1. Schematic diagram of the ES-MPT apparatus (not to scale). The principle of combination of the radiofrequency ion trap (octopole on the left side) and the MAC-E filter (right side). Anions are injected into the octopole trap from the left and confined axially using the electrostatic ring electrodes (R_1 , R_2). Laser radiation can be applied along the axis, reactant gas can be introduced into the trap between R_1 and R_2 . Produced electrons are magnetically guided to the region with lower magnetic field (B_2) and refocused to the MCP detector. Cylindrical electrodes ES0–ES4 create the electrostatic barrier (diameter and length in parentheses are in mm).

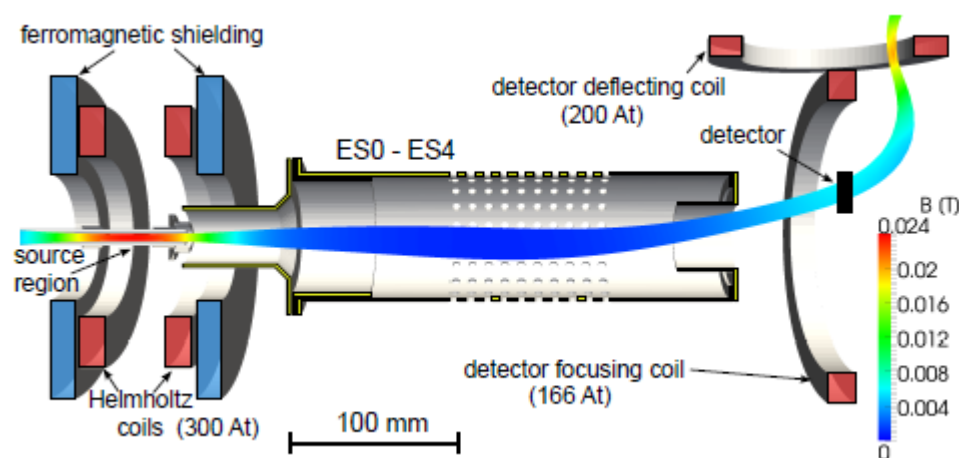
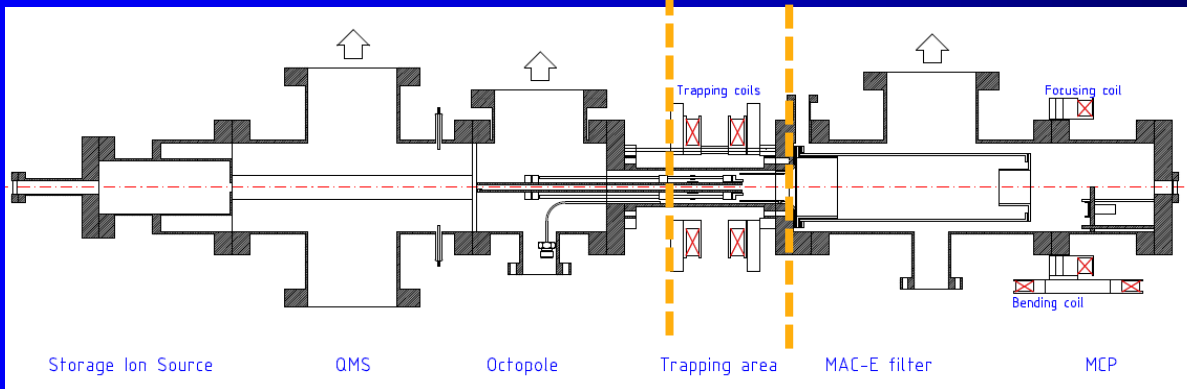
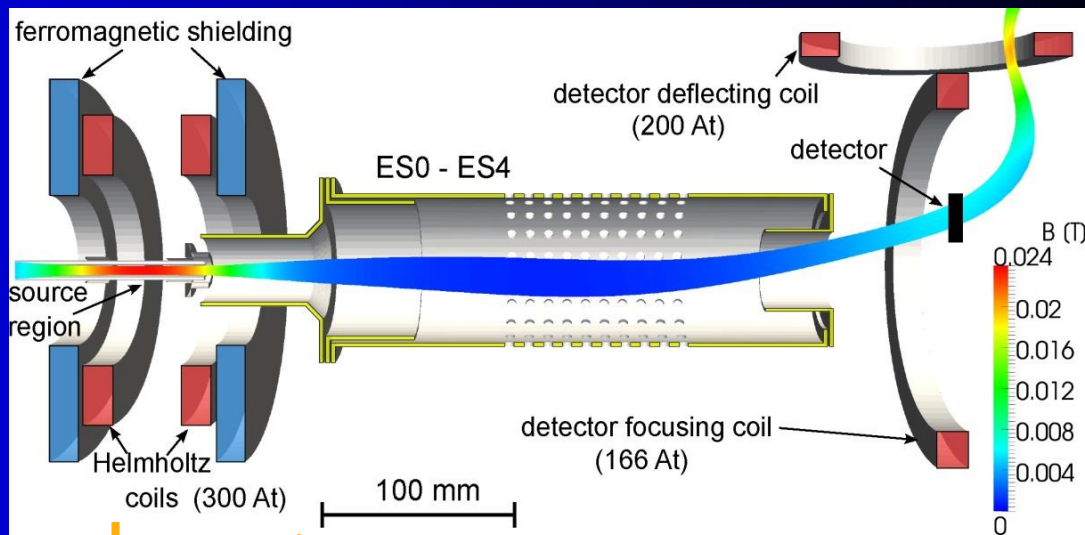
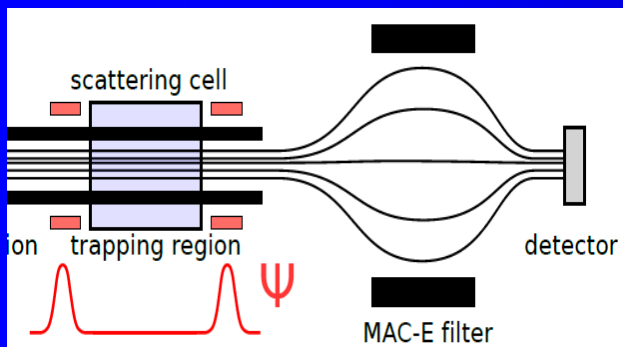
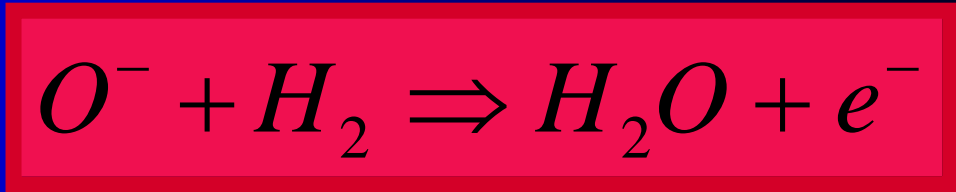


Fig. 2. Configuration of the electrodes, coils, and ferromagnetic elements of the electron spectrometer. The calculated color-coded magnetic field intensity is projected on the calculated magnetic flux tube emanating from the ion trap. The flux tube approximately represents the possible electron trajectories. The number of Ampere-turns (At) used for producing the magnetic field is indicated for each coil. (For interpretation of colour in the artwork, the reader is referred to the web version of the article.)

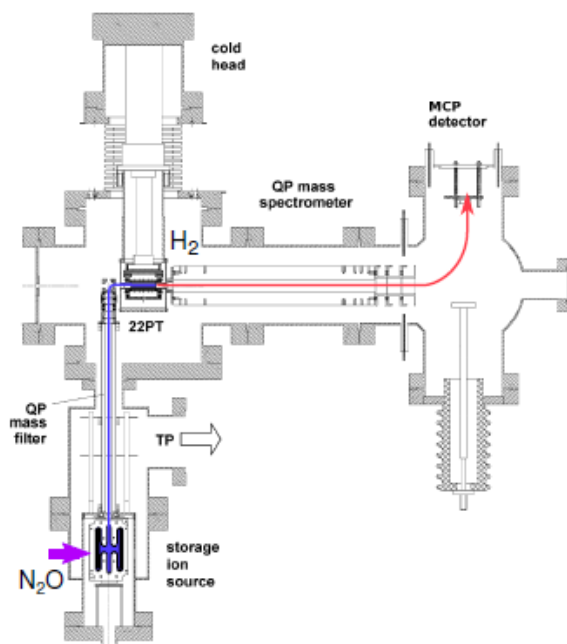
ES-MPT



Experimental techniques – ion traps

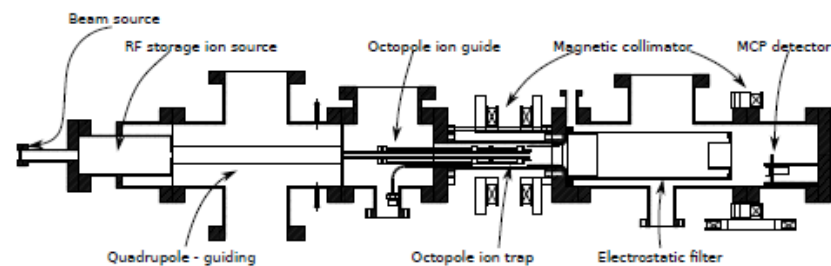
22PT – 22-Pole Trap

- ▶ Measurement of reaction rate coefficients
- ▶ Temperature range 10–300 K

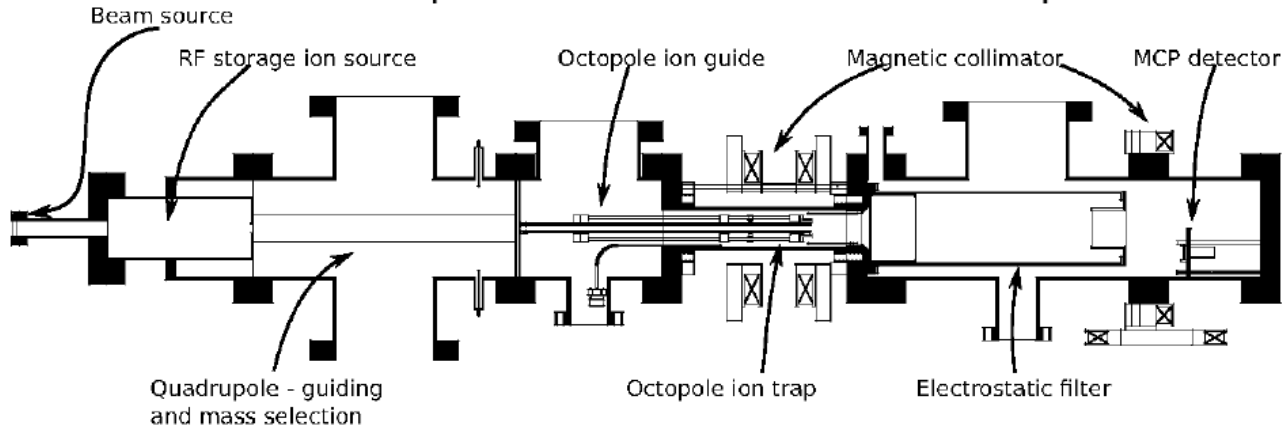


ES-MPT – Electron Spectrometer with MultiPole Trap

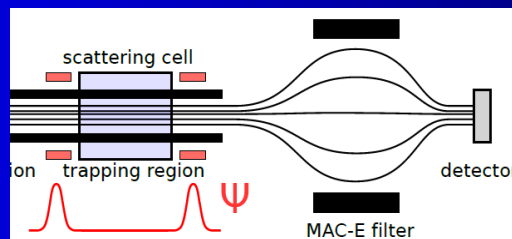
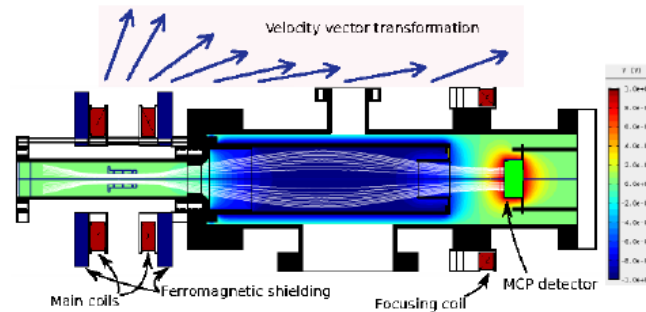
- ▶ Energy distribution of detached electrons
- ▶ Octopole
- ▶ Temperature 300 K



Electron Spectrometer with MultiPole Trap



- ▶ Extraction of electrons produced in the trap
- ▶ Collimation by mag. field and energy analysis by retarding electric field



name

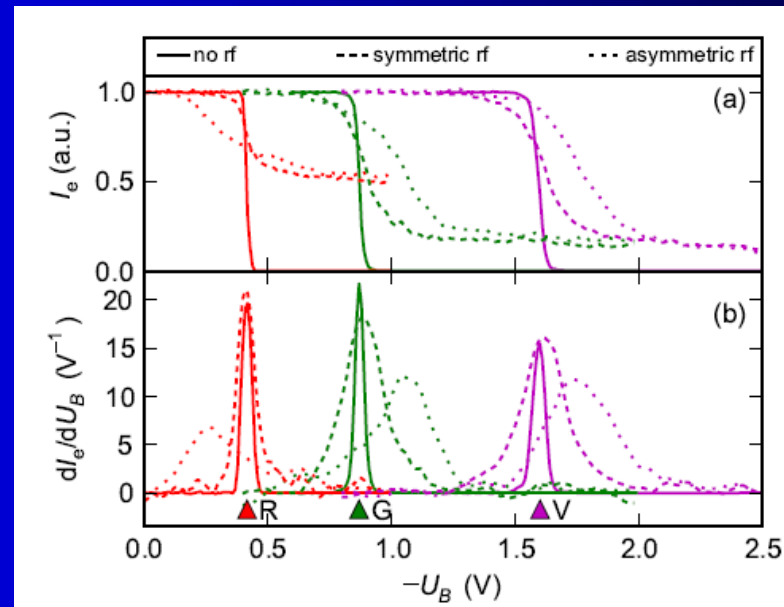
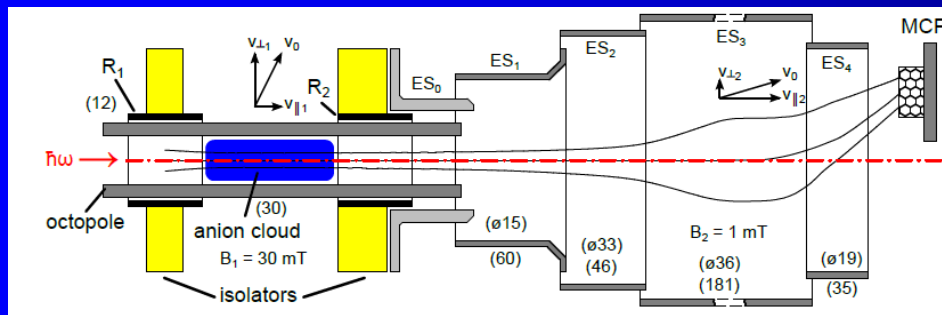


Fig. 3. Simulated spectra of monoenergetic isotropically distributed electrons with energies corresponding to the photodetached electrons from O^- using 660 nm (R), 532 nm (G), and 405 nm (V) lasers (see Table 1). (Panel a) Integral spectra of electrons normalized to unity at zero retarding barrier. (Panel b) Differential spectra obtained by differentiation of the spectra in panel (a). The spectra calculated without rf field (full lines), with ideal symmetric rf field (dashed lines), and with non-ideal asymmetric rf field (dotted lines) are shown.

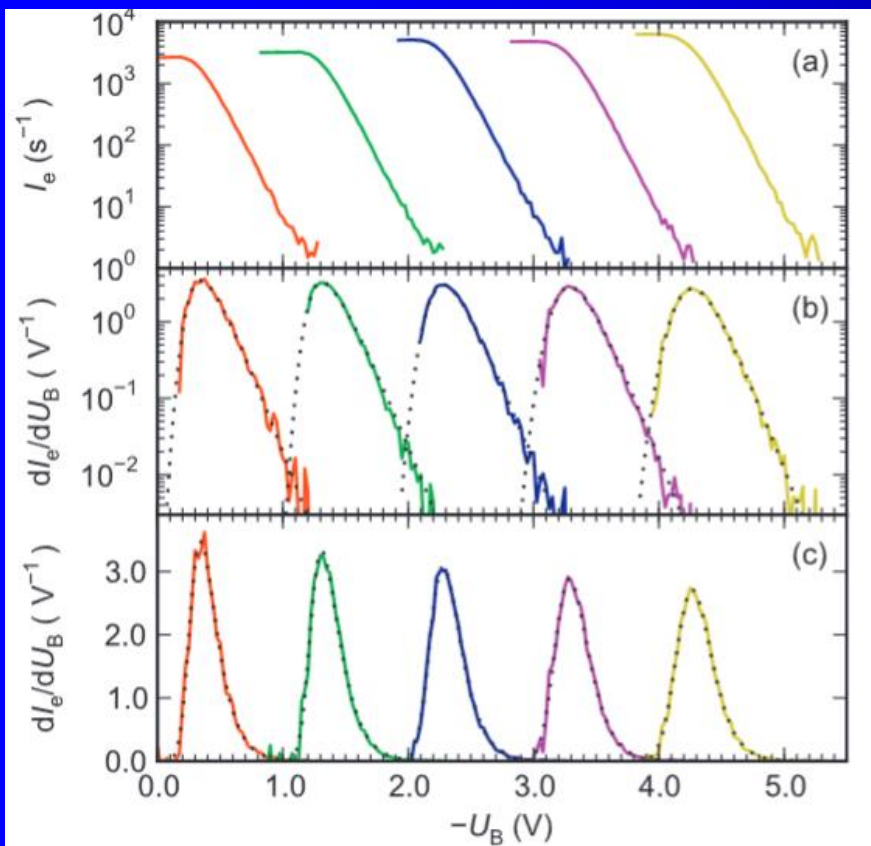


Fig. 4. The measured normalized spectra of electrons produced by thermionic emission from hot filament. (Panel a) Integral recorded spectra. (Panels b and c) Differential spectra (normalized) obtained from the integral spectra in logarithmic and linear scales, respectively. Cathode bias voltages -0.1 , -1.1 , -2.1 , -3.1 and -4.1 V were used to provide electrons of 5 different energy distributions (full lines). Fits of the theoretical spectrum (13) convolved with a Gaussian function and offset by the bias voltage are indicated by the dotted lines.

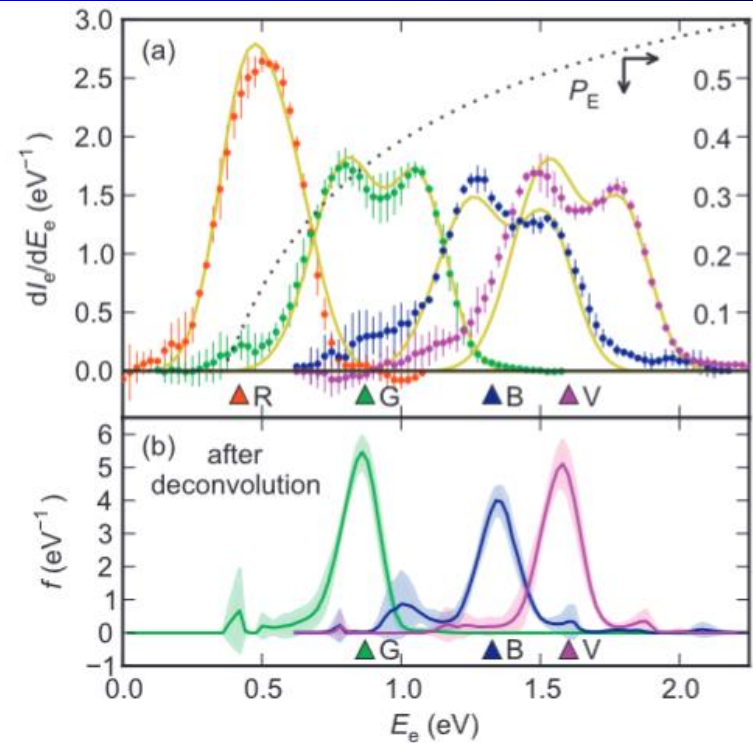
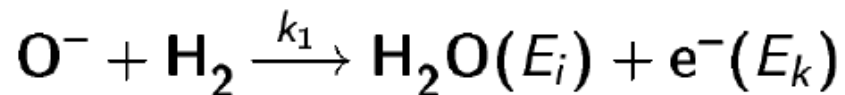
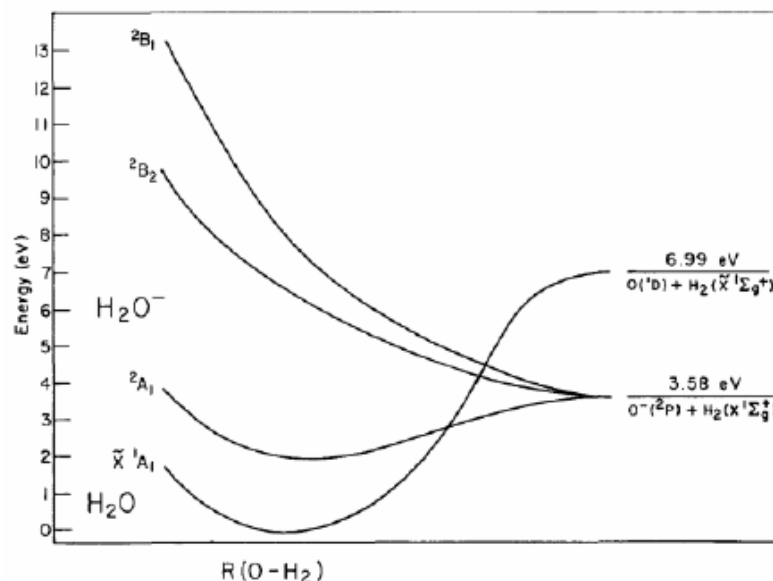


Fig. 8. Measured spectra of electrons photodetached from O^{-} anions. Photon wavelengths used are 660 nm (R), 532 nm (G), 445 nm (B) and 405 nm (V) (see Table 1). (Panel a) Points correspond to data measured with red, green, blue, and violet wavelengths, respectively (from left). Triangles indicate the expected electron energies according to Table 1. The smooth full lines represent the fitted convolution of the theoretical spectrum with the instrument function (Eq. (15)). The extraction probability $P_E(U_T)$ with the trapping potential U_T determined from the fit is indicated by the dotted line and its magnitude is shown on the right axis. (Panel b) The spectra obtained from the measured data after deconvolution with the instrument function. The spectrum of the red laser cannot be deconvolved because the signal is very reduced due to the low extraction probability P_E at electron energies ≈ 0.5 eV. (For interpretation of colour in the artwork, the reader is referred to the web version of the article.)

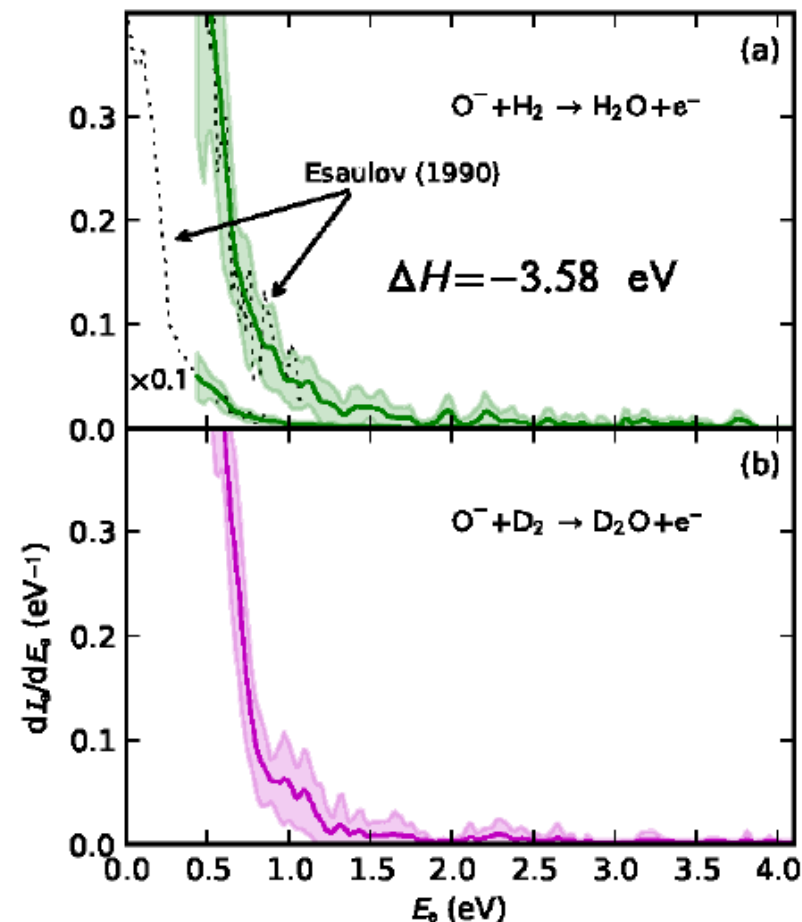
Spectra of detached electrons (ES-MPT instrument)



- ▶ Momentum conservation, Franck-Condon
- ▶ Produced molecule is highly excited

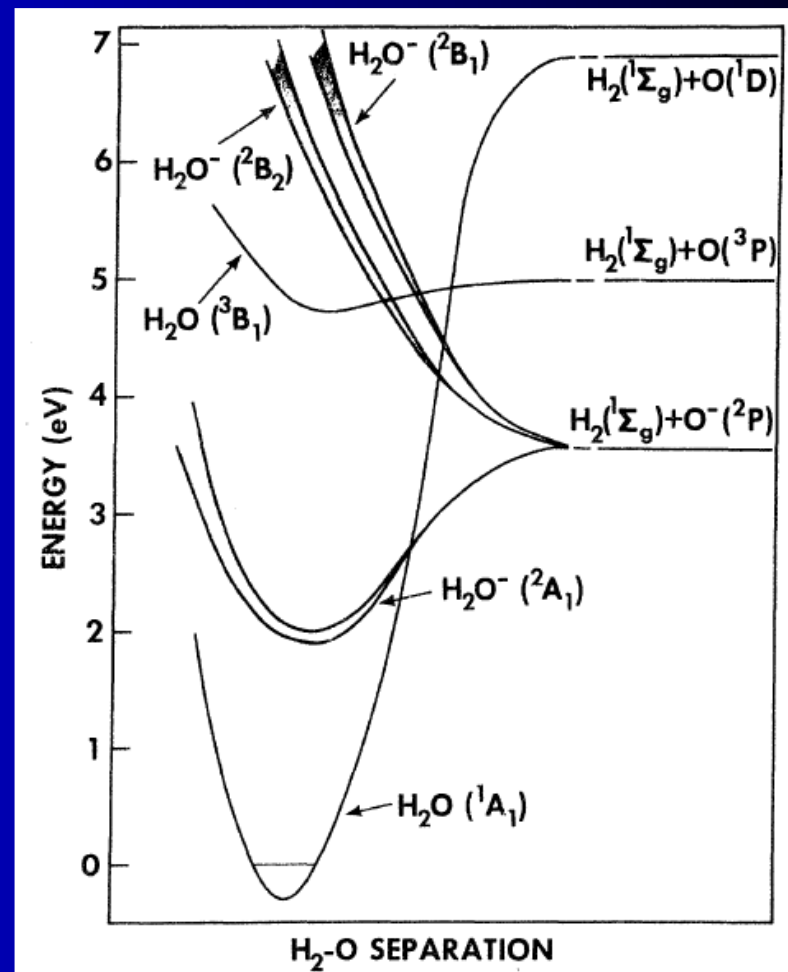
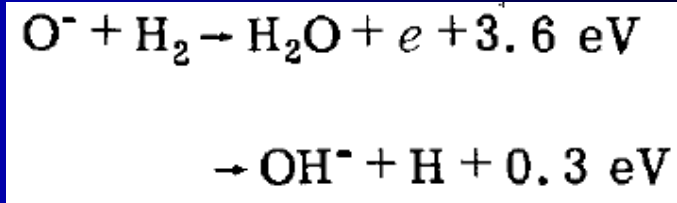
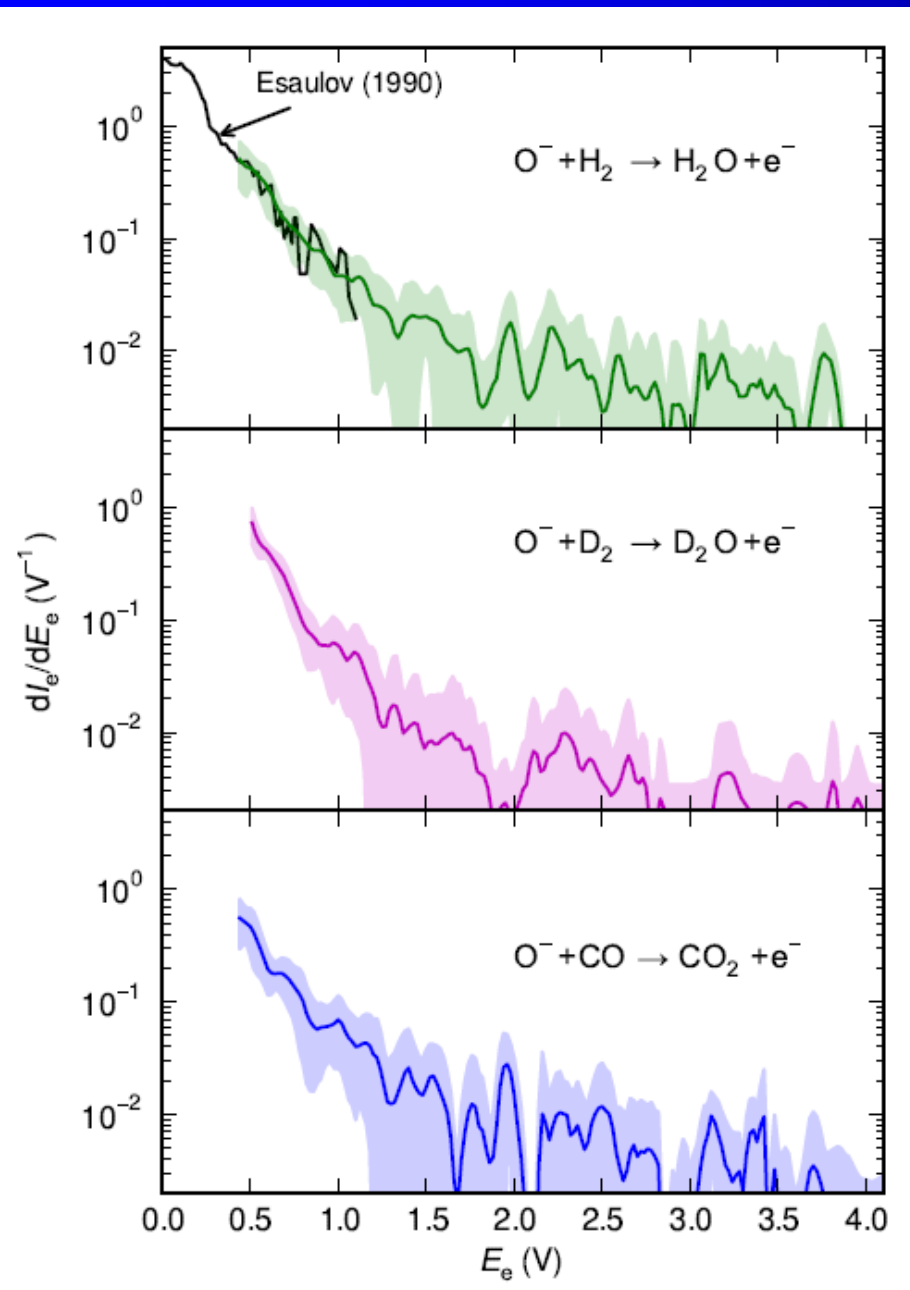


[Claydon et al. JCP 1971]

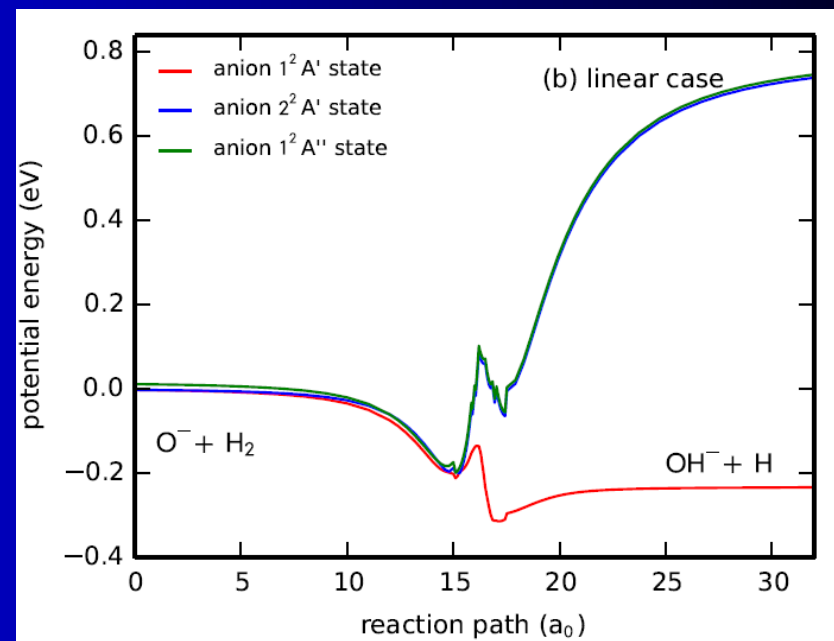
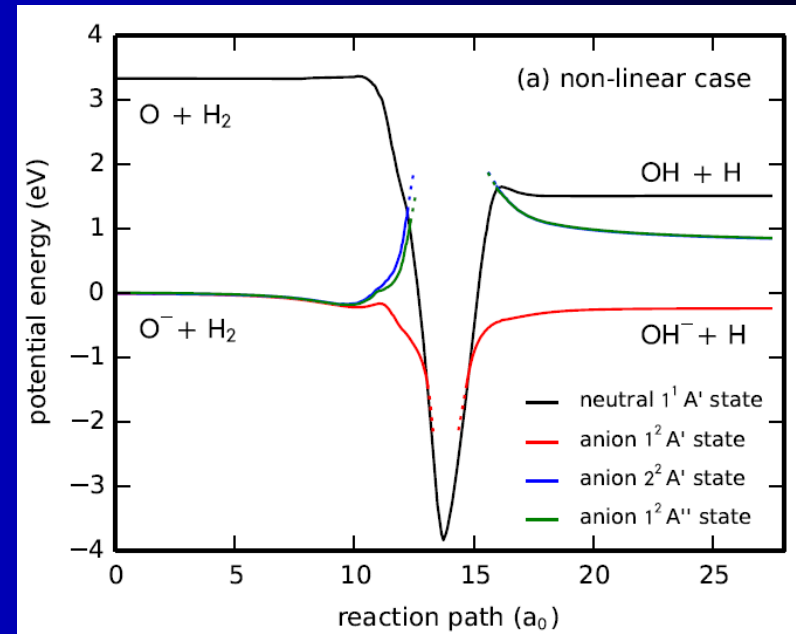
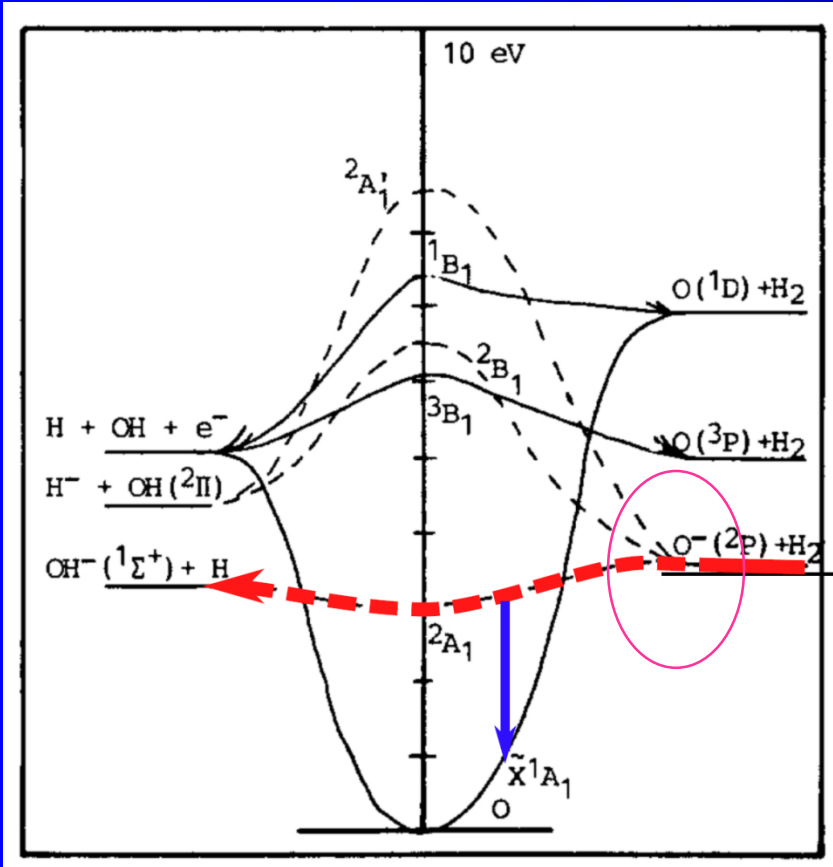


Published in [Jusko, Roučka, Plašil, Glosík; IJMS, 2013]



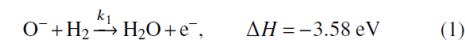


name



Interaction of O^- and H_2 at low temperatures

P. Jusko,¹ Š. Roučka,^{1,a)} D. Mullin,¹ I. Zymak,¹ R. Plašil,¹ D. Gerlich,¹ M. Čížek,² K. Houfek,² and J. Glosík¹



rogen atom transfer

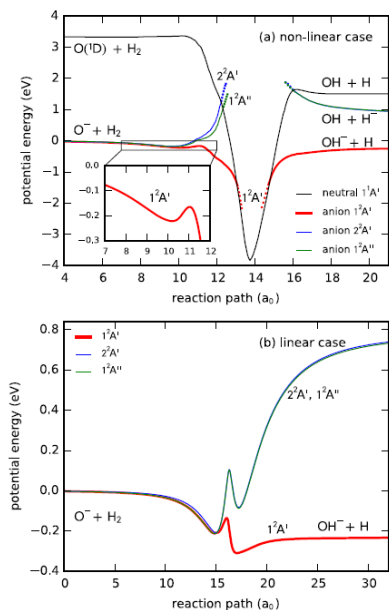
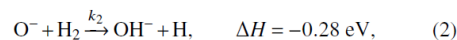


FIG. 3. Panel (a)—PES of H_2O^- and H_2O along the minimum energy path going from $O^- + H_2$ to $OH^- + H$ on the $1^2A'$ PES. The anionic curves in the autodetachment region, where they are above the neutral PES, are indicated by points. The local minimum of the $1^2A'$ PES, where some metastable H_2O^- states may exist, is magnified in the inset. In Panel (b), the path is constrained to the linear geometry, $\theta = 0^\circ$. In this case, the potential energy of the neutral H_2O is too high—outside of the graph.

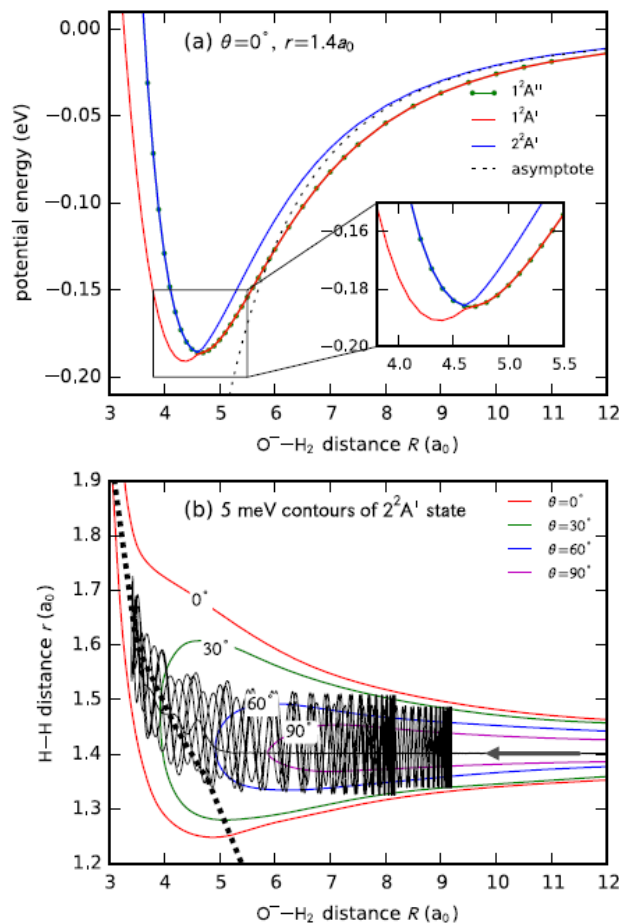


FIG. 4. Panel (a)—Section of the three potential energy surfaces for $\theta = 0^\circ$, $r = 1.4014a_0$, showing the attraction of O^- and H_2 and the conical intersection at $4.6a_0$, coupling them. The sum of quadrupole and polarization potential is marked with a dotted line. Panel (b)—Typical classical trajectory on the $2^2A'$ PES for a collision energy of 5 meV projected on the $\theta = 0^\circ$ plane. The conical intersection at $\theta = 0^\circ$ is marked by the dashed line. The equipotential lines for $V = 5$ meV are also shown for the indicated values of θ . This picture shows a section of a trajectory with a duration of 700 vibrational periods of H_2 . Most trajectories remain trapped for typically 10^4 – 10^5 vibrational periods, passing beyond the conical intersection several hundred times.

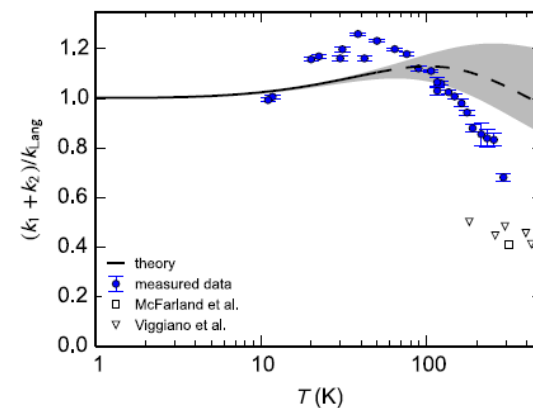
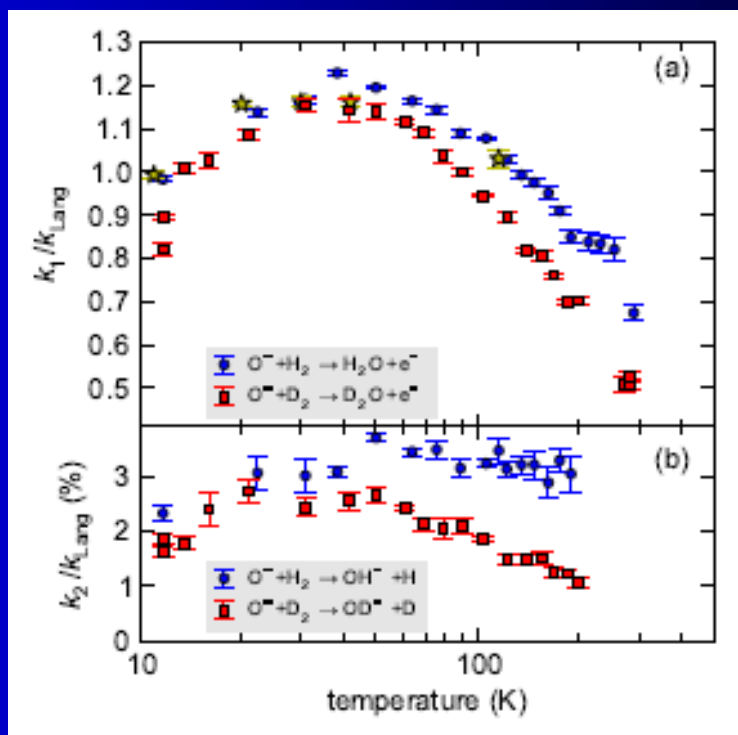
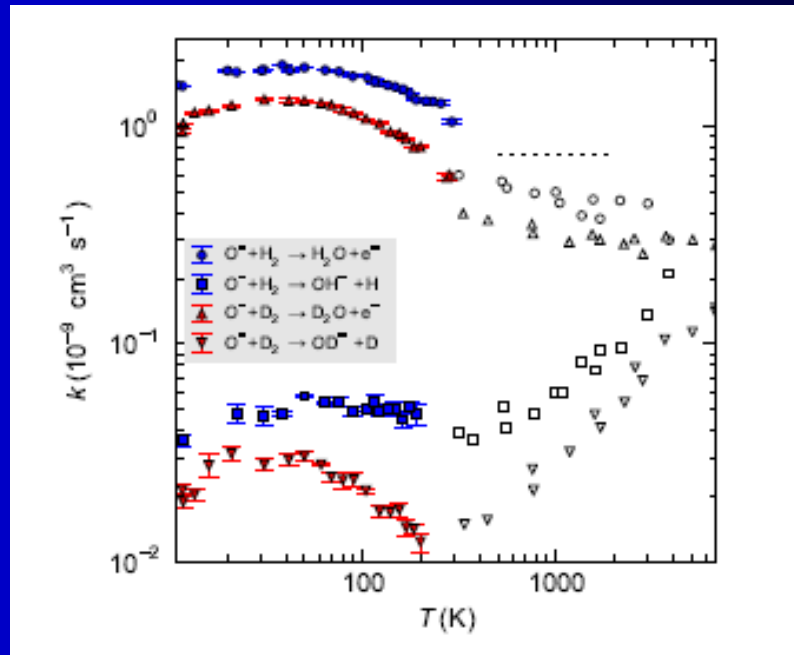
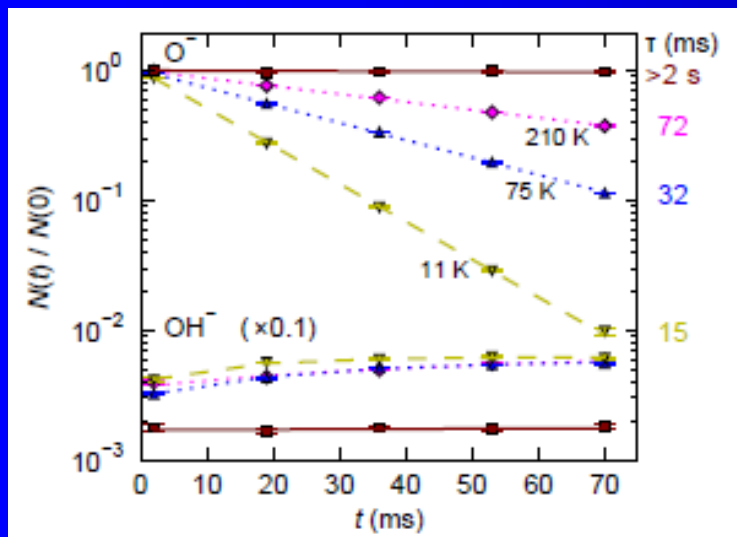


FIG. 5. Comparison of the measured total reaction rate coefficients $k_1 + k_2$ with the values calculated with the 1D capture model described in the text. The data are normalized with the Langevin capture rate coefficient. Sensitivity test of the model is indicated by the gray area. The part of the theoretical curve which is significantly sensitive to the parameters of the absorption potential, is shown as a dashed line. Experimental results of McFarland *et al.*¹⁰ and Viggiano *et al.*¹² are shown for comparison.

Table 2

Total reaction rate coefficient estimated from temporal evolutions of electron production at 300 K (see Fig. 10). Only the statistical error is shown. The results are accurate within a factor of 2 due to systematic errors.

Reaction	k (this work) ($10^{-10} \text{ cm}^3 \text{ s}^{-1}$)	k (McFarland <i>et al.</i> [34]) ($10^{-10} \text{ cm}^3 \text{ s}^{-1}$)
$O^- + H_2$	5.4 ± 0.2	6.4
$O^- + D_2$	3.2 ± 0.1	4.6



Ion trap study of $O^- + H_2$ at low temperatures

Roučka, Š.¹; Jusko, P.¹; Mulin, D.¹; Zymak, I.¹; Plašil, R.¹;
Gerlich, D.¹; Glosík, J.¹ Čížek, M.²; Houfek, K.²

